

DISSERTATION
SUBMITTED TO THE
COMBINED FACULTIES FOR THE NATURAL SCIENCES AND FOR MATHEMATICS OF THE
RUPERTO-CAROLA UNIVERSITY OF HEIDELBERG, GERMANY
FOR THE DEGREE OF
DOCTOR OF NATURAL SCIENCES

Put forward by
Torben Karl Schell, M.Sc.
Born in Heidelberg, Germany
Oral examination: February 1, 2017

New Directions in Top Physics

Referees: Prof. Dr. Tilman Plehn
Prof. Dr. Jan Martin Pawłowski

Abstract

The top quark plays an important role for many aspects of particle physics. The coupling of the Higgs boson to top quarks is a key parameter to probe electroweak symmetry breaking and is important for the evolution of the Higgs potential to high energies. In addition, many models of physics beyond the Standard Model predict heavy particles that decay to top-quark pairs. Furthermore, the unexplained hierarchy of fermion masses culminates in the large top-quark mass. In this thesis, we consider resonance searches based on top quarks in the fully hadronic final state. We employ multivariate techniques in form of boosted decision trees and add several improvements to the original HEPTOPTAGGER algorithm. These modifications and extensions result in the new HEPTOPTAGGER2. The achieved improvements are used to estimate the precision to which the top Yukawa coupling can be measured at a future 100 TeV proton-proton collider in the fully hadronic final state of $t\bar{t}H$ production. We find that at such a collider a precision measurement of the top Yukawa coupling to 1% should be possible. The statistical precision is backed up by demonstrating that in the ratio $\sigma(t\bar{t}H)/\sigma(t\bar{t}Z)$ theoretical uncertainties cancel to below-percent level. Finally, we propose a Froggatt-Nielsen-type model to address the hierarchy of fermion masses in the Standard Model and determine current and projected bounds on the available parameter space.

Zusammenfassung

Das Top-Quark spielt eine wichtige Rolle in vielen Bereichen der Teilchenphysik. Die Kopplung des Higgs-Bosons an Top-Quarks ist ein entscheidender Parameter für die Untersuchung der elektroschwachen Symmetriebrechung und für die Entwicklung des Higgs-Potentials zu hohen Energien. Des Weiteren sagen viele Modelle für Physik jenseits des Standard Modells neue schwere Teilchen voraus, die in Top-Quark-Paare zerfallen. Ferner findet die im Standard Modell nicht erklärte Hierarchie der Quark-Massen ihren Höhepunkt in der Top-Masse. In dieser Arbeit werden Resonanzsuchen betrachtet, die auf hadronisch zerfallenden Top-Quarks basieren. Hierzu werden multivariate Analysen in Form von Boosted Decision Trees verwendet und der ursprüngliche HEPTOPTAGGER wird in mehreren Aspekten verbessert. Diese Veränderungen und Erweiterungen ergeben den neuen HEPTOPTAGGER2. Die erreichten Verbesserungen werden benutzt, um abzuschätzen, wie präzise die Top-Yukawa-Kopplung an einem zukünftigen 100 TeV Proton-Proton-Beschleuniger gemessen werden kann. Es stellt sich heraus, dass an einem solchen Beschleuniger eine Präzisionsmessung im Prozentbereich möglich sein sollte. Die statistische Genauigkeit wird durch die Beobachtung gestützt, dass sich im Verhältnis $\sigma(t\bar{t}H)/\sigma(t\bar{t}Z)$ Theorieunsicherheiten größtenteils aufheben. Schließlich schlagen wir ein Modell à la Froggatt-Nielsen vor, das auf eine Erklärung der Hierarchie der Fermion-Massen im Standard Modell abzielt. Für dieses Modell werden die gegenwärtigen und in naher Zukunft zu erwartenden Grenzen für den möglichen Parameterraum untersucht.

Contents

Preface	1
I. Introduction	3
II. Basic concepts	6
A. Fermion masses in the Standard Model	6
B. The top quark	7
C. Event generation	9
D. Some basic concepts of collider physics	15
E. HEPTopTagging	18
F. Boosted decision trees	23
III. Resonance searches with boosted top quarks	26
A. Resonance reconstruction	27
B. Updated tagger	35
C. Full event information	41
D. Conclusions	45
IV. Measuring the top Yukawa coupling at a future hadron collider	46
A. Theoretical systematics for the $t\bar{t}H/t\bar{t}Z$ production rate	49
B. Boosted $t\bar{t}H$ at 100 TeV	56
C. Updated BDRS tagger	60
D. Conclusions	64
V. A possible explanation for the hierarchy of Yukawa couplings	66
A. Flavon model	68
B. Quark flavor constraints	74
C. Future lepton flavor measurements	80
D. Future hadron collider measurements	86
E. Conclusions	93
VI. Summary	96

Acknowledgments	98
A. HEPTopTagger2 performance	99
B. More details on the flavon model	104
Masses and couplings	104
Benchmark point for the flavon model	107
References	110

Preface

Like many other fields of research, particle phenomenology lives from the active collaboration of scientists. A typical form of research are small projects benefiting from common effort and the expertise of involved people. This thesis combines some of the projects the author has been part of. The presented results were achieved in close collaboration with other researchers and have been published as

- [1] M. Bauer, T. Schell and T. Plehn, “Hunting the Flavon,” *Phys. Rev. D* 94, no. 5, 056003 (2016),
- [2] M. L. Mangano, T. Plehn, P. Reimitz, T. Schell and H. S. Shao, “Measuring the Top Yukawa Coupling at 100 TeV,” *J. Phys. G* 43, no. 3, 035001 (2016),
- [3] G. Kasieczka, T. Plehn, T. Schell, T. Strebler and G. P. Salam, “Resonance Searches with an Updated Top Tagger,” *JHEP* 1506, 203 (2015).

They led to contributions to

- [5] R. Contino et al., “Physics at a 100 TeV pp collider: Higgs and EW symmetry breaking studies,” arXiv:1606.09408 [hep-ph],
- [6] T. Golling et al., “Physics at a 100 TeV pp collider: beyond the Standard Model phenomena,” arXiv:1606.00947 [hep-ph].

During his PhD studies the author contributed also to the following publication that is not incorporated in this thesis

- [7] J. Bramante, P. J. Fox, A. Martin, B. Ostdiek, T. Plehn, T. Schell and M. Takeuchi, “Relic neutralino surface at a 100 TeV collider,” *Phys. Rev. D* 91, no. 5, 054015 (2015).

Finally, the author is involved in ongoing projects that have not been ready for publication at the time of writing this thesis.

I. INTRODUCTION

One of the best-tested theories in modern physics is the Standard Model of particle physics [1–6]. Its success culminated in the discovery of the Higgs boson in July 2012 at the Large Hadron Collider (LHC) [7, 8] which has been made possible by amazing experimental efforts. Since then, we have entered the era of precision studies of the new particles' couplings. On the other hand, there are still open questions that are not explained within the Standard Model, like dark matter [9], the electroweak hierarchy problem [10], or neutrino masses [11].

In both cases, top quarks play an important role. In the Standard Model the coupling of the Higgs boson to top quarks is predicted to be of order unity and thus is an important probe for the mechanism of electroweak symmetry breaking. In the context of physics beyond the Standard Model (BSM) many models predict new heavy particles that decay to top quarks, yielding signatures that can be studied at the LHC.

In the past years, incredible progress has been made in the field of boosted analysis strategies and jet substructures. These techniques allow for example to reconstruct boosted top quarks like they typically occur in decays of heavy BSM resonances but also enable analyses of Standard Model processes like the production of a Higgs boson associated with a pair of top quarks ($t\bar{t}H$).

After reviewing some basic concepts, we introduce the original HEPTOPTAGGER in chapter II E. This algorithm aims for the reconstruction of hadronically decayed top quarks in a moderately boosted phase-space regime. In chapter III, we extend and improve the algorithm focusing on the reconstruction of a heavy resonance.

Top tagging can also be used to test the top Yukawa coupling y_t . The precision with which this coupling can be determined at the LHC is limited to $\sim 10\%$ [12, 13]. Employing the ratio $\sigma(t\bar{t}H)/\sigma(t\bar{t}Z)$ and the new version of the HEPTOPTAGGER, we illustrate in Sec. IV that a future 100 TeV collider can improve the precision to which y_t can be extracted to one percent.

While such a measurement will provide a crucial test of our understanding of electroweak symmetry breaking, it does not explain the large range of fermion masses. A model that generates such hierarchies is introduced and investigated in Sec. V. There, we estimate

effects on common flavor observables in terms of an effective field theory and confront the available parameter space with recent and projected limits of indirect searches. Additionally, we investigate to which extent the parameter space can be probed in direct searches at a future 100 TeV proton-proton collider.

II. BASIC CONCEPTS

Since there are plenty of introductions to the Standard Model [14–16], collider physics [17, 18] or Monte Carlo simulations [19, 20], this chapter only reviews some of the essential ingredients that are relevant for the following chapters. For more information on individual aspects, we refer the reader to the provided references which we partially follow here.

A. Fermion masses in the Standard Model

Despite solving the issue of heavy gauge bosons, the Higgs field gives mass to the Standard Model fermions, except the neutrinos. The naive mass term for a fermion Ψ

$$\mathcal{L}_{SM} \supset -m\bar{\Psi}\Psi = -m(\bar{\Psi}_L\Psi_R + \bar{\Psi}_R\Psi_L) \quad \Psi_{L,R} = P_{L,R}\Psi = \left(\frac{1 \pm \gamma_5}{2}\right)\Psi \quad (\text{II.1})$$

is forbidden by $SU(2)_L$ gauge transformations. Instead, the Higgs doublet Φ and its charge conjugate $\tilde{\Phi} = i\sigma_2\Phi^*$ generate the fermion mass terms by spontaneous breaking of the electroweak symmetry

$$\begin{aligned} \mathcal{L}_{SM} &\supset -y_{d_{ij}}\bar{Q}_i\Phi d_{R_j} - y_{u_{ij}}\bar{Q}_i\tilde{\Phi}u_{R_j} - y_{\ell_{ij}}\bar{L}_i\Phi\ell_{R_j} + \text{h.c.} \\ &\rightarrow -y_{d_{ij}}\frac{v+h}{\sqrt{2}}\bar{d}_{L_i}d_{R_j} - y_{u_{ij}}\frac{v+h}{\sqrt{2}}\bar{u}_{L_i}u_{R_j} - y_{\ell_{ij}}\frac{v+h}{\sqrt{2}}\bar{\ell}_{L_i}\ell_{R_j} + \text{h.c.} \\ &= -m_{d_i}\left[1 + \frac{h}{v}\right]\bar{d}_{L_i}^M d_{R_i}^M - m_{u_i}\left[1 + \frac{h}{v}\right]\bar{u}_{L_i}^M u_{R_i}^M - m_{\ell_i}\left[1 + \frac{h}{v}\right]\bar{\ell}_{L_i}^M \ell_{R_i}^M + \text{h.c.}, \end{aligned} \quad (\text{II.2})$$

where we diagonalized the coupling matrix in the last step by changing from flavor to mass eigenstates. As usual, $Q_i = (u_{L_i}, d_{L_i})^T$ and $L_i = (\nu_{L_i}, \ell_{L_i})^T$ denote the left-handed electroweak quark and lepton doublet respectively. In the Standard Model, the couplings between the Higgs boson and the fermions in the mass basis are set by the Yukawa couplings $y_i = \frac{\sqrt{2}m_i}{v}$ and the vacuum expectation value (VEV) of the Higgs field v .

B. The top quark

Already its mass distinguishes the top quark from all other quarks. With a mass of $m_t = 173.2$ GeV [19] it is the heaviest particle in the Standard Model and thus the top Yukawa coupling $y_t \sim 1$ is a key parameter to test our understanding of electroweak symmetry breaking. In addition, y_t is a crucial parameter for the evolution of the Higgs potential to higher, more fundamental energy scales and thus for the stability of the electroweak vacuum [21]. Very closely connected to the large mass is its short life time $\tau = \mathcal{O}(10^{-25}$ s). Since this is smaller than the typical time scale of hadronization, there are no hadrons containing top quarks.

Figure II.1 illustrates a tree-level Feynman graph for top decays and the leading-order branching ratios. Throughout this thesis, we refer to decays $t \rightarrow bq\bar{q}'$ as hadronic and $t \rightarrow b\ell^+\nu_\ell$ with $\ell = e, \mu$ as leptonic top decays. The decay to τ -leptons comes with additional challenges due to the second neutrino from the τ -decay and hadronic τ -decay modes.

Top quarks also occur in signatures of many extension of the Standard Model. For example, in supersymmetric models, the scalar partner of the top, the stop, can decay to a top quark and the lightest supersymmetric particle. Models with extended gauge groups can give rise to additional $U(1)$ gauge groups. If the corresponding new gauge boson, the Z' boson, is heavy and couples to quarks it can decay to $t\bar{t}$ pairs. In some of these models the Z' boson does not couple to leptons and has an enhanced coupling to up-type quarks like the top or couples only to the third generation. Especially in such cases, the new

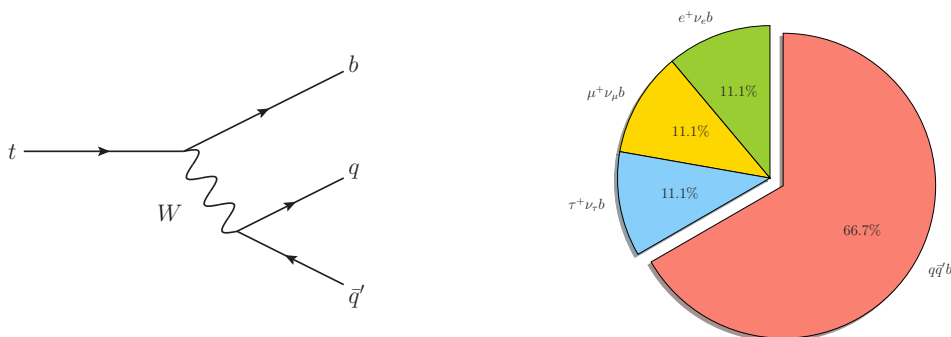


Figure II.1: Feynman graph for the hadronic decay of a top quark (left) and branching ratios assuming massless decay products (right).

particle should manifest itself as a peak in the m_{tt} distribution of top-pair production. For an exhaustive review of Z' models see *e.g.* Ref [22].

C. Event generation

The calculation of cross sections for processes at the LHC is slightly more involved than calculating the parton-level cross section $\hat{\sigma}$ from the hard matrix element. Parton-level results have to be folded with the parton density functions $f_i(x)$ which describe the probability to find a parton i with momentum fraction x inside the proton. The factorization theorem allows us to split the hard process from the description of the partons inside the proton, such that [17]

$$\sigma_{PP}(s, \mu_F, \mu_R) = \int_0^1 dx_1 \int_0^1 dx_2 \sum_{a,b} f_a(x_1, \mu_F) f_b(x_2, \mu_F) \hat{\sigma}_{ab}(x_1 x_2 s, \mu_R), \quad (\text{II.3})$$

where μ_F and μ_R denote the factorization and renormalization scale respectively and s denotes the squared center-of-mass energy of the proton-proton collision. Multiplied with the momentum fractions of the incoming partons x_1 and x_2 it yields the squared center-of-mass energy $\hat{s} = x_1 x_2 s$ on parton level.

While in many cases the total partonic cross section can be calculated analytically, one often relies on numerical integration which directly allows for the generation of actual events, *i.e.* specific phase-space configurations. However, the simulation of an entire event is more complicated as illustrated in the right panel of Fig. II.2.

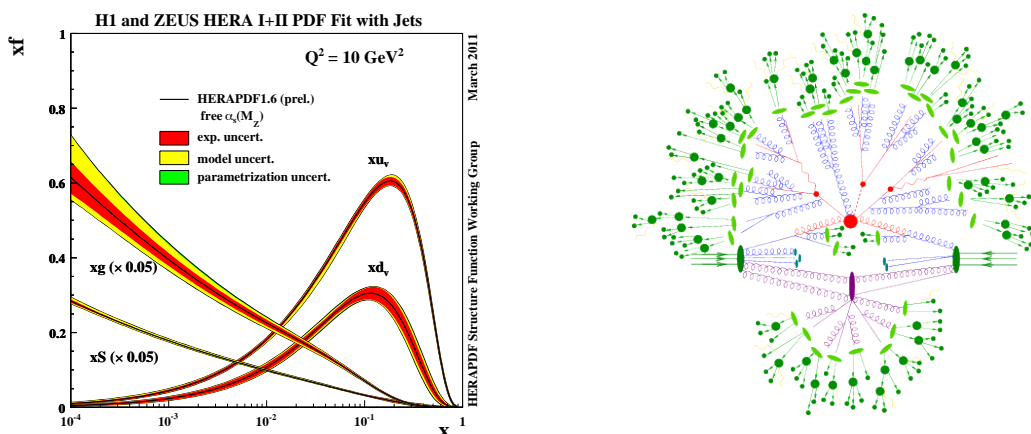


Figure II.2: Left: parton distribution functions inside the proton. Taken from [23]. Right: schematic illustration of various parts of event generation: the hard process (red), parton shower (blue), underlying event (pink) and hadronic physics (green). Taken from [24].

First, the parton-level matrix element \mathcal{M} can be evaluated at a given phase-space point, resulting in a weight for this phase-space point. Since the hard process happens typically at high energy scales ($Q \gg \Lambda_{QCD}$), we can rely on perturbative QCD and quarks and gluon as dynamical degrees of freedom.

A general $2 \rightarrow n$ process can be described by

$$d\sigma_{2 \rightarrow n} = \frac{1}{2\hat{s}} |\mathcal{M}|^2 d\Phi_n, \quad (\text{II.4})$$

where $2\hat{s}$ corresponds to the flux factor. To obtain the cross section one has to integrate over the n -particle Lorentz-invariant phase space Φ_n . Including the momentum fractions of the initial partons and taking into account energy-momentum conservation as well as on-shellness of the partons this yields a ($d = 3n + 2 - 4$)-dimensional integration space. Today, the only efficient way to integrate over such a high-dimensional space is Monte Carlo integration, *i.e.* replacing the integration by a sequence of N random points $\{y\}$. After reparametrizing the integration volume to the unit cube

$$\int_{[0,1]^d} d^d y f(y) = \langle f \rangle \approx \frac{1}{N} \sum_i^N f(y_i), \quad (\text{II.5})$$

where we assumed $f(y) \geq 0$. The integration error and thus the convergence of integration can be improved by importance sampling. Approximating $f(y)$ by a function $p(y) \geq 0$, we can write

$$\int_{[0,1]^d} d^d y f(y) = \int_{[0,1]^d} d^d y \frac{f(y)}{p(y)} p(y) = \left\langle \frac{f(y)}{p(y)} \right\rangle, \quad (\text{II.6})$$

if we can interpret $p(y)$ as probability distribution function. Since $f(y)/p(y)$ should be flatter than $f(y)$, the needed number of random points to achieve a certain precision is reduced, provided we can generate them according to $p(y)$.

In our situation, each point y corresponds to a certain phase-space point. The transition is provided by a mapping X which leads to a phase-space weight $g(y)$ for each point y

$$\frac{1}{g(y)} = \frac{d\Phi_n(X(y))}{dy}. \quad (\text{II.7})$$

A single mapping is often referred to as channel. In principle, it can be useful to employ

multiple channels X_i since they might cover different phase-space regimes more efficiently. For example, if several amplitudes contribute to the matrix element

$$|\mathcal{M}|^2 = \left| \sum_i \mathcal{A}_i \right|^2 = \frac{\left| \sum_i \mathcal{A}_i \right|^2}{\sum_i |\mathcal{A}_i|^2} \sum_i |\mathcal{A}_i|^2, \quad (\text{II.8})$$

one can use a different channel for each $|\mathcal{A}_i|^2$ with a relative weight $|\sum_i \mathcal{A}_i|^2 / \sum_i |\mathcal{A}_i|^2$. This multichannel phase-space generation proceeds by introducing a priori selection probabilities α_i for each channel which can be adjusted at runtime. Based on an additional flat random number $\tilde{\alpha}$ for each y a single channel $X(y, \tilde{\alpha}) = X_k(y)$ is selected. The phase-space weight is then given by $g(y) = \sum_k \alpha_k g_k(y)$. For each random point y , we thus receive a phase-space configuration, the initial momentum fractions and $d\sigma = g(y) f_1(x_1) f_2(x_2) \mathcal{M}(X(y))$, *i.e.* an event with corresponding weight.

In addition to the hard process, we have to account for the soft and collinear behavior of QCD. For example, collinear splittings of an outgoing quark or gluon scale like $\alpha_S(Q^2) \log(Q^2/\Lambda_{QCD})$. In combination with the scaling logarithms from the running of the strong coupling $\alpha_S = g_S^2/4\pi$, this leads to order-one corrections at all orders in perturbation theory. However, large logarithmically divergent corrections from soft and collinear splittings in the final state are canceled by virtual corrections in the total cross section order by order in perturbation theory (KLN theorem [25]). On the other hand, the factorization theorem allows us to absorb collinear initial-state singularities into the parton distribution functions. Thus the parton-level cross section can be used at fixed order in perturbation theory as long as it is interpreted as an inclusive result.

It can be shown [18] that the phase space for an additional collinear parton factorizes

$$d\Phi_{n+1} = d\Phi_n \frac{dp_a^2 dz d\phi}{4(2\pi)^3} (1 + \mathcal{O}(\theta)) = d\Phi_n \frac{dp_a^2 dz}{4(2\pi)^2} (1 + \mathcal{O}(\theta)), \quad (\text{II.9})$$

where θ stands for the splitting angle, p_a denotes the four-momentum before the splitting, and $0 < z < 1$ corresponds to the energy ratio of one parton after the splitting and the original one. Further, one can argue that the squared matrix element factorizes as well giving rise to universal splitting kernels $\frac{2g_s}{p_a} P(z)$ [18]. Finally, this leads for collinear

splittings to

$$d\sigma_{n+1} = \sigma_n \sum_{i,j} \frac{\alpha_S}{2\pi} \frac{d\theta^2}{\theta^2} dz P_{j \leftarrow i}(z, \phi) d\phi, \quad (\text{II.10})$$

where $j \leftarrow i$ is a shorthand for an additional parton of kind j from a splitting of the parton i . The splitting kernels for massless partons can be deduced to be [18]

$$\begin{aligned} P(z)_{g \leftarrow q} &= C_F \frac{1 + (1-z)^2}{z} & P(z)_{q \leftarrow g} &= T_R (z^2 + (1-z)^2) \\ P(z)_{q \leftarrow q} &= C_F \frac{1 + z^2}{1-z} & P(z)_{g \leftarrow g} &= C_A \left(\frac{z}{1-z} + \frac{1-z}{z} + z(1-z) \right), \end{aligned} \quad (\text{II.11})$$

where for $SU(3)$ $C_A = 3$, $C_F = 4/3$, and $T_R = 1/2$. To account for the leading logarithms changing the initial and final state, we can thus start from an event at the hard-matrix-element level and apply a series of splittings to the partons, where each splitting is associated with a certain probability. This is the basic idea behind initial and final-state parton showers.

An important object in parton showers are Sudakov factors which are for final-state showers defined as

$$\Delta_i^{\text{FSR}}(t, t') = \exp \left[- \sum_j \int_{t'}^t \frac{dt''}{t''} \int_0^1 dy \frac{\alpha_s(t'')}{2\pi} P_{j \leftarrow i}(y) \right], \quad (\text{II.12})$$

where t denotes the virtuality. To interpret this quantity, consider the Poisson distribution describing the probability to find n events if all events are independent and occur with probability p

$$\mathcal{P}(n; p) = \frac{p^n e^{-p}}{n!}. \quad (\text{II.13})$$

The probability to find no event is $\mathcal{P}(0; p) = \exp(-p)$ identifying the Sudakov factors with non-splitting probabilities.

By generating a flat random number $r \in [0, 1]$, we can solve $\Delta(t, t') = r$ for t' . If t' is between t and t_{end} , we generate a splitting at t' according to $P_{j \leftarrow i}(z)$. Otherwise, the parton is left unchanged. This algorithm can be applied iteratively to all partons until they reach a termination scale $t_{\text{end}} \sim 1$ GeV. A possible choice for the initial scale of the shower

is the factorization scale μ_F .

For initial-state radiation, we can use the parton shower as backward evolution. However, this time the Sudakov factors have to account for the fact that there are several initial configurations that can give rise to the current state and the changed initial-state configuration

$$\Delta_i^{\text{ISR}}(t, t') = \exp \left[- \sum_j \int_{t'}^t \frac{dt''}{t''} \int_x^1 \frac{dy}{y} \frac{\alpha_s(t'')}{2\pi} P_{j \leftarrow i}(y) \frac{f_j(t'', x/y)}{f_i(t'', x)} \right]. \quad (\text{II.14})$$

In addition, initial-state splittings introduce transverse momentum to the partons of the hard process and the corresponding recoils have to be distributed over all particles.

A second kind of divergences emerges from the fact that the gluon is massless. In consequence, soft gluons can be emitted at arbitrary angle. It has been shown, that using the angle instead of virtuality as ordering parameter in the shower correctly describes the double-logarithmic regime of soft and collinear splittings. Physically, this can be justified by the constructive interference of large-angle soft emissions from collinear particles. When using the radiation angle as scale, α_S at the splitting vertices should be evaluated at the relative parton transverse momentum after the splitting.

Once all strongly interacting final-state particles are evolved to scales $\sim \Lambda_{QCD}$, they have to be combined into colorless hadrons. At this stage also the remnants of the colliding partons have to be taken into account. Usually, the shower algorithm takes care of the color flow during the evolution and thus it is known which particles are color-connected. The transition from the colored final state after parton showers to colorless primary hadrons is called hadronization. There are different models that try to perform this transition like the Lund string model [26] or the cluster model [27]. Once primary hadrons are formed, their decays can be simulated using the known branching ratios.

Similar logarithmic divergences like for the colored partons are connected to the emission of photons and can be treated *e.g.* with shower algorithms as well.

While the parton-shower algorithms describe soft and collinear radiations well, they are not reliable for hard large-angle radiations. One method to achieve good results in both phase-space regimes is to match or merge matrix elements with parton showers. The idea is to cut the phase space into different regimes at a scale Q_{cut} . Radiations above this scale

are simulated as additional partons in the hard process. The rest should be covered by the parton showers. For each final-state multiplicity of hard partons one generates a separate sample which then is showered. Vetoing parton-shower radiations above the scale Q_{cut} ensures that there is no double counting. For the highest multiplicity sample there is no such cut applied. Therefore, all samples except the one with highest considered multiplicity are exclusive. This allows for a simple combination of the obtained samples.

Until now each event has a weight $d\sigma$. However, for a sample of events measured in an experiment this is a strange concept. To bridge the conceptual difference, we can pick events with a probability according to their weights and receive an unweighted sample.

All activity in an event that is not covered by the hard process and the corresponding initial and final-state showers is summarized as underlying event (UE). Most of this activity is expected to originate from additional color exchanges between the beam particles which can be simulated as multi-parton-parton interactions (MPI). There are two effects: First, there might occur additional hard parton-parton interactions resulting in additional jets (see below). Secondly, soft interactions between the partons influence the color flow and the totally exchanged momentum and hence lead to a higher hadronic activity in the detector.

Finally, the colliding objects are often not single protons, but proton bunches. Therefore, there is a fair chance of several proton-proton collisions in a single bunch crossing being detected at the same time. From this pile-up of interactions one has to extract the single interaction of interest. While this is a relevant source of contamination, the available amazing experimental techniques of pile-up subtraction allow us to neglect this effect for all our studies.

There are cases, in which one wants to take into account the effects of a detector. While simple acceptance cuts, preclustering of hadronic activity and global tagging efficiencies can be used as simple approximations, effects like the propagation in the magnetic field of the detector, more elaborate tagging efficiencies and geometrical constraints can be applied performing fast detector simulations e.g. with DELPHES3 [28]. However, to account for example for dead material and the interaction of the particles with different parts of the detector, full detector simulations are performed by the experimental collaborations.

D. Some basic concepts of collider physics

To describe the kinematics of an event, we need to define appropriate quantities. The common choice is to use a coordinate system in which the beam line is identified with the z -axis. The x -axis is chosen to point to the center of the collider and y -axis points upwards. A complication at hadron colliders is that the center of mass of the parton-level process is not known. We assume that it lies on the beam axis and thus the usual azimuthal angle ϕ and the scalar transverse momentum $p_T = \sqrt{p_x^2 + p_y^2}$ can be used to describe the kinematics in the plane transverse to the beam axis. The rapidity

$$y = \frac{1}{2} \log \frac{E + p_z}{E - p_z} \quad (\text{II.15})$$

is well suited to describe the remaining direction, since it is additive under longitudinal Lorentz boosts. In the limit of massless particles it is identical to the pseudorapidity η

$$y \approx \frac{1}{2} \log \frac{1 + \cos \theta}{1 - \cos \theta} =: \eta, \quad (\text{II.16})$$

which can be translated to the polar angle $\theta = 2 \arctan(e^{-\eta})$. Angular separations of two objects can be described by

$$\Delta R = \sqrt{(\Delta\phi)^2 + (\Delta y)^2}. \quad (\text{II.17})$$

As explained in the previous section, final-state quarks and gluons will split several times before they reach the hadronization scale and form color-neutral hadrons. Thus final-state quarks and gluons do result in a spray of hadrons that can be measured as energy deposits in the calorimeters of a detector. To reconstruct an object close the parton-level quark or gluon, sequential recombination algorithms have been established. The resulting objects of these algorithms are called jets. A generic clustering algorithm is based on the following steps:

1. Find the minimal distance between all prejets including the distances to the beam axis $d_{\min} = \min(d_{ij}, d_{iB})$.

2. If $d_{\min} < d_{\text{cut}}$, join the two prejets. For the case that the minimal distance is of the kind d_{iB} remove prejet i (beam radiation).
3. Iterate until there is only one object left or $d_{\min} > d_{\text{cut}}$.

The remaining objects are returned as jets. Since we are interested in the jet mass as physical observable, we join the subjects following the E -scheme, *i.e.* we add their four-vectors. The outlined exclusive procedure has a stop criterion d_{cut} . Usually one is interested in all jets in the event and will decide which ones are interesting at a later stage. By identifying d_{cut} with d_{iB} , one obtains the inclusive jet clustering algorithms which we will use in all analyses. The distinctive part of the various jet algorithms is their distance measure. For the three standard algorithms, it can be written as

$$d_{ij} = \min(p_{T,i}^a, p_{T,j}^a) \left(\frac{\Delta R_{ij}}{R} \right) \quad d_{iB} = p_{t,i}^a. \quad (\text{II.18})$$

For $a = 1$ the measure yields the k_T algorithm [29], $a = 0$ defines the measure of the Cambridge-Aachen (C/A) algorithm [30], and jet clustering with $a = -1$ is referred to as anti- k_T [29]. The parameter R trades off the beam and the subject distances. In C/A clustering it has a geometrical meaning as the size of the jet and thus is generally referred to as jet size. While the k_T algorithm combines soft structures first, the C/A measure quantifies collinearity. Both approaches are well-motivated by QCD. The anti- k_T algorithm starts by clustering hard structures and leads to well-defined jet areas. Figure II.3 illustrates the different results of these algorithms on the same event.

An important complication arises in QCD-busy environments like at hadron colliders. In such cases, there is additional hadronic activity that has to be removed in order to extract

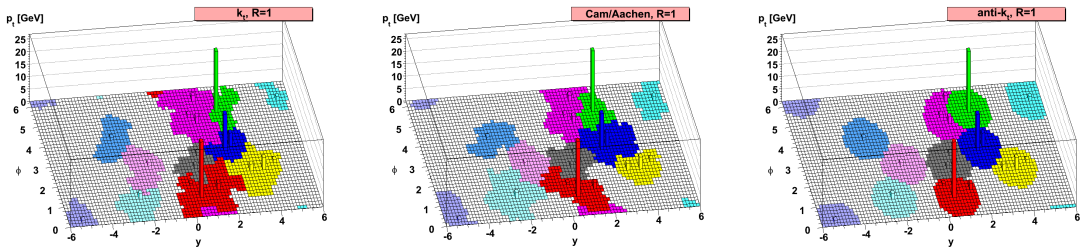


Figure II.3: Comparison of different jet-clustering algorithms applied to a sample parton-level event together with many random soft “ghosts” to illustrating the “active” catchment areas of the resulting hard jets. Taken from [31].

the physics of the hard process. While final-state radiation off the outgoing quarks and gluons has to be captured for an appropriate reconstruction, initial-state radiation from incoming color-charged particles should be removed. Additionally, UE provides a more or less smooth background of additional QCD activity. Its influence on the mass of a jet constructed with a cone size R is described by [32]

$$\langle \delta m_j \rangle \simeq \Lambda_{\text{UE}} p_{T,j} \left(\frac{R^4}{4} + \frac{R^8}{4608} + \mathcal{O}(R^{12}) \right), \quad (\text{II.19})$$

where Λ_{UE} denotes the amount of transverse momentum of the underlying event radiation and is for the LHC $\mathcal{O}(10 \text{ GeV})$. This problem is addressed by grooming techniques like filtering [33], pruning [34] or trimming [35] that try to reduce the contamination.

E. HEPTopTagging

The HEPTOPTAGGER is a tool that aims for the identification and reconstruction of hadronically decayed top quarks in a moderately-boosted phase-space regime. Starting from large-size jets (fat jets), it uses jet-substructure techniques to extract the top decay products. To decide whether these subjects are consistent with a top decay, it relies on invariant masses of subset combinations.

Since its first application [36] the HEPTOPTAGGER has been improved and modified several times [37–39]. In this section, we introduce the core of the HEPTOPTAGGER algorithm including the changed order of cuts introduced in Ref. [39]. This sets the stage for the extensions that are discussed in chapter III and App. A. For a complete discussion of the HEPTOPTAGGER2 algorithm, we refer to the appendix of Ref. [40]. An illustration of the individual steps is provided in Fig. II.4.

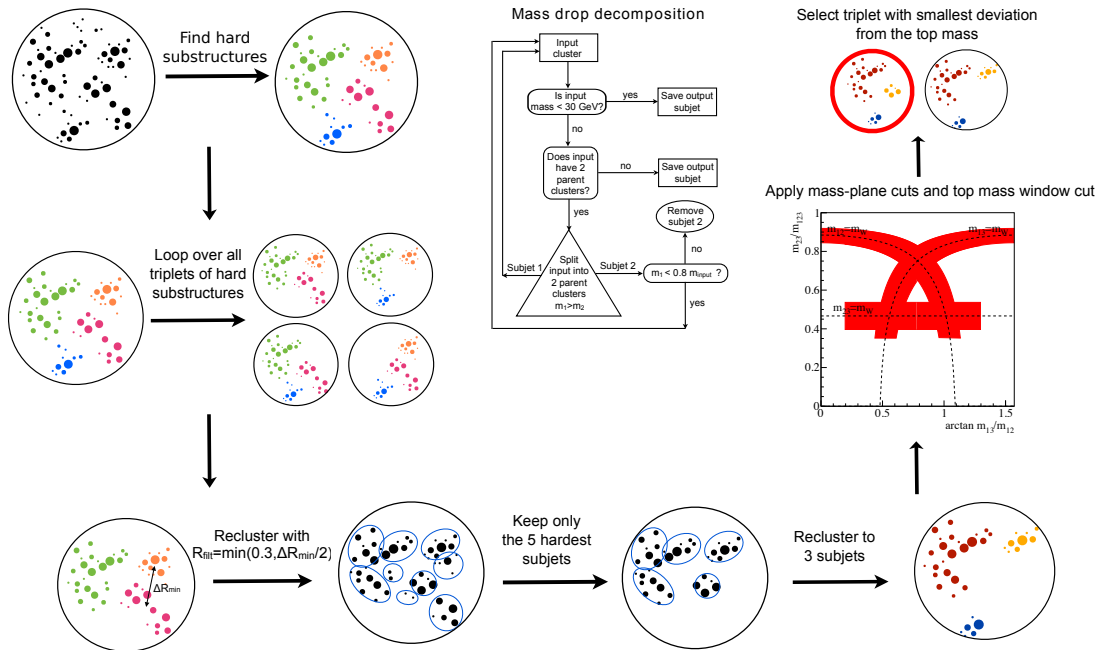


Figure II.4: Illustration of the HEPTOPTAGGER algorithm. The individual steps are discussed in the text. Adapted from Refs. [37, 41].

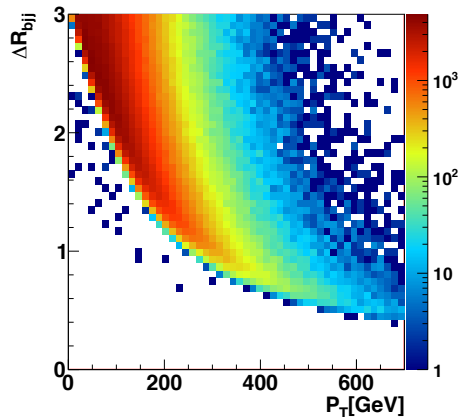


Figure II.5: Radius of C/A jets ΔR_{bjj} that should be able to capture all products of a hadronic top decay depending on the transverse momentum of the top quark. The color code provides the number of top quarks for the 14 TeV LHC with $\mathcal{L} = 10 \text{ fb}^{-1}$. Taken from Ref. [37].

If a top quark is at rest, its decay products will be widely separated making a reconstruction in a QCD-busy environment impossible. The situation changes if the top quark is boosted. Then, the decay products will be collimated and it might be possible to capture them in a fat jet. For SM top-pair production at the 14 TeV LHC, Fig. II.5 illustrates the correlation between the transverse momenta of the top quarks and the distance of their decay products R_{bjj} . The distance R_{bjj} corresponds to the size of a C/A jet that captures all three decay products, *i.e.* the distance of the third decay product to the combination of the two decay products with minimal separation ΔR . To access a maximal amount of top quarks, the size of the fat jet should be as large as possible. However, the contamination from initial-state radiation and UE increases dramatically with the jet size as was illustrated in Eq. (II.19).

The starting point for the HEPTOPTAGGER are fat C/A jets of large radii like $R = 1.5$ or $R = 1.8$ addressing top quarks with transverse momenta above 200 GeV. The actual algorithm proceeds in several steps:

1. hard substructures

Based on their clustering history, we stepwise decompose the fat jet looking for the two splittings $t \rightarrow Wb$ and $W \rightarrow jj$. The characteristic feature of these splittings is the drop in mass. Thus, we undo the last clustering step $j \rightarrow j_1 j_2$ with $m_{j_1} > m_{j_2}$. If the mass drop criterion $m_{j_1} < f_{\text{drop}} m_j$ with $f_{\text{drop}} = 0.8$ is fulfilled, both j_1 and j_2 are kept. Otherwise, we consider j_2 to originate from UE or initial-state radiation and

keep only j_1 . The decomposition is iterated until a soft cutoff $m_{j_i} > m_{\min} = 30$ GeV is reached.

2. filtering

Each triplet of hard substructures is filtered to remove contaminations from initial-state radiation or UE. Filtering reclusters the constituents of the triplet with a radius that is set based on the separation of the three hard substructures with an upper cutoff: $R_{\text{filt}} = \min(0.3, \Delta R_{jk}/2)$. Allowing for two final-state radiations off the top decay products, the $N_{\text{filt}} = 5$ hardest structures are then reclustered to three subjects which we label j_1, j_2 , and j_3 ordered by decreasing p_T . At this stage, all triplets that do not fulfill $m_{123} =: m_{\text{rec}} \in [150, 200]$ GeV are rejected.

3. mass-plane cuts

In addition to the requirement that m_{123} should reconstruct the top-quark mass, we can employ the fact that one pair of subjects should originate from a W boson while each subject is essentially massless. This yields the relation

$$m_t^2 = m_{123}^2 = m_{12}^2 + m_{13}^2 + m_{23}^2, \quad (\text{II.20})$$

which describes the surface of a sphere in three dimensions. We parametrize the surface by the two coordinates $\arctan(m_{13}/m_{12})$ and m_{23}/m_{123} . The condition that one m_{ij} should correspond to the W -boson mass, leads bands in the mass plane

$$\frac{m_{ij}}{m_{123}} = (1 \pm f_W) \frac{m_W}{m_t} = R_{\text{max,min}}, \quad (\text{II.21})$$

where $f_W = 0.15$ quantifies the allowed deviation from the expected value. These bands combine to a characteristic A-shape depicted in Fig. II.6. While in the mass plane for top candidates reconstructed from a $t\bar{t}$ signal the expected A is visible, the distributions in the W +jets and pure QCD jets background sample lead to additional cuts:

$$\text{if } m_{23} \sim m_W : \quad 0.2 < \arctan \frac{m_{13}}{m_{12}} < 1.3 \quad \text{else: } \frac{m_{23}}{m_{123}} > 0.35. \quad (\text{II.22})$$

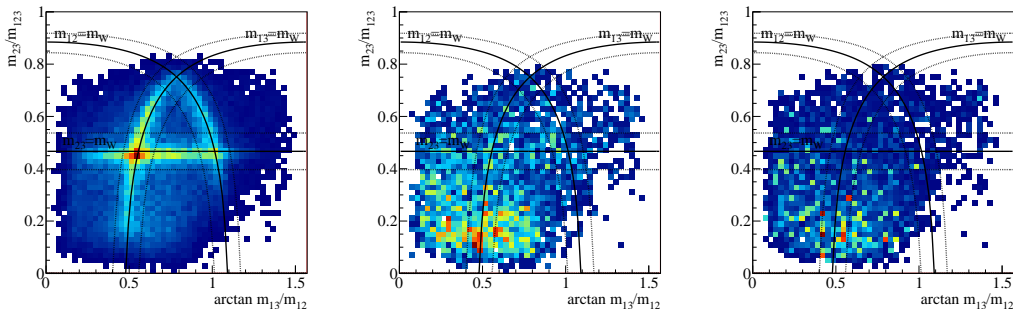


Figure II.6: Mass planes for $t\bar{t}$ (left), $W + \text{jets}$ (center), pure QCD jets sample (right). Simulations for the LHC with $\sqrt{s} = 14$ TeV. The color code illustrates the relative amount of top candidates (increasing from blue to red). Taken from Ref. [37].

The combination of all mass-plane cuts can be written as

$$\begin{aligned}
 0.2 < \arctan \frac{m_{13}}{m_{12}} < 1.3 \quad \text{and} \quad R_{\min} < \frac{m_{23}}{m_{123}} < R_{\max} & \quad (\text{II.23}) \\
 R_{\min}^2 \left[1 + \left[\frac{m_{13}}{m_{12}} \right]^2 \right] < 1 - \left[\frac{m_{23}}{m_{123}} \right]^2 < R_{\max}^2 \left[1 + \left[\frac{m_{13}}{m_{12}} \right]^2 \right] \quad \text{and} \quad \frac{m_{23}}{m_{123}} > 0.35 \\
 R_{\min}^2 \left[1 + \left[\frac{m_{12}}{m_{13}} \right]^2 \right] < 1 - \left[\frac{m_{23}}{m_{123}} \right]^2 < R_{\max}^2 \left[1 + \left[\frac{m_{12}}{m_{13}} \right]^2 \right] \quad \text{and} \quad \frac{m_{23}}{m_{123}} > 0.35 .
 \end{aligned}$$

4. triplet selection

Among all triplets passing this set of cuts we by default select the one that is closest to a true top quark in mass.*

5. consistency cut

Finally, the transverse momentum of the reconstructed top ($j_1 + j_2 + j_3$) has to exceed $p_{T,\text{rec}} > 200$ GeV to be consistent with the initial size of the fat jet.

While all studies in this thesis are based on Monte Carlo simulations, the ultimate performance test for such an algorithm is its application on real data. Figure II.7 illustrates a top mass peak obtained in an ATLAS study [42] using the HEPTOPTAGGER. Furthermore,

* This default choice can give rise to background sculpting. If one wants to reduce this at the expense of signal efficiency, there are alternative triplet selections like the summed modified jade distance [39] or the triplet obtained from the three hardest substructures.

the algorithm has been used by the ATLAS and CMS collaborations for several analyses including top quarks [43, 44].

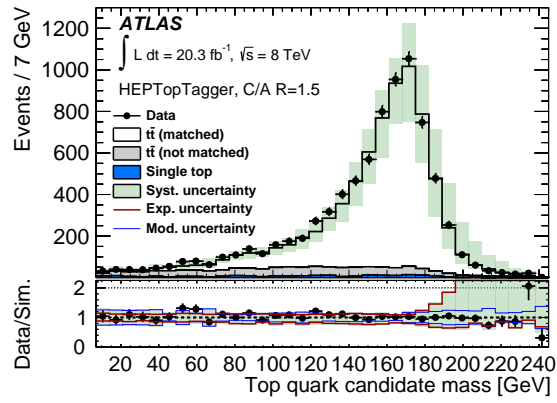


Figure II.7: Detector-level distribution of the mass of HEPTOPTAGGER top-quark candidates. Taken from Ref. [42].

F. Boosted decision trees

Top tagging is a typical (binary) classification problem. Based on a set of input variables, one wants to label an object as originating from a top decay or not. The classical approach to such a decision is a sequence of cuts on the variables. However, this approach cannot perform well in situations where the signal region in the space spanned by the variables is not a simple box.

An alternative approach are decision tree (DT) classifiers like the example shown in Fig. II.8. For classification, a series of successive yes-no criteria is employed, in which the next criterion depends on the previous decision. Selecting a single path from the top to the bottom results in a classical cut-based approach.

Throughout this thesis we rely on TMVA [45], a ROOT [46] environment for multivariate analyses, to construct appropriate classifiers. Therefore, we describe the particular implementation in TMVA in this section.

A generic procedure in the context of multivariate techniques is to bisect a dataset with known labels into a training and test sample. While the former is used to construct the classifier, the latter allows to test its performance. Separating these two tasks addresses the risk of overtraining, *i.e.* becoming sensitive to statistical fluctuations in the sample.

At each branching of the DT one wants to use the most decisive criterion to assign the remaining N_S signal and N_B background events of the training sample to the left (L) or right (R) branch. Therefore, the range of each variable is split into N_{cut} bins of equal size.

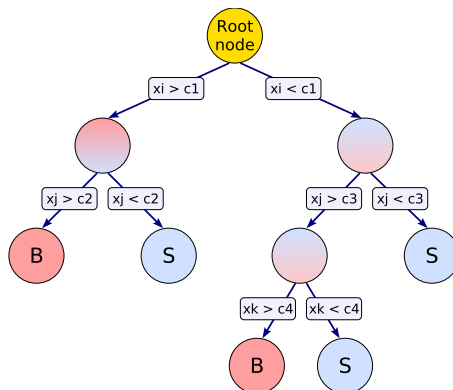


Figure II.8: Example for a decision tree. Starting from the root node an object follows a path according to the decisions at the individual nodes. Taken from Ref. [45].

Among all possible splittings the one with the maximum gain in separation

$$G = I(N_S, N_B) - \frac{N_S^L + N_B^L}{N_S + N_B} I(N_S^L, N_B^L) - \frac{N_S^R + N_B^R}{N_S + N_B} I(N_S^R, N_B^R) \quad (\text{II.24})$$

is selected, where $N_{S,B} = N_{S,B}^L + N_{S,B}^R$ and I denotes the Gini index

$$I(N_S, N_B) = \frac{N_S N_B}{(N_S + N_B)^2}. \quad (\text{II.25})$$

For simplicity we assume here events of equal weight. The splitting procedure can then be iterated until a predefined maximum depth of the tree is reached. A single branch is not split further once it exhibits a certain signal or background purity. The end points of a tree are called leaves and are assigned to one of the two categories depending on their actual purities. The obtained DT can now be used to predict the label for an object x as $y_{DT}(x) = \pm 1$ depending on what kind of leaf it ends up, where the upper (lower) sign corresponds to a classification as signal (background). Using the test sample we can quantify the rate of correctly identified signal events ϵ_S and the fraction of misidentified background events ϵ_B .

Stabler and more efficient classifiers are boosted decision trees (BDTs). In this context boosting means that the weights in the training sample are modified depending on the classification of the DT. More precisely, the ADABOOST algorithm [47] increases the weights of misclassified objects by

$$\alpha = \left(\frac{1 - r_{\text{false}}}{r_{\text{false}}} \right)^\beta, \quad (\text{II.26})$$

where r_{false} denotes the misclassification rate of the DT. The reweighted sample is then used to construct a second tree. This procedure can be iterated until a desired number of trees N_{trees} is reached. The amount of the reweighting can be controlled by the learning rate β . A typical choice is $\beta = 0.5$.

Instead of a predicted label, a BDT returns the weighted sum of outcomes of the individual trees

$$y_{\text{BDT}}(x) = \frac{1}{N_{\text{trees}}} \sum_i \log(\alpha_i) y_{DT_i}(x) \quad (\text{II.27})$$

which can be translated into a predicted signal probability. By scanning over the minimal signal probability required for classification as signal, one obtains a curve $\epsilon_B(\epsilon_S)$ known as receiver operating characteristic (ROC) curve.

III. RESONANCE SEARCHES WITH BOOSTED TOP QUARKS

The content of this chapter and the related App. A correspond to work done in collaboration with G. Kasieczka (ETH Zurich), T. Plehn (U Heidelberg), T. Strebler (ETH Zurich), and G. P. Salam (CERN) and is published as Ref. [40].

After the discovery of the Higgs boson, one main task at the LHC is the search for new physics beyond the Standard Model. Many models predict new heavy particles that can decay into pairs of top quarks [48]. An example are additional heavy neutral gauge bosons, called Z' bosons. Due to the large mass of the Z' bosons, the top quarks are boosted and thus their hadronic decay products are collimated to fat jets. This fact make Z' resonance searches a perfect application for substructure-based top taggers like the HEPTOPTAGGER. This reasoning is consistent with the first experimental HEPTOPTAGGER analysis being a Z' resonance search by ATLAS [43]. In this analysis results from the fully hadronic decay channel obtained with the HEPTOPTAGGER and the TEMPLATETAGGER [49] were comparable with the ones in the historically preferred semileptonic channel.

In the following, we want to improve such a $Z' \rightarrow t\bar{t}$ search based on boosted hadronic top quarks. Starting from a very simple analysis using the old HEPTOPTAGGER [36, 37] and a simple mass window cut on the invariant mass of the reconstructed tops, we will add several layers of improvements. In Sec. III A 3, we discard the fixed mass window and include additional kinematic information from the reconstructed top quarks in a multivariate analysis. Furthermore, we address effects of final-state radiation on the reconstruction. In addition, the multivariate setup is extended to overcome limitations from a fixed top-tagging working point. Algorithmic improvements and extensions of the old HEPTOPTAGGER are the focus of Sec. III B. Finally, we employ event deconstruction [50] as benchmark to compare our results against other proposed strategies in Sec. III C 2. Throughout this chapter, all results are discussed in context of the Z' resonance search. However, some improvements are directly connected to top tagging and lead to the new HEPTOPTAGGER2.[†] Therefore, the corresponding modifications and extensions are addressed separately in the context of ordinary top tagging in App. A.

[†] The HEPTOPTAGGER2 is available from: <http://www.thphys.uni-heidelberg.de/~plehn/index.php?show=heptoptagger&visible=tools>.

A. Resonance reconstruction

The current benchmark for heavy resonance searches using available information of boosted top quarks is event deconstruction [50]. To allow for a comparison in Sec. III C 2, the presented analyses follow the setup of Ref. [50]. A signal sample for the process $Z' \rightarrow t\bar{t}$ is generated with PYTHIA8 [51] where we set the mass of the new boson to $m_{Z'} = 1500$ GeV. Assuming the coupling structure of the Standard Model Z boson would result in a width $\Gamma(Z') = 47$ GeV. To match the assumptions and experimental resolution assumed in Ref. [50], we enforce pure vector couplings and increase the width to $\Gamma(Z') = 65$ GeV. As it will turn out later, this is of minor importance since the reconstruction will be limited to a larger width. For simplicity, we assume a branching ratio into tops of 100% throughout this study. The two relevant backgrounds are continuum top-pair and QCD dijet production. Both are generated with PYTHIA8 where we set a generator-level cut of $p_T \geq 400$ GeV on the top quarks and hard jets. We force all top-quark decays to be hadronic. Unless stated explicitly, we do not simulate pile-up or detector effects. A realistic performance test of all approaches has anyhow to rely on future experimental studies. For all optimizations we will focus on the pure QCD jets background which is by far the dominant one.

1. Decay kinematics

Since the mass of the considered Z' boson is much larger than twice the mass of a top quark, the top quarks will be boosted and give rise to fat jets. Thus, we require at least two fat jets constructed with the Cambridge-Aachen (C/A) algorithm [30] and a cone size of $R = 1.5$ using FASTJET [52]. Our analyses are based on the two hardest fat jets fulfilling

$$p_{T,\text{fat}} > 400 \text{ GeV} \quad \text{and} \quad |y_{\text{fat}}| < 2.5. \quad (\text{III.1})$$

Table III.1 provides the corresponding cut flow. The old default HEPTOPTAGGER [37] yields a double top-tagging efficiency of $\epsilon_{2\text{tags}} = 14\%$ for the signal sample. Applying a window on the invariant mass of the reconstructed top-quark pair $m_{t\bar{t}} \in [1200, 1600]$ GeV, leads to an overall Z' -tagging efficiency of $\epsilon_{Z'} = 10.2\%$. The mistagging rates for the $t\bar{t}$ background are $\epsilon_{2\text{tags}} = 13.7\%$ and $\epsilon_{Z'} = 3.3\%$. For the QCD jets background sample the double mistag rate is $\epsilon_{2\text{tags}} = 6.6 \cdot 10^{-4}$ and $\epsilon_{Z'} = 1.5 \cdot 10^{-4}$. At this point, the pure

	$Z' \rightarrow t\bar{t}$	$t\bar{t}$	QCD
generator level	10^5	10^5 (1.76 pb)	$8 \cdot 10^6$ (1.93 nb)
≥ 2 fat jets Eq.(III.1)	69142	85284 (1.50 pb)	$6.7 \cdot 10^6$ (1.62 nb)
hardest 2 fat jets HTT[JHEP1010] tagged	9679	11706 (0.21 pb)	4426 (1.07 pb)
$m_{t\bar{t}} \in [1200, 1600]$ GeV	7031	2817 (0.05 pb)	978 (0.24 pb)

Table III.1: Number of events and the corresponding PYTHIA8 cross section used for our analysis. The efficiencies $\epsilon_{S,B}$ for a Z' extraction are defined as the ratio of the last to the second line in this table.

QCD jets background rate dominates the continuum top-pair production by a factor five. Therefore, we focus on the QCD jets background for the rest of our analyses.

A possibility to improve this simple analysis is to replace the static mass window cut and consider the invariant mass $m_{t\bar{t}}$ and additional kinematic variables in a multivariate analysis using boosted decision trees, as implemented in TMVA [45]. The achievable performance of such an approach is illustrated in Fig. III.1 in terms of receiver operating characteristics (ROC) curves. The provided signal efficiencies ϵ_S are obtained from the Z' signal while the mistagging rates ϵ_B are based on the pure QCD jets background. The left panel of Fig. III.1 compares ROC curves starting from the invariant mass $m_{t\bar{t}}$. The fact that the corresponding ROC curve looks slightly worse than the working point of the old default HEPTOPTAGGER combined with the mass window $m_{t\bar{t}} \in [1600, 2000]$ GeV can be explained by a change in the order of cuts from the old default to the version of the tagger used for this comparison [39]. The changed order of cuts (mass-plane cuts before triplet selection) significantly reduces background sculpting at the expense of signal efficiency [39]. Background sculpting induces a major systematic error when looking for peaks in distributions and thus should be avoided. Once both versions are incorporated in a fully flexible multivariate setup, this difference vanishes.

Including additional variables in the multivariate analysis should improve their discriminational power, provided the variable adds new information. It should be emphasized that the HEPTOPTAGGER not only tags a fat jet as top, but returns a reconstructed four momentum of the top quark, that allows for a subsequent kinematical analysis. A possible observable that can be included in the multivariate analysis is the rapidity difference of the top quarks $|\Delta y|$. The corresponding signal and background distributions are provided in the left panel of Fig. III.1. While the shape of the Z' signal and the $t\bar{t}$ background are quite

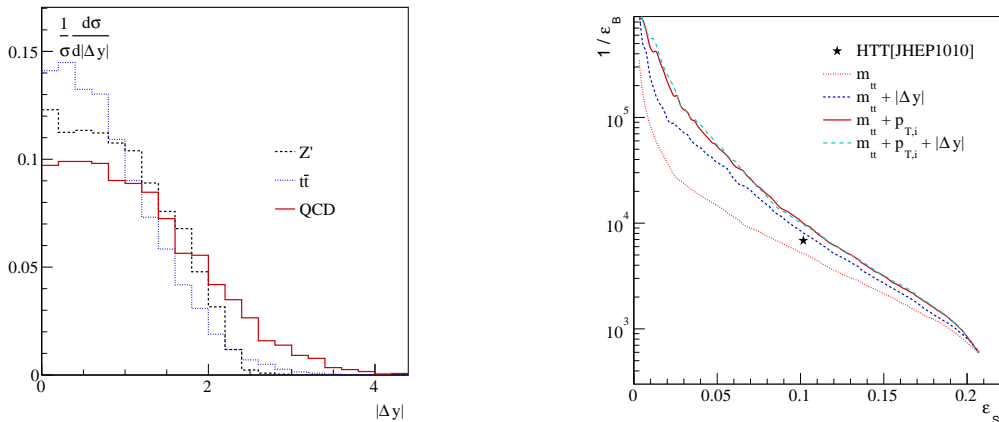


Figure III.1: Left: $|\Delta y|$ distribution of the reconstructed top quarks for signal and backgrounds. Right: ROC curves for the dominant QCD jets background vs. the Z' signal after including additional kinematic information shown in Eq.(III.2). As in all figures the asterisk corresponds to the original HEPTOPTAGGER described in Ref. [37]. Taken from Ref. [40].

similar, the extension of the QCD jets background to higher values of $|\Delta y|$ could be useful in a multivariate setup. Indeed, the corresponding ROC curve in the right panel of Fig. III.1 indicates a sizable improvement. Another obvious extension are the transverse momenta of the reconstructed top quarks $p_{T,i}$, which results in an even better performance. However, including $|\Delta y|$ on top of m_{tt} and the transverse momenta does not yield any further improvement. This indicates that there is no new information added, which is expected since the two-particle final state is essentially fully described. Thus, we can define a set of observables using only decay kinematics

$$\{ m_{tt}, p_{T,t_1}, p_{T,t_2} \} \quad (\text{decay kinematics}). \quad (\text{III.2})$$

2. QCD Jets

QCD effects beyond leading order are important to understand signal and backgrounds. Here, we provide a first estimate of the influence of final-state (FSR) and initial-state radiation (ISR) to our resonance search. The question how to deal with them is addressed in the next subsection.

A nice feature of using Monte Carlo simulations is that we can enable or disable certain parts of the simulation. This allows us to switch off ISR and FSR for the generation of signal events and thus investigate their influence on our analysis. Turning initial or

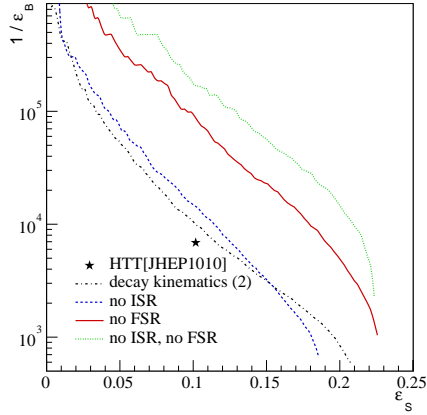


Figure III.2: ROC curves for different combinations of initial-state jet radiation (ISR) and final-state radiation (FSR) in the Z' signal generation. The background is QCD jets with ISR and FSR for all curves. Taken from Ref. [40].

final-state radiation off for the background is not sensible since additional QCD radiation is needed to obtain the sufficient jet multiplicity to fake top-quark decays. Figure III.2 depicts how deactivating ISR and/or FSR affects the ROC curves. The most striking effect is FSR spoiling the reconstruction of the signal, which will be addressed in the next subsection. The influence of initial-state radiation is twofold. On the one hand, it can give rise to additional soft jets that might be misidentified *e.g.* as the softer of the W -boson decay jets and thus worsens the top tagging and reconstruction. On the other hand, it can help since the recoil of the Z' boson against initial-state radiation changes the distribution of transverse momenta of the top quarks towards higher values. The latter effect is expected to be important for high signal efficiencies, which is reflected in the ROC curve. These observations indicate that a better treatment of QCD radiation could provide sizable improvements for the resonance reconstruction.

3. Final-state radiation

In contrast to other top taggers, the HEPTOPTAGGER reconstructs the four-vector of the tagged top quark. This directly allows to reconstruct $m_{Z'}$ as the invariant mass of the two top quarks. While the HEPTOPTAGGER is designed to capture final-state radiation off the top-quark decay products ($N_{\text{filt}} > 3$), the implemented mass cuts limit its usage to on-shell top quarks.

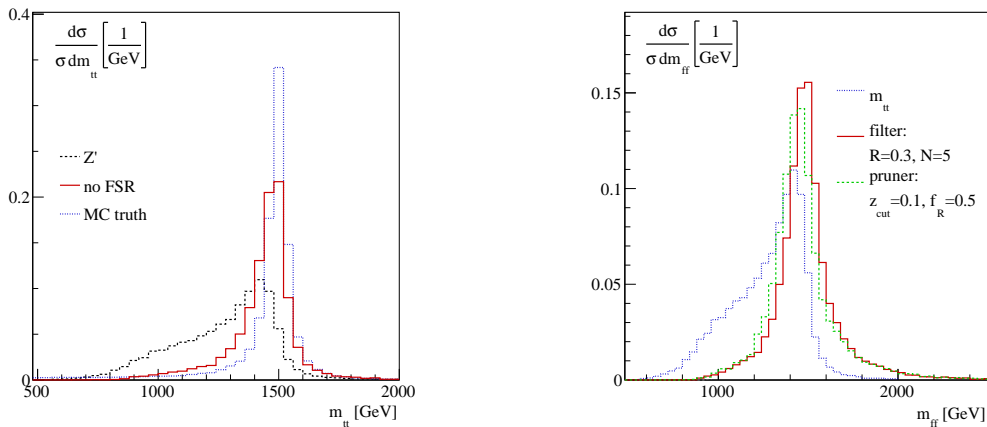


Figure III.3: Effect of final-state radiation on the invariant mass of the tagged and reconstructed $t\bar{t}$ system $m_{t\bar{t}}$ for the Z' signal (left) and different approaches to reconstruct the Z' mass peak (right). Monte Carlo truth is $\sqrt{p_{Z'}^2}$, with an assumed width of 65 GeV. Taken from Ref. [40].

However, the top quarks from Z' decays can be slightly off-shell and turn themselves on-shell by radiating off a hard gluon. This radiation is not captured when we reconstruct $m_{Z'}$ from the HEPTOPTAGGER top quarks and leads to a misalignment between the reconstructed and true mass of the Z' bosons. In particular, missing the gluon results in too small masses, while the top tagging itself remains unaffected. Accordingly, the reconstructed mass distribution in the left panel of Fig. III.3 exhibits an asymmetric tail toward small $m_{t\bar{t}}$. We can confirm this effect to be caused by final-state radiation by deactivating it during event generation: it removes the tail almost entirely. The remaining broadening and the minimal tail towards low masses is due to losses in the reconstruction of the top-quark four-momenta. We point out that the FSR tail becomes even more important for heavier Z' bosons.

Although the observed FSR tail is an issue for the reconstruction of heavy resonances, the task of the HEPTOPTAGGER is the identification and reconstruction of top quarks. Therefore, we will not modify the tagger but adjust the analysis strategy.

According to the discussion above, it should be possible to remove the asymmetric tail of the $m_{Z'}$ distribution by including kinematics of the fat jets in the analysis. We follow exactly the same analysis cuts as before but do not use the reconstructed four-momenta of the top quarks returned by the tagger. Instead, we can reconstruct the Z' boson from the top-tagged $R = 1.5$ C/A fat jets. Subjected to the influence of underlying event and initial-state radiation, the m_{ff} distribution peaks roughly at $m_{Z'}$ and has symmetric

	m_{peak} [GeV]	Γ [GeV]	$\epsilon_{Z'}^{\pm 150}$	$1/\epsilon_{tt}^{\pm 150}$	$1/\epsilon_{\text{QCD}}^{\pm 150}$
$m_{tt} \in [1200, 1600]$ GeV	–	–	0.136	22	2805
unfiltered	1539	167	0.141	21	1960
$R = 0.3, N = 4$	1457	152	0.146	28	2218
$R = 0.3, N = 5$	1477	144	0.150	25	2098
$R = 0.3, N = 6$	1489	139	0.151	25	2052
$R = 0.3, N = 7$	1496	144	0.151	24	2043
$R = 0.2, N = 5$	1443	140	0.141	29	2329
$R = 0.3, N = 5$	1477	144	0.150	25	2098
$R = 0.4, N = 5$	1500	144	0.151	24	2030
$R = 0.5, N = 5$	1515	143	0.148	23	1993
pruning $z = 0.1, f_R = 0.5$	1443	150	0.138	26	2075

Table III.2: Breit-Wigner fits and performance of different grooming approaches. The quoted efficiencies are based on a window for the invariant mass of the two filtered fat jets $|m_{\text{ff}} - m_{Z'}| < 150$ GeV.

tails. To obtain a stable result for the invariant mass of the two fat jets in an QCD-busy environment, we need to groom the fat jets. Our technique of choice is filtering [33], which essentially decreases the used jet area and therefore reduces the contamination from underlying event. The right panel of Fig. III.3 compares distributions of a filtered and a pruned version of the invariant mass based on the filtering and pruning routines provided within FASTJET [52]. For reference, we show again the invariant mass distribution of the top quarks' four-momenta. In contrast to the m_{tt} distribution, the groomed m_{ff} distributions have symmetric peaks around the Z' -boson mass. We confirm that grooming leads to stable results for the invariant mass by comparing several parameter settings in Tab. III.2. As characteristic parameters of the distributions we provide the peak position and the fitted Breit-Wigner width of the symmetric peaks as well as the reconstruction efficiencies for a fixed mass window of $|m_{\text{ff}} - m_{Z'}| < 150$ GeV. Using a Gaussian instead of a Breit-Wigner leads to similar results but a poorer modeling of the tails. The reconstructed widths lie around 145 GeV, roughly twice the value of the Monte Carlo width. In absence of detector effects, this value sets the resolution of mass reconstruction. Furthermore, Tab. III.2 indicates that replacing the cut on m_{tt} with a cut on a groomed version of m_{ff} does not improve the Z' signal extraction. The reason for this is that the shape of the background distributions in Fig. III.4 is changed as well. The m_{ff} distribution for the QCD

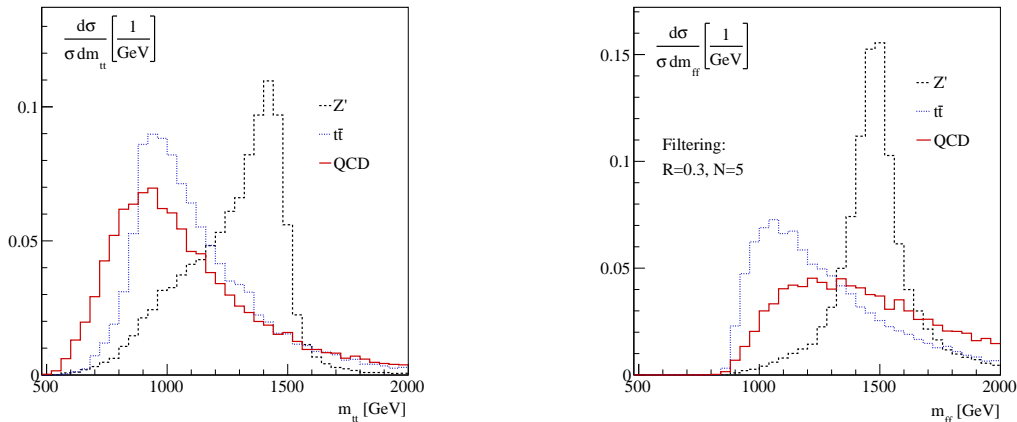


Figure III.4: Reconstructed mass distribution of the Z' signal and the backgrounds based on the tagged tops (left) and the corresponding filtered fat jets (right). Taken from Ref. [40].

jets background has its maximum around $m_{\text{ff}} = 1.3$ TeV, while the m_{tt} distribution exhibits a more pronounced maximum around $m_{tt} = 900$ GeV. The reason for this difference is the way that the top tagging removes QCD jets background events: First, the three assumed top decay products have to combine to the correct top-quark mass. Second, the combination of the two constructed tops has to fall in the mass window around the Z' -boson mass. Removing the first step leads to larger backgrounds at higher m_{ff} values.

To include final-state radiation and benefit from the additional information, we can use both m_{tt} and m_{ff} in the multivariate framework. Including kinematics of the fat jets this leads to the following set of variables describing the Z' decay

$$\{ m_{tt}, m_{\text{ff}}, p_{T,t_1}, p_{T,t_2}, p_{T,f_1}, p_{T,f_2} \} \quad (\text{filtered fat jets}). \quad (\text{III.3})$$

The used fat jets are filtered with a filter radius of $R = 0.3$ and keeping the $N = 5$ hardest substructures. Fig. III.5 depicts the corresponding ROC curves. In the left panel we show this time both the $t\bar{t}$ and QCD jets background. The improvement of using a multivariate approach for both backgrounds is obvious. For the QCD jets background, shown separately in the right panel, we find an improvement of a factor of 2 in $1/\epsilon_B$ at constant signal efficiency compared to the original HEPTOPTAGGER.

For the QCD jets background the combination of fat jet and mistagged top kinematics includes information beyond the hard process. For example, initial-state radiation, sensitive to the color structure of the signal and background, is captured in this combination. On

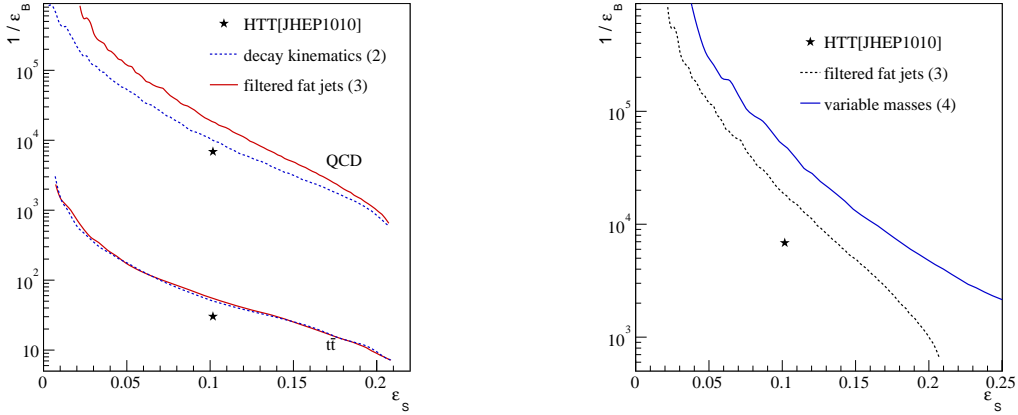


Figure III.5: Left: performance of the multivariate analysis including the information on the fat jet, as given in Eq.(III.2), Eq.(III.3) and Eq.(III.4). Only in this plot do we optimize for $t\bar{t}$ and QCD jets backgrounds separately. Right: performance curve for the full analysis only accounting for the dominant QCD jet background. Taken from Ref. [40].

the other hand, we construct the fat jets using standard jet clustering algorithms and our results are stable under different filter settings. Thus, we do not expect experimental problems relying on a working pile-up subtraction.

Up to this point the considered kinematic observables are based on the HEPTOPTAGGER output using a fixed working point. In general, the reconstruction of Z' bosons is limited by the efficiency to reconstruct the two top quarks and thus depends on the choice of working point. To allow for more flexibility, we open the mass window on the reconstructed top-quark mass. For each top candidate the mass reconstructed by the tagger can then be used as input for the multivariate analysis. In particular, we provide the smaller and the larger reconstructed top-quark mass as m_{rec}^{\min} and m_{rec}^{\max} . Similarly, we loosen the constraint on the ratio of the W -boson and top-quark mass f_W . The deviation from the true value is then an output of the tagger that we include in the multivariate analysis as f_{rec} . These modifications extent the set of variables to

$$\{ m_{tt}, m_{\text{ff}}, p_{T,t_1}, p_{T,t_2}, p_{T,f_1}, p_{T,f_2}, m_{\text{rec}}^{\min}, m_{\text{rec}}^{\max}, f_{\text{rec}}^{\max} \} \quad (\text{variable masses}). \quad (\text{III.4})$$

The corresponding ROC curve in the right panel of Fig. III.5 illustrates that going beyond the fixed HEPTOPTAGGER working point increases the range of achievable signal efficiencies. In particular, we can receive efficiencies up to $\epsilon_S = 56\%$. Compared to the old default

HEPTOPTAGGER working point combined with a fixed mass window around the Z' -boson mass, the improvements of the last sections result in a five-times better background rejection at constant signal efficiency.

B. Updated tagger

During LHC run I, fat jets with large cone size of $R = 1.5$ or $R = 1.8$ have been established as analysis objects. Those jets are large enough to capture the decay products of heavy particles. If a particle of mass m decays to two subjets, their separation can be estimated to $\Delta R_{ij} \sim 2m/p_T$. Thus, the geometrical size of the fat jets sets a limit on the accessible range of transverse momenta of the heavy particle. Consequently, any tagger should allow for jets as large as possible. However, with the size of the fat jet the contamination from underlying event and pile-up gets more and more problematic. As grooming step, filtering [33] has been an essential ingredient all versions of the HEPTOPTAGGER. By reducing the effectively used size of the fat jet, it decreases the problem of underlying event and not entirely removed pile-up. Another issue is initial-state radiation which enters the fat jet and complicates the combinatorics during the reconstruction of the top quark. A typical ISR jet can mimic e.g. the softer W -boson decay jet and thus leads to a wrongly reconstructed four-momentum. Such so-called type-2 tags containing only two correct top decay products have been studied in the context of less boosted top quarks [39]. Their occurrence can be reduced by harder reconstruction cuts which, however, lower the tagging rate. At higher boosts like in the reconstruction of heavy new particles, the used radii of the fat jets are too large and consequently should be adjusted. In the next section, we introduce an adaptive cone size for the HEPTOPTAGGER, the optimalR mode. In addition, this procedure yields a new powerful observable to discriminate between fat jets originating from top quark decays and those arising from QCD jets backgrounds. Finally, we demonstrate how the tagging can be improved further by employing N -subjettiness [53].

1. *OptimalR mode*

The idea of an adjustable jet size is not new [54–56], but none of them lead to a dramatically improved tagger.[‡] In this section, we rely on a purely algorithmic approach to find an adequate size of the fat jet [60]. In principle, there is an optimal fat-jet size R_{opt} at which all top decay products are captured. A smaller fat jet would miss relevant parts of the decay and thus cannot reconstruct the top quark correctly. A larger fat jet, instead, would capture all relevant decay products, but contain an unnecessary large amount of contamination from ISR, the underlying event and pile-up. The idea of the optimalR mode is to determine R_{opt} by starting from a large fat jet, say $R = 1.5$, and stepwise reduce the size of the fat jet. At each R , we run the usual HEPTOPTAGGER to reconstruct a top-quark candidate. If reducing the cone size splits the fat jet into several smaller fat jets, we only consider the hardest one for further deconstruction. As long as the used radius is larger than the optimal value, the tagger should be able to return an almost stable result for the reconstructed top quark. Once the algorithm passes R_{opt} from above, the lack of relevant parts of the decay results in a change of the reconstructed four-momentum. With decreasing radius we therefore expect a stable plateau of reconstructed top-quark mass until R_{opt} is passed. This allows us to algorithmically extract R_{opt} via

$$\frac{m_{\text{rec}}^{(1.5)} - m_{\text{rec}}(R)}{m_{\text{rec}}^{(1.5)}} > 0.2 \quad \Leftrightarrow \quad R < R_{\text{opt}}. \quad (\text{III.5})$$

The final output of the tagger is then the four-momentum reconstructed at $R = R_{\text{opt}}$. As smallest value for the cone size we set $R = 0.5$ and point out that this value can and has to be adjusted for studies of tops with large boosts $p_{T,t} \gtrsim 1$ TeV. For now, the cutoff should avoid experimental problems due to the resolution of the calorimeter, but has to be tested in full detector simulation by ATLAS and CMS. In our analysis we typically obtain values around $R_{\text{opt}} = 0.6$ in the signal sample.

In addition to the algorithmic procedure outlined above, we can estimate the expected value for R_{opt} from a fit to Monte Carlo data. For this purpose, we simulate Standard Model

[‡] Recently, the new HOTVR tagger [57] relying on Mass Jump [58] and VariableR [56] claimed to yield better performance than the HEPTOPTAGGER2 for transverse momenta above 1 TeV. However, they rely on a fixed working point and the used parameters are not adjusted to the considered boost. A comparison of the two approaches in a multivariate framework is in preparation [59].

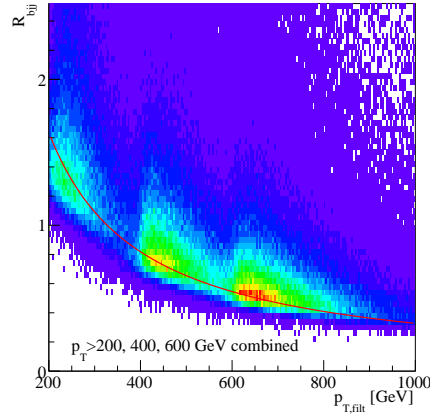


Figure III.6: $R_{\text{opt}}^{(\text{calc})}$ fit based on Standard Model $t\bar{t}$ samples with $p_{T,t} > 200, 400, 600$ GeV for the parton-level distance of decay products R_{bjj} . The fat jets are filtered with $R = 0.2$, $N = 10$. The functional form of the fit curve is given by $R_{\text{opt}}^{\text{calc}} = 327 \text{ GeV}/p_{T,\text{filt}}$. Taken from Ref. [40].

top-pair production with hadronic top decays using PYTHIA8. To increase the statistics at higher transverse momenta, we combine samples with $p_T > 200, 400, \text{ and } 600$ GeV. From these samples we can derive a relation between the distance of the expected cone size R_{bjj} and the kinematics of the corresponding fat jet, in particular its transverse momentum. To achieve stable results for the fat jets, we filter them using $R_{\text{filt}} = 0.2$ and keeping the ten hardest substructures. This choice of parameters turns out to perform best for our purposes [60]. However, the final choice has to be left to experimental optimizations. To obtain the desired relation, we fit $R_{\text{opt}}^{(\text{calc})} \propto 1/p_{T,\text{filt}}$ to the data. From the fit in Fig. III.6, we estimate the optimal cone size as $R_{\text{opt}}^{\text{calc}} = 327 \text{ GeV}/p_{T,\text{filt}}$. While for true top quarks the estimated value $R_{\text{opt}}^{\text{calc}}$ and the algorithmically found R_{opt} should be close, for a QCD jet faking a top-quark decay this is not the case. Therefore, we can gain additional information from the deviation $R_{\text{opt}} - R_{\text{opt}}^{(\text{calc})}$. However, we note that $R_{\text{opt}}^{(\text{calc})}$ might be strongly correlated with other observables that are already included in Eq.(III.6). Including the larger of the two deviations increases the set of observables for the BDT to

$$\{ m_{tt}, m_{\text{ff}}, p_{T,t_1}, p_{T,t_2}, p_{T,f_1}, p_{T,f_2}, m_{\text{rec}}^{\text{min}}, m_{\text{rec}}^{\text{max}}, f_{\text{rec}}^{\text{max}}, R_{\text{opt}} - R_{\text{opt}}^{(\text{calc})} \} \quad (\text{optimalR}), \quad (\text{III.6})$$

where we evaluate all HEPTOPTAGGER outputs at R_{opt} . The gain in performance is shown in Fig. III.7. For small signal efficiencies there is no improvement within numerical fluctuations. At larger signal efficiencies, however, we observe a significant improvement.

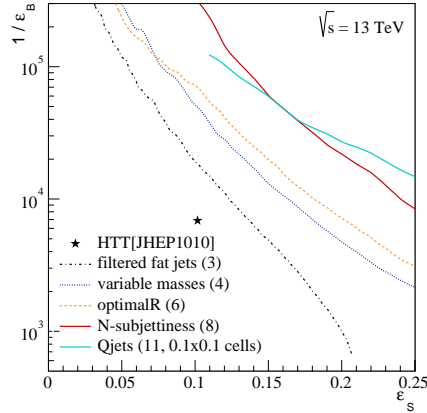


Figure III.7: Performance of the optimalR mode based on the kinematic variables in Eq.(III.6), including N -subjettiness variables as defined in Eq.(III.8), and including QJETS. As described in the text, for QJETS we need to require a finite calorimeter resolution, while all other curves do not include any detector effects. We only consider the dominant QCD jets background. Taken from Ref. [40].

2. N -subjettiness

The most straightforward question that one might ask in the context of jet substructure is: how many hard subjets are contained inside a jet? In other words, is the jet consistent with a N -prong decay? A quantity that measures exactly this property is N -subjettiness [53, 61]. The basic idea behind it is to construct a set of N axes and measure how consistent the constituents can be assigned to them. N -subjettiness quantifies this as

$$\tau_N = \frac{1}{R_0 \sum_k p_{T,k}} \sum_k p_{T,k} \min(\Delta R_{1,k}, \Delta R_{2,k}, \dots, \Delta R_{N,k}) . \quad (\text{III.7})$$

For each constituent of the (fat) jet it determines the minimal distance to any of the N axes. The sum of the distances to the nearest axis measures how well the jet is described by N or less axes. The p_T -weighting emphasizes the importance of hard substructures. Conventionally, the sum is normalized by the sum over all transverse momenta. The parameter R_0 is usually set to the size of the (fat) jet to guarantee $\tau_N \in [0, 1]$. Since small τ_N indicates consistency with N or less axes, the ratio τ_N/τ_{N-1} serves as a probe of the N -pronginess of the (fat) jet and has been used as a tagger itself.

Including the first three τ_N calculated for each of the fat jets both filtered and unfiltered yields an amazing improvement of the ROC curve shown in Fig. III.7. The set of observables

now includes

$$\left\{ m_{tt}, m_{\text{ff}}, p_{T,t_1}, p_{T,t_2}, p_{T,f_1}, p_{T,f_2}, m_{\text{rec}}^{\min}, m_{\text{rec}}^{\max}, f_{\text{rec}}^{\max}, R_{\text{opt}} - R_{\text{opt}}^{(\text{calc})}, \tau_{1,N}, \tau_{1,N}^{(\text{filt})}, \tau_{2,N}, \tau_{2,N}^{(\text{filt})} \right\} \quad (N\text{-subjettiness}). \quad (\text{III.8})$$

A more detailed explanation of the used quantities is provided in App. A.

3. Qjets

A major limitation of substructure based tagging algorithms is the restriction to a deterministic sequence of clustering steps (clustering history). As described in Sec. IID, the jet clustering is a purely algorithmic procedure that tries to reverse the physical process of additional QCD radiations. However, there can be situations in which the jet clustering does not do its job well enough and leads to an inappropriate jet. In such cases the reconstruction of a top quark has to fail right from the beginning. A possibility to overcome this limitation in signal efficiency is to consider not just a single history per fat jet. One approach that allows for the construction of several clustering histories together with a statistical interpretation is QJETS [62]. To construct a jet, the usual clustering algorithms iteratively combine the closest pair of prejets based on a given metric d_{ij} . In the C/A jet algorithm this is their geometric separation $d_{ij} = \Delta R_{ij}$. QJETS associates in each clustering step all possible clusterings of prejet pairs (i,j) with a weight

$$\omega_{ij}^{(\alpha)} = \exp\left(-\alpha \frac{d_{ij} - d_{ij}^{\min}}{d_{ij}^{\min}}\right) \quad (\text{III.9})$$

and randomly selects a splitting according to these weights. To balance the aim of alternative jet clusterings and the convergence of the clustering, we choose a rigidity of $\alpha = 0.1$. The deterministic clustering is restored in the limit $\alpha \rightarrow \infty$. Multiplying the weights of all selected merging steps leads to a global weight for the entire clustering history

$$\Omega^{(\alpha)} = \prod_{\text{mergings}} \omega_{ij}^{(\alpha)} = \left[\prod_{\text{mergings}} \exp\left(-\frac{d_{ij} - d_{ij}^{\min}}{d_{ij}^{\min}}\right) \right]^{\alpha} \xrightarrow{\text{consistent}} 1. \quad (\text{III.10})$$

This weight is limited by the deterministic cluster sequence with $\Omega = 1$ independent of α . The intrinsic probabilistic behavior of the algorithm allows for the generation of a whole

set of possible clustering histories. For our studies we limit the size of these sets to 100 clustering histories per fat jet, each with its own weight Ω . If the deterministic clustering corresponds to a reasonable history for a signal event, we expect the outcome of the tagger using this history to be close to the one clustering history with the largest global weight.

One situation in which QJETS can help is when the deterministic jet clustering picks an intermediate merging that is minimal with respect to d_{ij} but is not well motivated by QCD. By definition this clustering history has the maximum weight $\Omega = 1$. Another clustering history, which might be more consistent with QCD, can reach a similarly large weight. From the set of alternative clustering histories, we can pick the subset which leads to top tags and large global weights. In this analysis, we select the two positively tagged clustering histories with largest weights. Therefore, we can correct for a possibly misled deterministic cluster sequence. Especially for large signal efficiencies, we expect a benefit from the approach, because in this regime the effect of wrong clustering histories becomes limiting. In addition, we can extract statistical information from the 100 QJETS histories. First of all, we label the fraction of histories that result in a top tag as ϵ_{Qjets} . Secondly, we characterize the reconstructed top mass distribution $m_{\text{rec}}^{\text{Qjets}}$ of the ϵ_{Qjets} tagged histories in terms of its first and second moment. Adding this information to the set of observables for the multivariate analysis finally leads to

$$\left\{ m_{tt}, m_{\text{ff}}, p_{T,t_1}, p_{T,t_2}, p_{T,f_1}, p_{T,f_2}, m_{\text{rec}}^{\min}, m_{\text{rec}}^{\max}, f_{\text{rec}}^{\max}, \right. \\ \left. R_{\text{opt}} - R_{\text{opt}}^{(\text{calc})}, \{\tau_N\}, \epsilon_{\text{Qjets}}^{\min}, \{m_{\text{rec}}^{\text{Qjets}}\} \right\} \quad (\text{QJETS}), \quad (\text{III.11})$$

where $\{\tau_N\}$ stands as a shorthand for the N -subjettiness values used in Eq. (III.8). From the two top candidates, we only consider the smaller value for ϵ_{Qjets} . All other variables are evaluated at R_{opt} for the highest weighted clustering histories. The obtained ROC curve is given in Fig. III.7. In contrast to all analyses above, this time we precluster the event to $(\eta \times \phi)$ cells of size (0.1×0.1) . This detector resolution limits the number of clustering steps and therefore reduces the number of possible clustering histories to a manageable level. Because this preclustering is not done for the analyses before, the QJETS ROC curve does not exceed the previous ROC over the entire range. However, we still observe the expected improvement towards larger signal efficiencies.

C. Full event information

Finally, we have to compare the performance of the HEPTOPTAGGER2 to other approaches designed for the LHC. As benchmark we compare against the projection of event deconstruction for a Z' resonance search [50]. As discussed in Sec. IID, the hard process and QCD jet radiation are blurred when we include *e.g.* filtered subjet information or N -subjettiness. Therefore, we first study briefly the information from additional jets in the entire event before comparing against the leading proposal for Z' analyses.

1. Additional jets

To estimate the difference in the jet structure of Z' signal processes and the QCD jets background, we cluster the hadronic event into small $R = 0.2$ C/A jets with $p_T > 10$ GeV. This choice corresponds to the micro-jets which constitute the starting point of event deconstruction. While it is not clear whether such jets can be meaningfully used at the LHC, here we use them to capture a maximum amount of information. Without analysis cuts, the number of jets in a signal event is set by the three decay products of each top quark and additional ISR and FSR jets. The number of jets and their kinematics should allow to separate different processes in an inclusive event sample [63].

After a first level of cuts, both the Z' signal and the $t\bar{t}$ background peak at 10 micro-jets in Fig. III.8, *i.e.* six top decay products and four additional jets from initial or final-state radiation. The QCD jets background exhibits a maximum at slightly larger number of jets, which is expected since the scale of the hard process is also generated through a large number of jets. Furthermore, the leading jet in the signal tends to be harder than for the backgrounds. These jet patterns might be useful in a multivariate analysis, however, the contained information would be heavily correlated with the variables used in the HEPTOPTAGGER.

Instead, we can study the jet activity that does not contribute to the top candidates. During top tagging the typical subjets are of size $R = 0.3$ and $p_T \gtrsim 20$ GeV after filtering. To obtain the unused hadronic activity, we remove all calorimeter data that ends up in the final top candidates and recluster the remnants into micro-jets. As shown in the lower row of Fig. III.8, the number of obtained postjets for the signal peaks around 2, indicating two jets

that do not originate from final-state radiation off the top decay products. The distribution of transverse momenta of the hardest postjet peaks for the signal and $t\bar{t}$ background at small values corresponding to soft initial-state radiation. For the QCD jets background the distribution has its maximum around $p_{T,j} = 50 - 200$ GeV. This is still small compared to the scale set by the fat jets but could provide additional information that can be used in a BDT analysis. However, the ROC curves in the right panel of Fig. III.8 indicate only a negligible gain in performance by adding postjet information to the set of variables defined in Eq.(III.3). Almost all information of the additional jet radiation is already contained in the combined analysis of the reconstructed tops and the corresponding fat jets.

This observation backs up the assumption that additional jet information inside and outside the fat jets has no major influence on the stable tagging results of the updated tagger. Consequently, we can compare the HEPTOPTAGGER2 with other multivariate approaches.

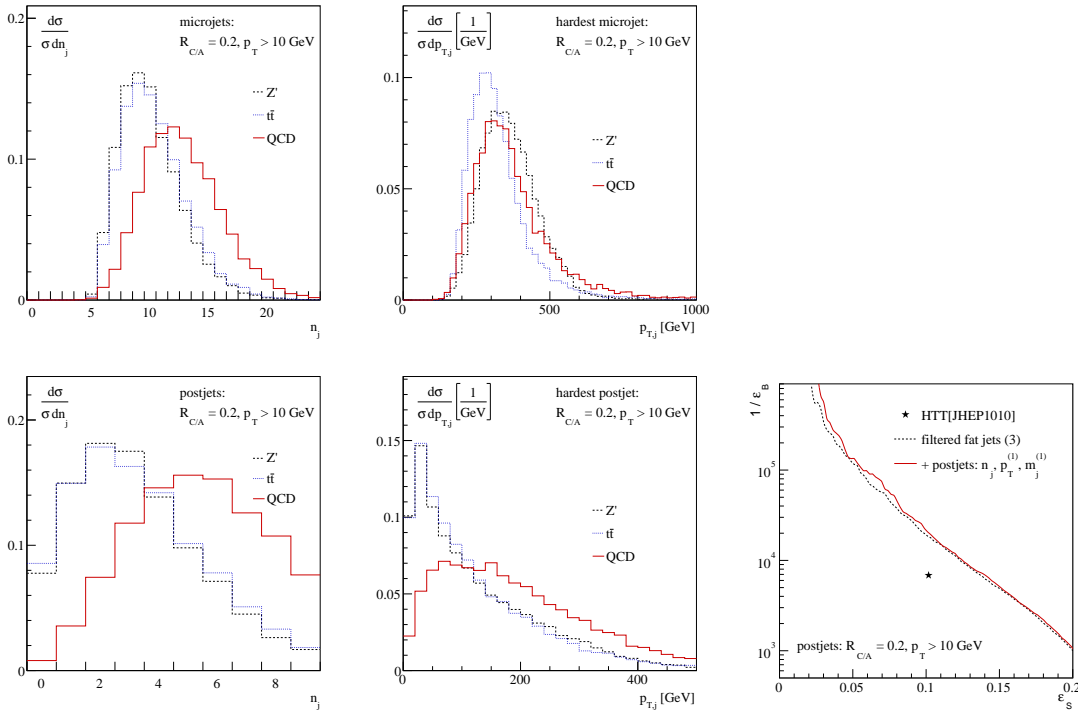


Figure III.8: Information on the hardest jet before top tagging (upper row) and the hardest jet remaining after top tagging (lower row). For the jets defined with $R = 0.2$ and $p_T > 10$ GeV we show the number of jets, the hardest jet's transverse momentum, and ROC curves illustrating the gain in performance by including information from the postjets. Taken from Ref. [40].

2. Comparison with other approaches

One of the most promising proposals for boosted top-quark identification and $t\bar{t}$ resonance searches at the LHC are shower deconstruction [64] and event deconstruction [50]. The basic idea is to construct likelihoods representing possible shower histories for a jet or a fat jet. The fundamental objects in these analyses are C/A micro-jets with $R = 0.2$ and $p_T > 10$ GeV [50]. Although these jets are slightly softer and smaller than the ones typically used in taggers, our observations in the last section indicate that this should not make a significant difference. In contrast to general template methods, shower deconstruction relies on the soft and/or collinear approximation of QCD to compute the likelihood for a given shower history in terms of Sudakov factors and splitting probabilities. The obtained likelihood ratio is then used to decide whether a fat jet originated from a top-quark decay or QCD jets background. Like other probabilistic approaches, shower deconstruction does not separate classification and reconstruction and thus, unlike the HEPTOPTAGGER, does not yield a reconstructed four-momentum for the top quark.

The Z' resonance search using event deconstruction relies on two C/A fat jets of size $R = 1.5$ fulfilling the criteria of Eq. (III.1). Each fat jet is then reclustered to micro-jets, of which up to the hardest nine are used to calculate the corresponding likelihoods. For the Z' analysis not only the likelihood separating top-quark jets from QCD jets is

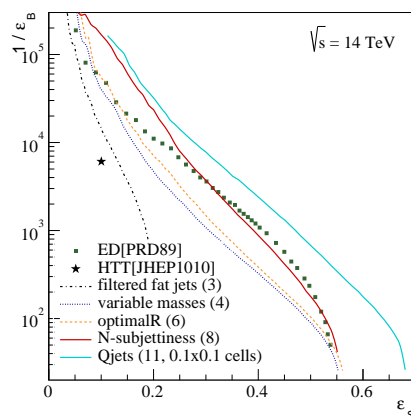


Figure III.9: Comparison of the multivariate HEPTOPTAGGER2 analysis presented in this thesis with the event deconstruction approach of Ref. [50]. All HEPTOPTAGGER2 curves correspond to Fig. III.7, but now with a collider energy of 14 TeV instead of 13 TeV, This comparison in the absence of an experimental validation should be taken as first estimate. Taken from Ref. [40].

taken into account but in addition the event likelihood differentiates between resonant and non-resonant production of the fat-jet pair. For the hard process this approach is similar to the established matrix element method [65] and replaces the analysis of m_{tt} and $p_{T,t}$. Following Ref. [50] we assume a width of the Z' boson of 65 GeV. However, the exact value is secondary for our analysis since its resolution is limited to a reconstructed width around 145 GeV, as was shown in Tab. III.2. Figure III.9 provides a comparison of the analysis developed in the previous sections with event deconstruction. In contrast to Fig. III.7, we show signal efficiencies up to 68% illustrating the extension of achievable signal efficiencies using QJETS. Furthermore, the shown results are obtained for 14 TeV center-of-mass energy allowing for a direct comparison to the event deconstruction efficiencies of Ref. [50]. Both event deconstruction and the new deterministic HEP_{TOP}TAGGER2 perform comparably over a wide range of signal efficiencies. Of course, the final answer on both methods has to be subject of a full experimental study based on real data.

D. Conclusions

In the past sections, we improved a plain $Z' \rightarrow t\bar{t}$ resonance search using the old HEPTOPTAGGER by modifying the tagging algorithm and adding several kinematic observables to a multivariate analysis. Considering fat jet kinematics allowed us to account for final-state radiation in resonance searches. Moreover, we introduced an algorithmically optimized size of the original fat jet combined with its prediction (optimalR mode). Further improvements were achieved by probing more general subjet structures inside the fat jet using N -subjettiness. Finally, QJETS provided a global picture of the most likely clustering histories giving a top tag. For the outlined Z' search, we achieved an increased background rejection by a factor 30 for a constant Z' tagging efficiency of 10%. These results are at least competitive with the leading estimates for other tagging methods.

Except for the fat jet kinematics, all these improvements can be incorporated in the top tagging algorithm leading to the new HEPTOPTAGGER2. The corresponding improvements for top tagging are discussed in App. A, where we test the new tagger for moderate ($p_T > 200$ GeV) and sizable ($p_T > 600$ GeV) boosts. Especially, for large boosts we find significant improvements compared to the old HEPTOPTAGGER.

IV. MEASURING THE TOP YUKAWA COUPLING AT A FUTURE HADRON COLLIDER

This chapter presents work done in collaboration with M. L. Mangano (CERN), T. Plehn (U Heidelberg), P. Reimitz (U Heidelberg), and H. S. Shao (CERN) that is published as Ref. [66]. Especially the credit for the studies of the theoretical uncertainties has to go to the our collaborators from CERN.

Besides searches for new particles, it is a primary tasks of the following LHC runs to test the nature of the Higgs boson. Especially the top Yukawa coupling y_t is of major interest. Due to its large size, it dominates the renormalization group evolution of the Higgs potential to higher energy scales [21]. However, y_t is very hard to determine directly at colliders [13, 67], since it requires a precise measurement of the production cross section of a Higgs boson associated with a pair of top quarks ($t\bar{t}H$). In principle, this process can be studied at hadrons colliders [36, 68, 69] as well as at e^+e^- machines [12, 70], provided they exceed the required center-of-mass energy of 500 GeV. The expected precisions for the determination of the Higgs couplings at the LHC and the proposed International Linear Collider (ILC) [71] are depicted in Fig. IV.1. Should a future e^+e^- Higgs factory not fulfill this requirement, the measurement of y_t will be left as a task for future hadron-hadron colliders. Candidates for a 100 TeV proton-proton collider are the FCC-hh [72] at CERN and the SppC [73] in China. Such a hadron collider could shed some light on weakly interacting thermal dark matter [75], the Standard Model gauge sector at high

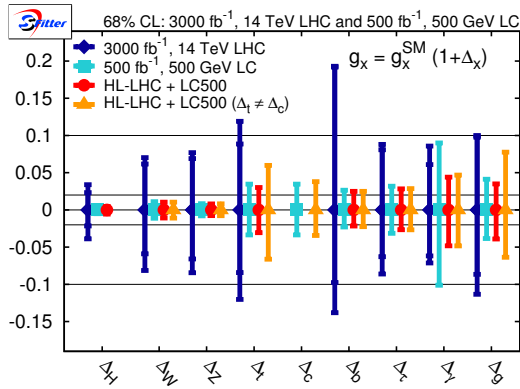


Figure IV.1: Expected precision in the determination of Higgs couplings at the high-luminosity LHC and the ILC ($\sqrt{s} = 500$ GeV). Taken from [12].

energies [76], the electroweak phase transition [77] and the hierarchy problem. In addition, high precision studies of the Higgs boson will be an important part of the physics program.

While it is unclear whether and when such a machine will be built, it is important to estimate the feasibility and reach of proposed measurements. First studies indicate that the Higgs self-coupling could be determined with a precision of 5 to 10% with an integrated luminosity of 30 ab^{-1} [78]. The fact that already for the high-luminosity LHC the extraction of Higgs couplings is expected to be limited by theoretical and systematic uncertainties [79] limits the possibility for extrapolations. An important exception is the measurement of $t\bar{t}H$ production, which will still be limited by statistics.

In this chapter, we illustrate that a future 100 TeV proton-proton collider will allow for a precision measurement of $t\bar{t}H$ production. The main feature compared to the LHC is the increased rate of events at larger boosts of the top quarks and the Higgs bosons. This enables us to exhaust features of boosted objects and jet substructure [80]. The changes in the transverse momentum distributions at a 100 TeV collider compared to the LHC are illustrated in Fig. IV.2. Our analysis is based on the first HEPTOPTAGGER application to semileptonic $t\bar{t}H$ Higgs boson decaying to a pair of b -quarks [36]. There are several differences of the presented 100 TeV analysis compared to the original LHC study.

First, we benefit from the hugely increased statistics at a 100 TeV collider with an expected integrated luminosity of $\mathcal{O}(10 \text{ ab}^{-1})$. From Fig. IV.2 we expect, for example, around 10 million events with $p_{T,H} > 500 \text{ GeV}$ in 10 ab^{-1} . The improved statistics allows

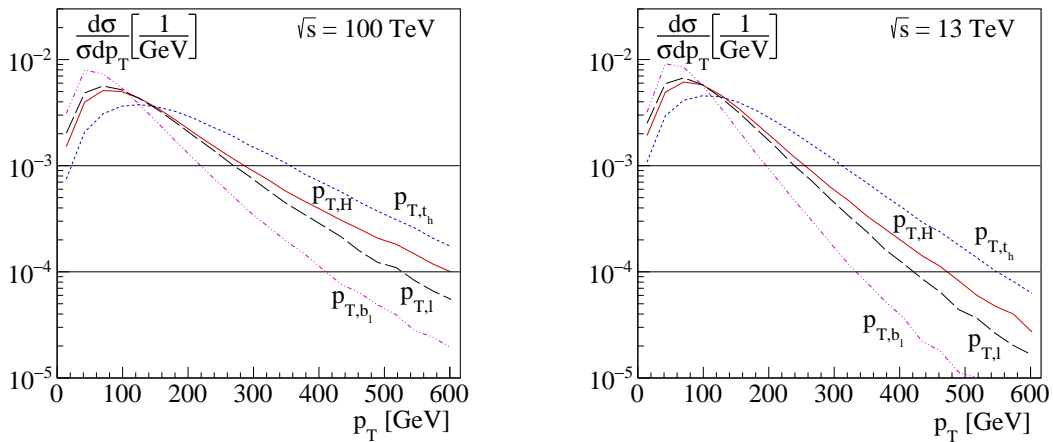


Figure IV.2: Transverse momentum distributions for the $t\bar{t}H$ signal process at a 100 TeV collider (left) and the 13 TeV LHC (right). Taken from version 1 of Ref. [66].

for a comparison to the similarly peaked $t\bar{t}Z, Z \rightarrow b\bar{b}$ background which reduces systematic and theoretical uncertainties. The next section illustrates that the cross-section ratio $\sigma(t\bar{t}H)/\sigma(t\bar{t}Z)$ comes with very small theoretical uncertainties which are at the percent level already today.

Secondly, the change of the transverse momentum spectra towards higher p_T provides a large fraction of events that can be investigated with default boosted tagging techniques as shown in Sec. II E.

Finally, the improvements in the HEPTOPTAGGER2 outlined in chapter III and their application on the BDRS Higgs tagger [33] will allow us to reduce background sculpting and increase the signal statistics. Using these improvements in Sec. IV C, we find that the ratio of the fiducial cross section of $t\bar{t}Z$ and $t\bar{t}H$ can be measured with percent level statistical precision. Assuming negligible BSM contamination in the $t\bar{t}Z$ production, this measurement probes the product of the top Yukawa y_t and the $H \rightarrow b\bar{b}$ branching ratio to 1% precision. In the likely case that a 100 TeV collider is preceded by an e^+e^- Higgs factory, the branching ration $B(H \rightarrow b\bar{b})$ will be known to better than 1% [73, 81–83] and the suggested measurement would provide a direct measurement of the top Yukawa coupling.

A. Theoretical systematics for the $t\bar{t}H/t\bar{t}Z$ production rate

While the great benefit of hadron colliders are the immense statistics, there is the intrinsic problem to perform accurate absolute rate predictions. A major difficulty is the complexity and size of higher-order corrections. Next-to-leading-order (NLO) calculations come often with uncertainties of order 10%. For gg -initiated processes these can be much larger, especially for Higgs or $b\bar{b}$ production. Including NNLO contributions, the uncertainties can in many cases be reduced to the percent level. Another issue are the uncertainties of the gluon parton distribution function (PDF) which range from a few percent to order one for extremal values of the proton momentum fraction x . Additional uncertainties arise from the modeling of realistic final states. The precision that can be reached in inclusive parton-level calculations has to be folded with hadronization and analysis cuts. Finally, for some processes the achievable precision is limited by the knowledge of input parameters, e.g. the masses of heavy quarks.

In the past years, there has been significant progress in theoretical precision [84]. For example, the inclusive Higgs production from the gg initial state has been calculated to NNNLO [85]. Combined with improvements in the estimation and the consistency of the gluon PDF [86], the uncertainty on the total production rate reached $3\%_{\text{NNNLO}} \oplus 3\%_{\text{PDF}}$. Similar precision could be reached for the $t\bar{t}$ production rate at NNLO [87]. Of course, it is hard to predict the theoretical progress until a 100 TeV collider might be operational. However, upcoming LHC measurements will provide validation of available calculations and parton distributions such that it is reasonable to assume that all Higgs production processes should be known to the level of 1% or better theoretical accuracy.

Despite this expectation, it is useful to explore observables that are more robust with respect to systematics and allow measurements where experimental systematics can be reduced to the size of the theoretical ones. Here, we propose the ratio of $t\bar{t}H$ and $t\bar{t}Z$ cross sections in fiducial regions of acceptance suitable for an experimental analysis. In the next subsections, we illustrate that this ratio can be predicted with percent-level accuracy already today based on the theoretical understanding of the processes including NLO QCD [88–90] and electroweak (EW) [91, 92] corrections, and the current knowledge of PDFs. Certainly, this precision will be consolidated and improved until a 100 TeV collider is built. The next subsections are dedicated to motivate this accuracy claim.

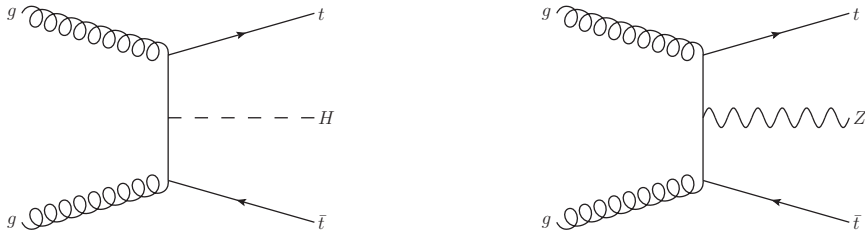


Figure IV.3: Example Feynman diagrams for the dominant gg -initiated contribution to $t\bar{t}H$ and $t\bar{t}Z$ production.

1. Total rates and ratios

The benefit of considering the ratio of $t\bar{t}H$ and $t\bar{t}Z$ is based on the close analogy of the two processes. At leading order both are dominated by the gg initial state with the Higgs or the Z boson emitted off the top line. For illustration, Fig. IV.3 provides example Feynman diagrams. A difference between the two processes is that in the qq initial state the Z boson can be radiated off the initial light quarks. At 13 TeV the qq initial state amounts for $\lesssim 30\%$ of the total cross section; at 100 TeV it is reduced to $\lesssim 10\%$. We show below that this difference has no large effect and is further reduced at 100 TeV. The similarity of tree-level diagrams leads to similar relevant diagrams at NLO. Consequently, renormalization, factorization, and the cancelation of soft and collinear divergences are highly correlated. Therefore, we can relate the choice of the renormalization and factorization scales within the estimate of scale uncertainties. Obviously, uncertainties from the top-quark mass are fully correlated between the two processes. Another feature is the closeness of the Higgs and Z -boson mass resulting in similar x values being probed. This fact and the necessity to synchronize the PDF choice between the two processes when considering their ratio leads to a significant reduction of the PDF systematics. Finally,

	$\sigma(t\bar{t}H)$ [pb]	$\sigma(t\bar{t}Z)$ [pb]	$\frac{\sigma(t\bar{t}H)}{\sigma(t\bar{t}Z)}$
13 TeV	$0.475^{+5.79\%+3.33\%}_{-9.04\%-3.08\%}$	$0.785^{+9.81\%+3.27\%}_{-11.2\%-3.12\%}$	$0.606^{+2.45\%+0.525\%}_{-3.66\%-0.319\%}$
100 TeV	$33.9^{+7.06\%+2.17\%}_{-8.29\%-2.18\%}$	$57.9^{+8.93\%+2.24\%}_{-9.46\%-2.43\%}$	$0.585^{+1.29\%+0.314\%}_{-2.02\%-0.147\%}$

Table IV.1: Total cross sections $\sigma(t\bar{t}H)$ and $\sigma(t\bar{t}Z)$ and the ratios $\sigma(t\bar{t}H)/\sigma(t\bar{t}Z)$ with NLO QCD corrections at 13 TeV and 100 TeV. Results are presented together with the renormalization/factorization scale and PDF+ α_s uncertainties. Taken from Ref. [66].

		$\sigma(t\bar{t}H)$ [pb]	$\sigma(t\bar{t}Z)$ [pb]	$\frac{\sigma(t\bar{t}H)}{\sigma(t\bar{t}Z)}$
13 TeV	MSTW2008	$0.475^{+5.79\%+2.02\%}_{-9.04\%-2.50\%}$	$0.785^{+9.81\%+1.93\%}_{-11.2\%-2.39\%}$	$0.606^{+2.45\%+0.216\%}_{-3.66\%-0.249\%}$
	CT10	$0.450^{+5.70\%+6.00\%}_{-8.80\%-5.34\%}$	$0.741^{+9.50\%+5.91\%}_{-10.9\%-5.29\%}$	$0.607^{+2.34\%+0.672\%}_{-3.47\%-0.675\%}$
	NNPDF2.3	$0.470^{+5.26\%+2.22\%}_{-8.58\%-2.22\%}$	$0.771^{+8.97\%+2.16\%}_{-10.6\%-2.16\%}$	$0.609^{+2.23\%+0.205\%}_{-3.41\%-0.205\%}$
100 TeV	MSTW2008	$33.9^{+7.06\%+0.94\%}_{-8.29\%-1.26\%}$	$57.9^{+8.93\%+0.90\%}_{-9.46\%-1.20\%}$	$0.585^{+1.29\%+0.0526\%}_{-2.02\%-0.0758\%}$
	CT10	$32.4^{+6.87\%+2.29\%}_{-8.11\%-2.95\%}$	$55.5^{+8.73\%+2.16\%}_{-9.27\%-2.78\%}$	$0.584^{+1.27\%+0.189\%}_{-1.99\%-0.260\%}$
	NNPDF2.3	$33.2^{+6.62\%+0.78\%}_{-6.47\%-0.78\%}$	$56.9^{+7.62\%+0.75\%}_{-7.29\%-0.75\%}$	$0.584^{+1.29\%+0.0493\%}_{-2.01\%-0.0493\%}$

Table IV.2: Results with NLO QCD corrections at 13 TeV and 100 TeV, using three different sets of PDFs. Results are presented together with the renormalization/factorization scale and PDF uncertainties. Contrary to Tab. IV.1, the α_S systematics is not included here.

similar (although not identical) production kinematics should lead to further reduction of systematics in the final-state modeling like e.g. shower-induced higher-order corrections, underlying-event, and hadronization.

We can quantify the qualitative arguments using MADGRAPH5_AMC@NLO [93], which includes both NLO QCD and EW corrections. The default parameter set used in this study is:

Parameter	value	Parameter	value
G_μ [GeV ⁻²]	$1.1987498350461625 \cdot 10^{-5}$	n_{f}	5
m_t [GeV]	173.3	$y_t v / \sqrt{2}$ [GeV]	173.3
m_W [GeV]	80.419	m_Z [GeV]	91.188
m_H [GeV]	125.0	α^{-1}	128.930

As default PDF we rely on MSTW2008 NLO [94] and set $\mu_R = \mu_F = \mu_0 = \sum_{f \in \text{final states}} m_{T,f}/2$ for the central choice of renormalization and factorization scales, where $m_{T,f}$ is the transverse mass of the final particle f . This scale choice interpolates between the dynamical scales that were shown in Ref. [88] to minimize the p_T dependence of the NLO/LO ratios for the top and Higgs spectra.

We start this discussion with results at LO in the electroweak (EW) effects. To quantify the scale dependence, we vary μ_R and μ_F over the usual range $0.5\mu_0 \leq \mu_{R,F} \leq 2\mu_0$.

		$\sigma(t\bar{t}H)$ [pb]	$\sigma(t\bar{t}Z)$ [pb]	$\frac{\sigma(t\bar{t}H)}{\sigma(t\bar{t}Z)}$
13 TeV	default	$0.475^{+5.79\%}_{-9.04\%}$	$0.785^{+9.81\%}_{-11.2\%}$	$0.606^{+2.45\%}_{-3.66\%}$
	$\mu_0 = m_t + m_{H,Z}/2$	$0.529^{+5.96\%}_{-9.42\%}$	$0.885^{+9.93\%}_{-11.6\%}$	$0.597^{+2.45\%}_{-3.61\%}$
	$m_t = y_t v/\sqrt{2} = 174.1$ GeV	$0.474^{+5.74\%}_{-9.01\%}$	$0.773^{+9.76\%}_{-11.2\%}$	$0.614^{+2.45\%}_{-3.66\%}$
	$m_t = y_t v/\sqrt{2} = 172.5$ GeV	$0.475^{+5.81\%}_{-9.05\%}$	$0.795^{+9.82\%}_{-11.2\%}$	$0.597^{+2.45\%}_{-3.65\%}$
	$m_H = 126.0$ GeV	$0.464^{+5.80\%}_{-9.04\%}$	$0.785^{+9.81\%}_{-11.2\%}$	$0.593^{+2.42\%}_{-3.62\%}$
100 TeV	default	$33.9^{+7.06\%}_{-8.29\%}$	$57.9^{+8.93\%}_{-9.46\%}$	$0.585^{+1.29\%}_{-2.02\%}$
	$\mu_0 = m_t + m_{H,Z}/2$	$39.0^{+9.76\%}_{-9.57\%}$	$67.2^{+10.9\%}_{-10.6\%}$	$0.580^{+1.16\%}_{-1.80\%}$
	$m_t = y_t v/\sqrt{2} = 174.1$ GeV	$33.9^{+7.01\%}_{-8.27\%}$	$57.2^{+8.90\%}_{-9.42\%}$	$0.592^{+1.27\%}_{-2.00\%}$
	$m_t = y_t v/\sqrt{2} = 172.5$ GeV	$33.7^{+6.99\%}_{-8.31\%}$	$58.6^{+8.93\%}_{-9.46\%}$	$0.576^{+1.27\%}_{-1.99\%}$
	$m_H = 126.0$ GeV	$33.2^{+7.04\%}_{-8.28\%}$	$57.9^{+8.93\%}_{-9.46\%}$	$0.575^{+1.25\%}_{-1.95\%}$

Table IV.3: Results with NLO QCD corrections at 13 TeV and 100 TeV for varying some parameter values. Results are presented together with the renormalization/factorization scale uncertainties.

Of course, the scale choice for the numerator and denominator has to be synchronized. Table IV.1 provides the scale and PDF $+\alpha_s$ uncertainties for the MSTW 2008 NLO PDF set. Uncertainties of $\pm 7 - 10\%$ for the individual total cross sections are reduced to $\pm 1.5\%$ ($\pm 3\%$) for the ratios at 100 (13) TeV. The effect of PDF variation is reduced by a factor of ten in the ratio to a few per mille. To validate the stability of the ratio, we study different PDF sets using LHAPDF 5.9.1 [95]. Table IV.2 provides the results for MSTW2008 NLO [94], CT10 NLO [96] and NNPDF2.3 NLO [97] PDFs. Here we focus only on the PDF variation, and not the α_s systematics. For all PDF choices the predictions for the individual rates vary in the $\pm 5\%$ range and are reduced to the few-per-mille level in the ratio.

To quantify the uncertainties connected to the value of the input parameters in Tab. IV.3, we vary them without considering PDF uncertainties, since these should be practically unaffected by those parameters. Fixing the central scale to $\mu_0 = m_t + m_{H,Z}/2$ modifies the ratio $\sigma(t\bar{t}H)/\sigma(t\bar{t}Z)$ by $1\% - 1.5\%$, which is covered by the estimated range using the dynamical scale choice. Changing the top-quark mass within $m_t = 173.3 \pm 0.8$ GeV leaves $\sigma(t\bar{t}H)$ practically constant. This can be understood by the anti-correlation between

		$\sigma(t\bar{t}H)$ [pb]	$\sigma(t\bar{t}Z)$ [pb]	$\frac{\sigma(t\bar{t}H)}{\sigma(t\bar{t}Z)}$
13 TeV	$m_t = 174.1$ GeV	0.3640	0.5307	0.6860
	$m_t = 172.5$ GeV	0.3707	0.5454	0.6800
100 TeV	$m_t = 174.1$ GeV	23.88	37.99	0.629
	$m_t = 172.5$ GeV	24.21	38.73	0.625

Table IV.4: LO results at 13 TeV and 100 TeV, keeping the top Yukawa coupling $y_t v/\sqrt{2} = 173.3$ GeV.

the effects on the strength of the top Yukawa coupling y_t and the available phase space. The approximate cancelation is not possible in $t\bar{t}Z$ resulting in a variation at the level of $\pm 1.5\%$ which directly translates into the ratio. If we fix the top Yukawa coupling while changing the mass, only the phase-space effect is left. Consequently, the ratio remains constant within a few percent as shown in Tab. IV.4 and is almost only sensitive to the value of y_t . Estimating the dependence on the Higgs mass by changing it ± 1 GeV yields a $\sim 2\%$ shift in $\sigma(t\bar{t}H)$ and in the ratio. Note however, that this variation overestimates the uncertainty to which the Higgs mass is known [98]. Certainly, the value of m_H will be determined to higher precision in the near future.

The effect of next-to-leading-order EW corrections in the $\alpha(m_Z)$ scheme is illustrated in

		$\alpha(m_Z)$ scheme			G_μ scheme		
		$\sigma(t\bar{t}H)$ [pb]	$\sigma(t\bar{t}Z)$ [pb]	$\frac{\sigma(t\bar{t}H)}{\sigma(t\bar{t}Z)}$	$\sigma(t\bar{t}H)$ [pb]	$\sigma(t\bar{t}Z)$ [pb]	$\frac{\sigma(t\bar{t}H)}{\sigma(t\bar{t}Z)}$
13 TeV	NLO QCD	0.475	0.785	0.606	0.462	0.763	0.606
	$\mathcal{O}(\alpha_S^2\alpha^2)$ Weak	-0.006773	-0.02516		0.004587	-0.007904	
	$\mathcal{O}(\alpha_S^2\alpha^2)$ EW	-0.0045	-0.022		0.0071	-0.0033	
	NLO QCD+Weak	0.468	0.760	0.617	0.467	0.755	0.619
	NLO QCD+EW	0.471	0.763	0.617	0.469	0.760	0.618
100 TeV	NLO QCD	33.9	57.9	0.585	32.9	56.3	0.585
	$\mathcal{O}(\alpha_S^2\alpha^2)$ Weak	-0.7295	-2.146		0.0269	-0.8973	
	$\mathcal{O}(\alpha_S^2\alpha^2)$ EW	-0.65	-2.0		0.14	-0.77	
	NLO QCD+Weak	33.1	55.8	0.594	32.9	55.4	0.594
	NLO QCD+EW	33.2	55.9	0.594	33.1	55.6	0.595

Table IV.5: Effect of EW NLO corrections, in the $\alpha(m_Z)$ and G_μ schemes, at 13 TeV and 100 TeV.

Tab. IV.5. They result in a shift of order 2% compared to the pure NLO QCD result. For reference, we also provide results in the G_μ scheme using $\alpha^{-1} = 132.50699632834286$ and $G_\mu = 1.166390 \cdot 10^{-5}$. The difference to the $\alpha(m_Z)$ scheme is at the percent level for the individual rates and at the per-mille level for the ratios. Thus, we can conclude that after NLO EW corrections the residual uncertainty of the cross-section ratio due to higher-order EW effects should be well below the percent level.

Finally, we want to point out that at LO the renormalization and factorization scales appear only in the PDFs and $\alpha_S(\mu_R)$. Since the numerical values for the scales of the two processes are very close, the obtained scale uncertainties at LO are unreliably optimistic. At NLO the appearance of kinematical factors of Q^2 in the renormalization logarithms $\log(\mu_R^2/Q^2)$ give rise to relevant differences between the two processes. Additionally, one obtains NLO diagrams that differ between the processes that contribute to finite NLO terms like e.g. light quark loops coupling to the Z boson, but not to the Higgs. Such effects can not be covered by scale variations. In general, there is no guarantee that higher-order contributions do not exceed the range estimated by scale variations. Consequently, one should demand that the uncertainties we have estimated above have to be confirmed by a full NNLO calculation that certainly will be possible in the next few years.

2. Kinematical distributions

Any actual analysis, especially boosted ones like the one we suggest here, restrict the phase space of final states. Therefore, it is necessary to check whether the precision obtained for the fully inclusive cross section carries over to the description of the final state including kinematic cuts. We limit our studies to the most relevant kinematical distributions for our analysis and the main source of uncertainty, *i.e.* scale and PDF uncertainties. In Fig. IV.4 we study the ratio of integrated transverse momentum spectra for different final-state objects X . The left panel shows the dependence on a minimum transverse momentum cut on the Higgs or the Z boson. In the central panel the cut is applied on the top quarks. The right panel applies the cut on the $t\bar{t}$ system. All ratios are normalized to the corresponding ratio value without a cut. Thus, the provided uncertainties correspond directly to the systematics in the extrapolation of the ratio of the differential distributions

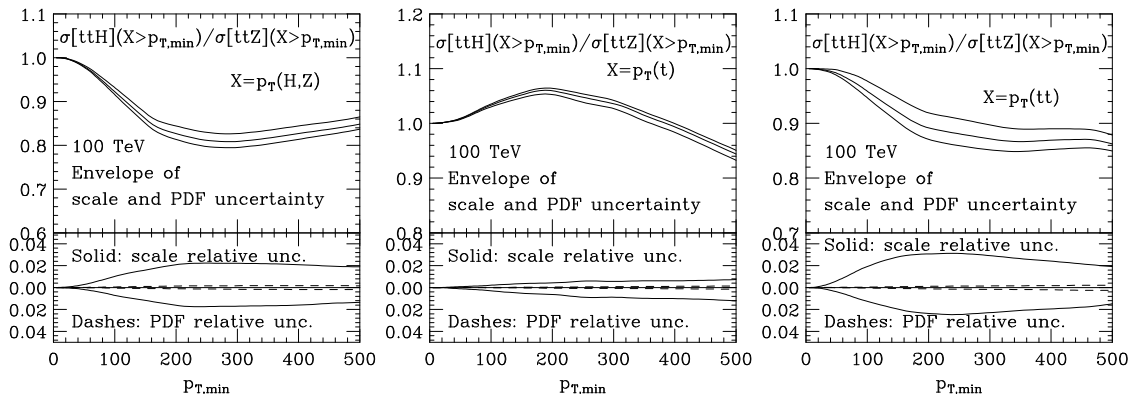


Figure IV.4: Scale and PDF systematics of ratios of integrated p_T spectra for different observables, at 100 TeV. From left to right: p_T of the boson, p_T of the top quark, p_T of the $t\bar{t}$ pair. Taken from Ref. [66].

to the total rates. The upper parts of the plots indicate that the ratios are not constant w.r.t. to the applied p_T cuts. They change by up to 20% using cuts up to $p_T = 500$ GeV. The lower parts provide the relative uncertainties split up into the ones obtained by scale variation and those from PDF variation within the MSTW2008 NLO set. The scale uncertainties reach $\pm 2\%$ for the boson p_T spectra, $\pm 1\%$ for the top and $\pm 3\%$ for the p_T of the $t\bar{t}$ system. In all considered cases, the PDF uncertainties remain well below the percent level.

B. Boosted $t\bar{t}H$ at 100 TeV

In principle, there are many Higgs decay channels that might be considered to study $t\bar{t}H$ production. Table IV.6 provides the corresponding event numbers assuming an integrated luminosity of 20 ab^{-1} at a future 100 TeV proton-proton collider. The given numbers include branching ratios for the semileptonic decay of the top-quark pair, *i.e.* $t\bar{t} \rightarrow \ell\nu_\ell + \text{jets}$ ($\ell = e, \mu$). These numbers are typically reduced by a factor of 10 or more due to analysis cuts and efficiencies. Therefore, the clean decay channel to four leptons does not yield the number of 10^4 events needed for a precision of 1%. To estimate the decay to two photons (see also Ref. [99]) a simple parton-level analysis with basic cuts

$$\begin{aligned} p_{T,\gamma,b,j} > 25 \text{ GeV}, & \quad |\eta_{\gamma,b,j}| < 2.5, & \quad \Delta R_{jj,bb,bj} > 0.4, \\ p_{T,\ell} > 20 \text{ GeV}, & \quad |\eta_\ell| < 2.5, & \end{aligned} \quad (\text{IV.1})$$

leaves around $5 \cdot 10^4$ events in 20 ab^{-1} . The $t\bar{t}\gamma\gamma$ background fulfilling $|m_{\gamma\gamma} - 125| < 5 \text{ GeV}$ is almost a factor of 10 smaller. Considering lepton and photon isolation and b -tagging makes this channel borderline for an analysis at the percent level and should be subject of a dedicated study including detector effects. Additionally, the decay to photons has the intrinsic possibility of BSM contributions to the loop. The decay $H \rightarrow 2\ell 2\nu$ has a potentially interesting rate, which may deserve a separate study. Here, we employ the dominating decay $H \rightarrow b\bar{b}$. Following the original LHC analysis [36], we study

$$pp \rightarrow t\bar{t}H \rightarrow (bjj) (\bar{b}\ell\bar{\nu}) (b\bar{b}), (b\ell\nu) (\bar{b}jj) (b\bar{b}). \quad (\text{IV.2})$$

The leptonic top decay yields a lepton that can be used for triggering and reduces the multi-jet combinatorics. The leading backgrounds for this signature are:

$pp \rightarrow t\bar{t}b\bar{b}$, the main irreducible QCD background

$H \rightarrow 4\ell$	$H \rightarrow \gamma\gamma$	$H \rightarrow 2\ell 2\nu$	$H \rightarrow b\bar{b}$
$2.6 \cdot 10^4$	$4.6 \cdot 10^5$	$2.0 \cdot 10^6$	$1.2 \cdot 10^8$

Table IV.6: $t\bar{t}H$ event numbers for various Higgs decay modes, with 20 ab^{-1} at 100 TeV, assuming $t\bar{t} \rightarrow \ell\nu + \text{jets}$, $\ell = e, \mu$.

$pp \rightarrow t\bar{t}Z$, including the Z -peak in the m_{bb} distribution

$pp \rightarrow t\bar{t}$ +jets with fake-bottoms tags

Further backgrounds like W +jets are small and do not yield dangerous kinematical features [36]. For our analysis we rely on boosted Higgs and top decays leading to a quite simple analysis strategy:

1. an isolated lepton
2. a tagged top without any b -tag requirement
3. a tagged Higgs with two b -tags inside
4. a continuum b -tag outside the top and Higgs fat jets

The obtained m_{bb} distribution provides large sidebands that allow us to control the $t\bar{t}b\bar{b}$ and $t\bar{t}$ +jets backgrounds. In addition, it yields a second peak corresponding to the Z boson. The need for a continuum b -tag is discussed below.

For simplicity, all simulations are performed at leading order. The effect of higher order corrections [88–90, 100, 101] have been discussed before and are left out for this signal-background analysis. All samples are generated with MADGRAPH5 [102] with NNPDF23 parton densities [103], showering and hadronization via PYTHIA8 [51] and a fast detector simulation with DELPHES3 [28, 104]. On generator level we require $p_{T,j,b,\ell} > 10$ GeV and $\Delta R_{jj,bb,j\ell} > 0.1$. The $t\bar{t}$ +jets background is generated as one hard jet with $p_{T,j} > 100$ GeV in the hard matrix element. We do not consider merged samples since we found that the influence of $t\bar{t} + 2j$ to our analysis is negligible. After generation cuts, we start with a signal cross section of 4.2 pb. Associated $t\bar{t}Z$ production yields 1.2 pb. The continuum $t\bar{t}b\bar{b}$ background counts 121 pb and is at this stage dominated by $t\bar{t} + jets$ with 2750 pb. We demand the transverse momentum of the isolated leptons to exceed 10 GeV. For isolation we require a transverse momentum ratio (isolation variable) $I < 0.1$ within $\Delta R = 0.3$. Jets are obtained using the Cambridge/Aachen (C/A) jet algorithm [30] implemented in FASTJET3 [52] on energy flow objects constructed within DELPHES3. To tag a jet as b -jet, we require a parton-level b -quark within $\Delta R = 0.3$ and assume a tagging efficiency of 50 % and a misidentification rate of 1% for all jets within $|y_j| < 2.5$ and $p_{T,j} > 30$ GeV. For the

identification of Higgs and top candidates, we use a modified BDRS Higgs tagger [33, 36] and the HEPTOPTAGGER2 [38], respectively.

The analysis starts by asking for an isolated lepton with $|y_\ell| < 2.5$ and $p_{T,\ell} > 15$ GeV. Further, we require at least two fat C/A jets with $R = 1.8$ and $p_{T,j} > 200$ GeV. One of them has to yield a HEPTOPTAGGER2 top tag within $|y_j^{(t)}| < 4$. Since both the signal and the backgrounds contain a hadronic top quark, changing the top tagging parameters only leads to an overall factor. Since in this analysis the initial size of the fat jets is chosen to fit the expected transverse momenta of the top quarks, we do not cut on the difference between the found and calculated optimal radius. To be save with respect to the QCD multi-jet background, we set a mild cut on the filtered N -subjettiness ratio $\tau_3/\tau_2 < 0.8$. This cut can be tightened at the cost of signal efficiency if desired.

Once we identified the hadronic top quark, we remove the associated hadronic activity from the event and recluster to fat C/A jets with $R = 1.2$, $|y_j^{(H)}| < 2.5$, and $p_{T,j} > 200$ GeV. These fat jets are the starting point for a modified BDRS Higgs tagger. The fat jets are decomposed in hard substructures with $m_{\text{sub}} > 40$ GeV using a mass drop threshold of 0.9. All possible pairs of hard substructures are ordered by their modified Jade distance

$$J = p_{T,1}p_{T,2}(\Delta R_{12})^4. \quad (\text{IV.3})$$

While the usual Jade distance uses the squared distance ΔR^2 and thus is similar to the

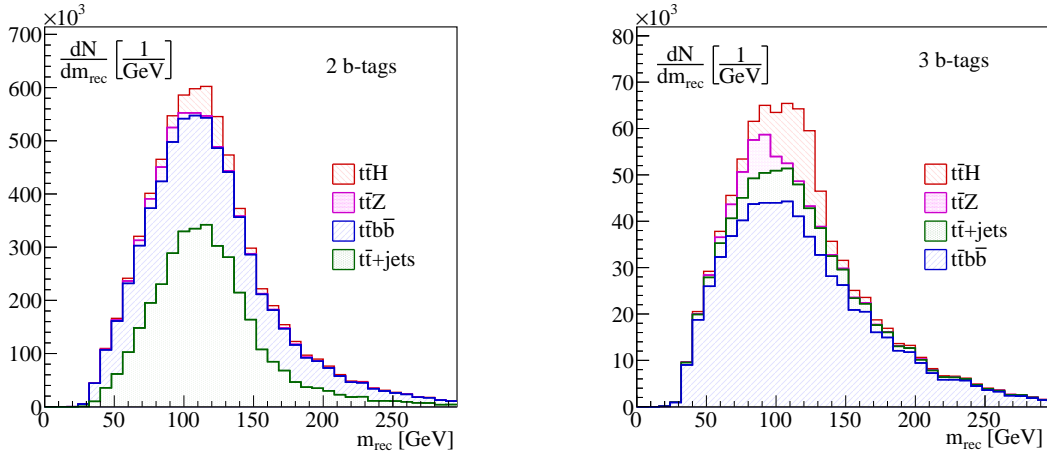


Figure IV.5: Reconstructed m_{bb} for the leading- J substructures in the fat Higgs jet. We require two b -tags inside the fat Higgs jet (left) and an additional continuum b -tag (right). The event numbers are scaled to $\mathcal{L} = 20 \text{ ab}^{-1}$. Taken from Ref. [66].

$m_{bb} \in [100, 150]$ GeV	2 b -tags	3 b -tags	ratio
$t\bar{t}H$	$2.4 \cdot 10^5$	$6.4 \cdot 10^4$	1/3.8
$t\bar{t}b\bar{b}$	$1.2 \cdot 10^6$	$2.4 \cdot 10^5$	1/5.0
$t\bar{t}+$ jets	$1.9 \cdot 10^6$	$3.8 \cdot 10^4$	1/50
$t\bar{t}Z$	$2.3 \cdot 10^4$	$4.9 \cdot 10^3$	1/4.7

 Table IV.7: Event numbers assuming an integrated luminosity of 20 ab^{-1} .

squared mass, this measure emphasizes the angular separation of the substructures. We filter the leading pair following the original BDRS approach using the $N_{\text{filt}} = 3$ hardest structures, which allows for a hard gluon from final-state radiation. For consistency we require the reconstructed transverse momentum to exceed 200 GeV. Finally, we require a double b -tag within the Higgs candidate.

The reconstructed m_{bb} distribution in the left panel of Fig. IV.5 illustrates that at this stage the $t\bar{t}+$ jets and $t\bar{t}b\bar{b}$ backgrounds are of similar size. Moreover, the analysis sculpts the distributions to peak around $m_{bb} \sim 100$ GeV. An additional continuum b -tag simplifies the background composition and reduces the strong background sculpting. For this purpose, we cluster the hadronic event that is not used for the reconstruction of the hadronic top and the Higgs boson to $R = 0.6$ C/A jets and ask for a b -tag within $|y_b| < 2.5$ and a separation of $\Delta R_{bj} > 0.4$ from all other jets including the top and Higgs decay jets. The resulting m_{bb} distribution in the right panel of Fig. IV.5 is now dominated by the $t\bar{t}b\bar{b}$ background while the $t\bar{t}+$ jets background is reduced to the level of the Higgs signal. The corresponding event numbers for an integrated luminosity of 20 ab^{-1} are provided in Tab. IV.7.

C. Updated BDRS tagger

In this section, we apply the main improvements of the HEPTOPTAGGER2 to the BDRS Higgs tagger. While for top tagging the N -subjettiness ratio τ_3/τ_2 is a powerful observable, for the decay $H \rightarrow b\bar{b}$ we have to identify a two prong structure and therefore the relevant quantity is τ_2/τ_1 . The correlation between the reconstructed masses and the ratio τ_2/τ_1 obtained from the filtered fat jets in Fig. IV.6 suggests that a cut $\tau_2/\tau_1 < 0.4$ not only reduces the backgrounds but also leads to narrower peaks in the m_{bb} distributions.

The second improvement of the HEPTOPTAGGER2 is optimalR mode. Reducing the radius of the fat jet stepwise to its optimal value decreases contaminations from underlying event and pile-up and minimizes the combinatorics in the m_{bb} reconstruction. In the same way as for the HEPTOPTAGGER2, we reduce the size of the fat jet in steps of 0.1 until the reconstructed mass drops below $m_j < 0.8 m_{j,\text{orig}}$ compared to the Higgs candidate obtained at $R = 1.2$. Additionally, we can estimate the expected optimal radius from fits to Monte Carlo simulations to

$$\Delta R_{bb}^{(\text{calc})} = \frac{250 \text{ GeV}}{p_{T,\text{filt}}}. \quad (\text{IV.4})$$

This relation is consistent with the expectation $\Delta R \sim 2m/p_T$ for a two-prong decay and supports the original choice of $R = 1.2$ for $p_T > 200 \text{ GeV}$. Due to this choice, we find that the difference between the calculated and algorithmically obtained value does not significantly improve the analysis. However, the mass difference of the Higgs and the Z boson gives rise to a shifted peak in the $\Delta R_{bb} - \Delta R_{bb}^{(\text{calc})}$ distribution for $t\bar{t}Z$ which could be used if one wants to reduce the Z peak in the m_{bb} distribution. The left panel of Fig. IV.8

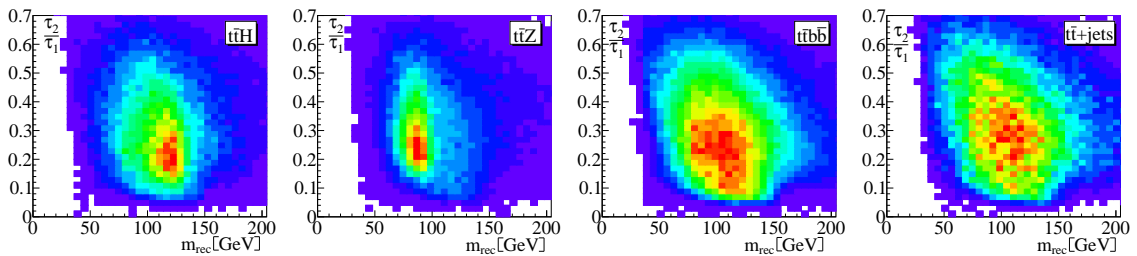


Figure IV.6: Correlation between the reconstructed mass m_{rec} and the N -subjettiness ratio τ_2/τ_1 of the filtered Higgs candidate fat jet for the signal and background samples. The event numbers are scaled to $\mathcal{L} = 20 \text{ ab}^{-1}$. Taken from Ref. [66].

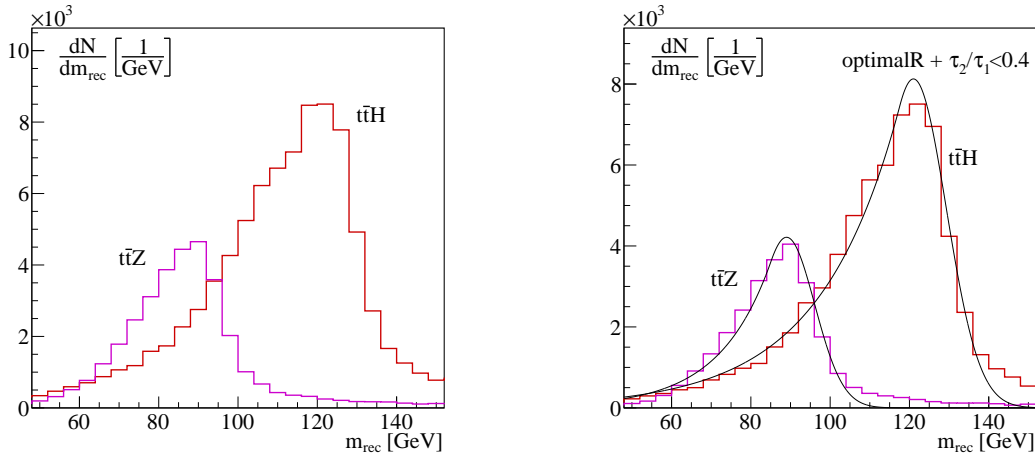


Figure IV.7: Reconstructed m_{bb} of the Higgs and Z candidates in $t\bar{t}H$ and $t\bar{t}Z$ production with the default BDRS tagger (left) and after using optimalR and the N -subjettiness cut $\tau_2/\tau_1 < 0.4$ (right). In the right panel we include the fitted Crystal Ball functions. The event numbers are scaled to $\mathcal{L} = 20 \text{ ab}^{-1}$. Taken from Ref. [66].

provides the final result including a triple b -tag, the N -subjettiness variable τ_2/τ_1 , and a modified fat jet radius for the Higgs candidate.

For $m_{bb} \in [160, 300] \text{ GeV}$, we obtain a smooth sideband that can be used to subtract the QCD continuum. The soft regime $m_{bb} \in [0, 60] \text{ GeV}$ might be useful as well but needs to be checked by a full experimental analysis. Using the range $m_{bb} \in [104, 136] \text{ GeV}$ as signal region, we receive a signal-to-background ratio around $S/B \approx 1/3$ and a Gaussian significance $S/\sqrt{B} = 120$ for an integrated luminosity of $\mathcal{L} = 20 \text{ ab}^{-1}$. The error for the extraction of the nominally $N_S = 44700$ has two contributions. If we assume a perfect knowledge of the background, we can determine N_S from the total number of events $N_S + N_B$ in the signal region. The actual error on the background comes from the side band. It contains $N_{\text{side}} = 135000$ events and its relative uncertainty of $1/\sqrt{N_{\text{side}}}$ yields a statistical uncertainty ΔN_B . Altogether, this leads to

$$\begin{aligned} \Delta N_S &= \left[\left(\sqrt{N_S + N_B} \right)^2 + \left(\Delta N_B \right)^2 \right]^{1/2} \\ &= \left[\left(\sqrt{N_S + N_B} \right)^2 + \left(\frac{N_B}{\sqrt{N_{\text{side}}}} \right)^2 \right]^{1/2} = 0.013 N_S, \end{aligned} \quad (\text{IV.5})$$

which translates into a relative uncertainty for the Yukawa coupling of around 1%.

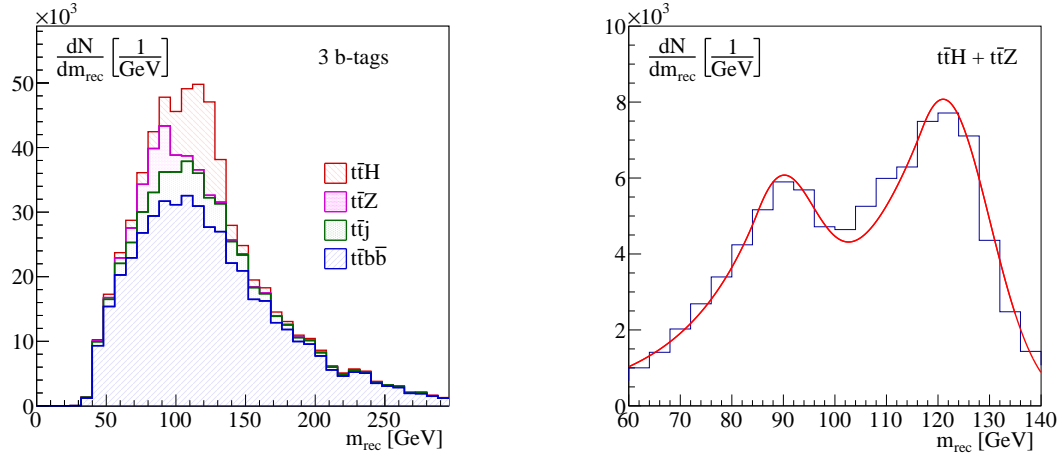


Figure IV.8: Left: Reconstructed m_{bb} for the leading- J substructures in the fat Higgs jet. We require two b -tags inside the fat Higgs jet and a continuum b -tag. Unlike in Fig. IV.5 we apply an N -subjettiness cut and use an optimalR version of the BDRS tagger. Right: Double-peak fit assuming perfect continuum background subtraction. The event numbers are scaled to $\mathcal{L} = 20 \text{ ab}^{-1}$. Taken from Ref. [66].

In the right panel of Fig. IV.8, we simultaneously fit the Higgs and Z boson peaks assuming a perfect background subtraction. Such an analysis with known masses serves as a check of the jet substructure techniques and allows to reduce systematic uncertainties as explained in the Sec. IV A. Based on separate Monte Carlo simulations for the Higgs and Z peaks, we can fix the shape of both distributions. We fit to each distribution a Crystal Ball function [105] which combines a Gaussian core with a power-law tail towards low masses. The fits are depicted in the right panel of Fig. IV.7. For the fits, we fix the peak positions accounting for losses due to reconstruction. The linear combination of the two fits allows us to model the background subtracted m_{bb} distribution. For the combined fit we keep all shape parameters fixed and allow only for separate scaling factors. This double Crystal-Ball function yields the relative size of the two peak areas $N_H/N_Z = 2.80 \pm 0.03$. Therefore, the combined fit enables us to probe the top Yukawa coupling with a statistical precision of $\sim 0.5\%$. As discussed in Sec. IV A, the obtained precision can be matched by the theoretical systematics, provided the $t\bar{t}Z$ production is not affected by new physics beyond the percent level.

Finally, the measurement might be limited by experimental systematics arising from b -tagging. However, the b -tagging efficiencies can be studied *e.g.* in the process $pp \rightarrow ZZ \rightarrow \ell^+ \ell^- b\bar{b}$. Based on the ZZ production cross section $\sigma(ZZ) = 200 \text{ pb}$ at 100 TeV, we expect

$1.5 \cdot 10^7$ events within 20 ab^{-1} . Even after including efficiencies, cuts and a stiff cut on the transverse momentum of the lepton pair to boost the recoiling $b\bar{b}$ system, per-mille-level statistical precision should be reachable.

D. Conclusions

The top Yukawa coupling is a key parameter for the understanding of the Higgs potential. At the LHC the expected statistics and theoretical uncertainties will limit its measurement to around $\Delta y_t/y_t \approx 10\%$ [12, 13]. In this chapter, we proposed an analysis of $t\bar{t}H$ production in the $H \rightarrow b\bar{b}$ decay channel at a future 100 TeV hadron collider. Focusing on the semileptonic decay of the top-quark pair and a boosted phase-space regime, our analysis is based on a lepton and two fat jets corresponding to the hadronic top and Higgs decays. The obtained m_{bb} distribution yields a smooth sideband that can be used to subtract the dominant backgrounds. A second peak from $t\bar{t}Z$ allows for a translation to a measurement of the top Yukawa coupling. Considering the ratio $\sigma(t\bar{t}H)/\sigma(t\bar{t}Z)$ systematic uncertainties can be significantly reduced.

Finally, we find that a measurement of the top Yukawa coupling should be possible to percent-level precision at $\sqrt{s} = 100$ TeV with an integrated luminosity of 20 ab^{-1} , provided sufficient precision for the $H \rightarrow b\bar{b}$ is available. Therefore, a 100 TeV collider would yield an order of magnitude better precision than the LHC.

V. A POSSIBLE EXPLANATION FOR THE HIERARCHY OF YUKAWA COUPLINGS

The content of this chapter is work done in collaboration with M. Bauer (U Heidelberg) and T. Plehn (U Heidelberg), and is published as Ref. [106]. Most of the credit for the calculation of quark and lepton flavor constraints is entitled to Martin Bauer.

One of the outstanding mysteries of the Standard Model is the large hierarchy of masses. While in the Standard Model all fermion masses are generated by electroweak symmetry breaking through the Higgs mechanism, the observed masses range from mass of the electron $m_e = 511$ keV to the top-quark mass $m_t = 173.2$ GeV as illustrated in Fig. V.1. This observation has led to various models beyond the Standard Model including Abelian flavor symmetries [107, 108], loop-suppressed couplings to the Higgs [109], partial compositeness [110], or wave-function localization [111]. Each of these models introduces flavor-violating couplings and additional heavy degrees of freedom. The resonances, however, are not unique. Already today's experimental results push the scale of the connected new physics beyond the energy scale reachable at the LHC. Consequently, these theories are studied in terms of an effective field theory, integrating out the occurrence of new particles.

In this section, we propose a minimal Froggatt-Nielsen setup [107] allowing for couplings directly related to the generation of the flavor hierarchies and study search strategies for the dynamic agent of flavor symmetry breaking [113], the flavon, at a future hadron collider. In this setup a future discovery can directly probe the underlying mechanism of flavor symmetry breaking. In general, the dimensionless Yukawa couplings do not favor any underlying mass scale. A low flavor breaking scale appears if we link the flavor breaking

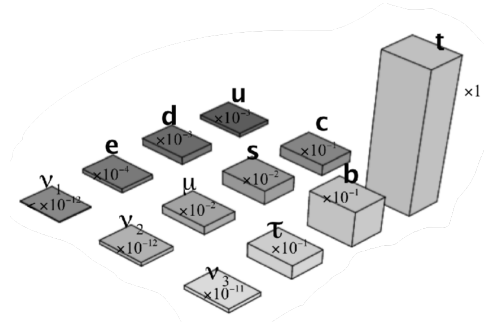


Figure V.1: Masses in the Standard Model. Adapted from Ref. [112].

and the electroweak scale [114] or if dark matter interactions are mediated by flavon exchange [115]. We deliberately remain agnostic about the ultraviolet completion and discuss the accessible parameter space independent of model building aspects.

After introducing the model, we review the most stringent flavor bounds and projections of current and future experiments testing the quark and lepton sectors in Sec. V B. Recently, LHC, Belle, and BaBar have made significant progress in testing quark flavor physics. Future searches will only slightly increase their sensitivity. On the other hand, tests of the lepton flavor sector [116] are expected to make significant progress based on experiments like MEG II, Mu3e, DeeMe, COMET, and Mu2e. These experiments aim for improvements in precision by several orders of magnitude.

In Sec. V D, we estimate the discovery reach of the LHC and a future 100 TeV hadron collider [117]. We find that the latter will for the first time allow us to probe a sizable part of the flavon parameter space, *i.e.* giving us access to the actual dynamic degrees of freedom in the flavor sector rather than constraining its symmetry structure based on effective field theory. This way, flavon searches add a qualitatively new aspect to the case of a future proton-proton collider.

A. Flavon model

The probably simplest setup for a Froggatt-Nielsen flavon model is to charge the Higgs boson and all Standard Model fermions, except for the top quark, under a global $U(1)$ or a discrete subgroup. This setup forbids all standard Yukawa terms in the Lagrange density with exception of the top-quark mass term. Introducing a new complex scalar field S with flavor charge $a_S = 1$, we can write down the modified Yukawa sector assuming the existence of right-handed neutrinos:

$$\begin{aligned}
 -\mathcal{L}_{\text{Yukawa}} = & y_{ij}^d \left(\frac{S}{\Lambda}\right)^{n_{ij}^d} \bar{Q}_i \Phi d_{R_j} + y_{ij}^u \left(\frac{S}{\Lambda}\right)^{n_{ij}^u} \bar{Q}_i \tilde{\Phi} u_{R_j} \\
 & + y_{ij}^\ell \left(\frac{S}{\Lambda}\right)^{n_{ij}^\ell} \bar{L}_i \Phi \ell_{R_j} + y_{ij}^\nu \left(\frac{S}{\Lambda}\right)^{n_{ij}^\nu} \bar{L}_i \tilde{\Phi} \nu_{R_j} + \text{h.c.}
 \end{aligned} \tag{V.1}$$

The flavor indices $i, j \in [1, 3]$ link the fundamental Yukawa couplings with the corresponding number of insertions of the scalar field S . To compensate for the additional mass dimension, each insertion has to be suppressed by the UV scale Λ . We assume that the field S acquires a vacuum expectation value (VEV) f through the potential

$$-\mathcal{L}_{\text{potential}} = -\mu_S^2 S^* S + \lambda_S (S^* S)^2 - b(S^2 + S^{*2}) + \lambda_{\Phi S} (S^* S) (\Phi^\dagger \Phi) + V(\Phi), \tag{V.2}$$

where $V(\Phi)$ denotes the usual Higgs potential. Here, we switch off the portal interaction by setting $\lambda_{\Phi S} = 0$. Otherwise the mixing with the Higgs [118] and changed Higgs couplings would become an alternative strategy for effects of this model. Assuming $\lambda_{\Phi S} = 0$, the excitation around the VEV lead to the physical flavon field

$$S(x) = \frac{f + s(x) + i a(x)}{\sqrt{2}}. \tag{V.3}$$

As shown in App. B, this yields the masses for the scalar and pseudoscalar components

$$m_s = \sqrt{2\mu_S^2 + 4b} = \sqrt{2\lambda_S} f \quad \text{and} \quad m_a = 2\sqrt{b}, \tag{V.4}$$

where the mass of the pseudoscalar “pion” of flavor breaking remains a free parameter. Provided it stays below the flavor scale, we can assume

$$m_a < m_s \approx f < \Lambda . \quad (\text{V.5})$$

Consequently, the first resonance one should find in searches for this mechanism is the pseudoscalar flavon a . In this model the entire flavor structure is dictated by

$$\epsilon = \frac{f}{\sqrt{2}\Lambda} = \frac{1}{\Lambda} \sqrt{\frac{\mu_S^2 + 2b}{2\lambda_S}} \quad \text{with} \quad v < f < \Lambda . \quad (\text{V.6})$$

We fix the numerical value of ϵ to the Cabibbo angle

$$\epsilon = (V_{\text{CKM}})_{12} \approx 0.23 . \quad (\text{V.7})$$

Starting from anarchic fundamental Yukawa matrices of order one

$$|y^{u,d,\ell}| \approx \begin{pmatrix} 1 & 1 & 1 \\ 1 & 1 & 1 \\ 1 & 1 & 1 \end{pmatrix} , \quad (\text{V.8})$$

the effective Yukawa couplings are obtained from

$$-\mathcal{L}_{\text{Yukawa}} = Y_{ij}^d \bar{Q}_i \Phi d_{R_j} + Y_{ij}^u \bar{Q}_i \tilde{\Phi} u_{R_j} + Y_{ij}^\ell \bar{L}_i \Phi \ell_{R_j} + Y_{ij}^\nu \bar{L}_i \tilde{\Phi} \nu_{R_j} + \text{h.c.} \quad (\text{V.9})$$

as $Y_{ij} = y_{ij} \epsilon^{n_{ij}}$. Thus, the hierarchy of Yukawa couplings is determined by the number of insertions of the field S .

Flavon couplings

The exponents n_{ij} of the ratio S/Λ are dictated by the flavor charges we assign to the Higgs doublet and the Standard Model fermions

$$\begin{aligned} n_{ij}^d &= a_{Q_i} - a_{d_j} - a_\Phi \\ n_{ij}^u &= a_{Q_i} - a_{u_j} + a_\Phi , \end{aligned} \quad (\text{V.10})$$

where $a_{u_j} = a_{u,c,t}$ and $a_{d_j} = a_{d,s,b}$ denote the flavor charges of the three generations of quark singlets, a_{Q_i} are the flavor charges of the three generations of quark doublets, and a_Φ is the flavor charge of the Higgs doublet. To obtain the correct quark masses in our benchmark scenario we set $a_S = 1$, $a_\Phi = 0$, and

$$\begin{pmatrix} a_{Q_1} & a_{Q_2} & a_{Q_3} \\ a_u & a_c & a_t \\ a_d & a_s & a_b \end{pmatrix} = \begin{pmatrix} 3 & 2 & 0 \\ -5 & -2 & 0 \\ -4 & -3 & -3 \end{pmatrix}. \quad (\text{V.11})$$

Using the benchmark point defined in App. B, we obtain for the masses

$$m_t \approx \frac{v}{\sqrt{2}} \quad \frac{m_b}{m_t} \approx \epsilon^3 \quad \frac{m_c}{m_t} \approx \epsilon^4 \quad \frac{m_s}{m_t} \approx \epsilon^5 \quad \frac{m_d}{m_t} \approx \epsilon^7 \quad \frac{m_u}{m_t} \approx \epsilon^8, \quad (\text{V.12})$$

and for the quark mixing the Cabibbo-Kobayashi-Maskawa (CKM) matrix

$$V_{\text{CKM}} \approx \begin{pmatrix} 1 & \epsilon & \epsilon^3 \\ \epsilon & 1 & \epsilon^2 \\ \epsilon^3 & \epsilon^2 & 1 \end{pmatrix}. \quad (\text{V.13})$$

In the mass basis the flavon couplings are linked to the Yukawa couplings. Neglecting $\mathcal{O}(1)$ factors in the off-diagonal entries, they read

$$g_{af_i L f_j R}^u \equiv g_{aij}^u = \frac{1}{f} \begin{pmatrix} 8m_u & \epsilon m_c & \epsilon^3 m_t \\ \epsilon^3 m_c & 4m_c & \epsilon^2 m_t \\ \epsilon^5 m_t & \epsilon^2 m_t & 0 \end{pmatrix} \quad g_{aij}^d = \frac{1}{f} \begin{pmatrix} 7m_d & \epsilon m_s & \epsilon^3 m_b \\ \epsilon m_s & 5m_s & \epsilon^2 m_b \\ \epsilon m_b & \epsilon^2 m_b & 3m_b \end{pmatrix}. \quad (\text{V.14})$$

In the same way, the exponents for the lepton sector are given by

$$\begin{aligned} n_{ij}^\ell &= a_{L_i} - a_{\ell_j} - a_\Phi \\ n_{ij}^\nu &= a_{L_i} - a_{\nu_j} + a_\Phi. \end{aligned} \quad (\text{V.15})$$

To reproduce the lepton masses and mixing structures, we use

$$\begin{pmatrix} a_{L_1} & a_{L_2} & a_{L_3} \\ a_{\nu_e} & a_{\nu_\mu} & a_{\nu_\tau} \\ a_e & a_\mu & a_\tau \end{pmatrix} = \begin{pmatrix} 1 & 0 & 0 \\ -24 & -21 & -20 \\ -8 & -5 & -3 \end{pmatrix}. \quad (\text{V.16})$$

The charges for the neutrino can be smaller if one introduces a Majorana mass term. A possible way is to set the flavor charges of the right-handed neutrinos to 1/2 allowing for

$$\mathcal{L}_{\text{Majorana}} = M_\nu \nu_R \nu_R, \quad (\text{V.17})$$

with $M_\nu = f$. The flavor charges in Eq. (V.16) result in lepton mass ratios

$$\frac{m_\tau}{m_t} \approx \epsilon^3 \quad \frac{m_\mu}{m_t} \approx \epsilon^5 \quad \frac{m_e}{m_t} \approx \epsilon^9 \quad \frac{m_{\nu_1}}{m_t} \approx \epsilon^{25} \quad \frac{m_{\nu_2}}{m_t} \approx \epsilon^{21} \quad \frac{m_{\nu_3}}{m_t} \approx \epsilon^{20}, \quad (\text{V.18})$$

and the lepton mixing matrix

$$U_{\text{PMNS}} \approx \begin{pmatrix} 1 & \epsilon & \epsilon \\ \epsilon & 1 & 1 \\ \epsilon & 1 & 1 \end{pmatrix}. \quad (\text{V.19})$$

As in the quark sector, we can give the couplings up to order-one factors in the off-diagonal entries

$$g_{af_i L f_j R}^\ell \equiv g_{aij}^\ell = \frac{1}{f} \begin{pmatrix} 9m_e & \epsilon m_\mu & \epsilon m_\tau \\ \epsilon^3 m_\mu^3 & 5m_\mu & \epsilon^2 m_\tau \\ \epsilon^5 m_\tau & \epsilon^2 m_\tau & 3m_\tau \end{pmatrix}. \quad (\text{V.20})$$

For simplicity, we define

$$g_{ij} \equiv g_{sf_i L f_j R} = i g_{af_i L f_j R} \quad (\text{V.21})$$

to leading order and for all fermions except for $i = j = t$. A detailed derivation of the masses and couplings is provided in App. B.

Flavon and top decays

For the couplings in Eqs. (V.14) and (V.14) we can calculate the partial decay widths of the flavon. An important difference to the Higgs boson in the decay to fermion pairs at LO is the possibility of decays that are not flavor diagonal. The LO partial width for the decay of the pseudoscalar flavon to fermions is given by

$$\frac{\Gamma(a \rightarrow f_i \bar{f}_j)}{m_a} = \frac{N_c}{16\pi} \left[\frac{(m_a^2 - (m_i + m_j)^2)(m_a^2 - (m_i - m_j)^2)}{m_a^4} \right]^{1/2} \left[(|g_{ij}|^2 + |g_{ji}|^2) \left(1 - \frac{m_i^2 + m_j^2}{m_a^2} \right) - 2(g_{ij}g_{ji} + g_{ij}^*g_{ji}^*) \frac{m_i m_j}{m_a^2} \right], \quad (\text{V.22})$$

where for leptons the color factor N_C is set to one. At one-loop level, we can compute the decay to photons and gluons in analogy to the Higgs, taking care of the pseudoscalar nature of the flavon. Figure V.2 provides the obtained branching ratios depending on the flavon mass m_a for our choice of $\epsilon = 0.23$. At low flavon masses the decay modes are similar to the ones of the Higgs boson: the decay mode $a \rightarrow b\bar{b}$ dominates the decay into τ -leptons due the larger coupling and the color factor. Once the flavon mass exceeds the top-quark mass, the off-diagonal decays including top quarks open up and the flavor-violating decay $a \rightarrow tc$ takes over. While in our analyses we do not assume charm tagging, it might be a possible experimental improvement. The decay $a \rightarrow t\bar{t}$ does not occur at tree level.

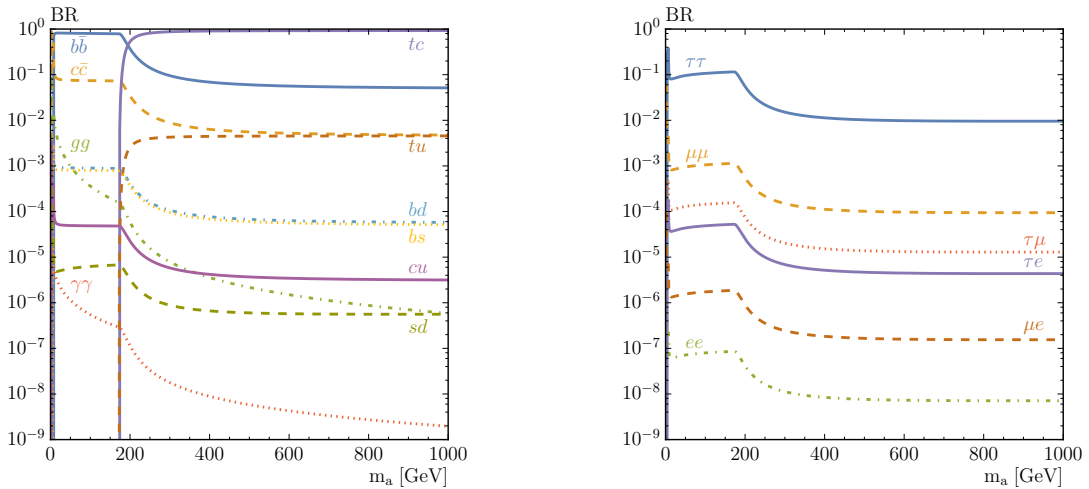


Figure V.2: Flavon branching ratios for decays to quarks (left) and leptons (right). Taken from Ref. [106].

The large off-diagonal couplings $g_{tc} \sim g_{ct}$ do not only play a role in the decay of heavy flavons. If the flavon is lighter than the top quark, they induce flavor-changing top-quark decays. In the limit $m_c \ll m_a < m_t$ the corresponding decay width reads

$$\frac{\Gamma(t \rightarrow ca)}{m_t} = \frac{1}{32\pi} (|g_{ct}|^2 + |g_{tc}|^2) \left(1 - \frac{m_a^2}{m_t^2}\right)^2. \quad (\text{V.23})$$

This channel with a Higgs boson instead of a flavon in the final state has been subject of analyses at the LHC and will be discussed later in the context of collider constraints in Sec. VD.

B. Quark flavor constraints

To date, the most stringent constraints on the proposed flavon model arise from quark flavor physics. Especially, loop-induced meson mixing and rare decays shrink the allowed parameter space spanned by the flavon mass m_a , the VEV f and the quartic coupling λ_S . In this section, we provide constraints in the f - m_a plane for fixed quartic flavon coupling $\lambda_S = 2$.

Neutral meson mixing

One effect of the flavon coupling structure are flavor-changing neutral currents (FCNC) which influence meson-antimeson mixing with $\Delta F = 2$. Such mixings can be described by the effective Hamiltonian

$$\begin{aligned} \mathcal{H}_{\text{NP}}^{\Delta F=2} = & C_1^{ij} (\bar{q}_L^i \gamma_\mu q_L^j)^2 + \tilde{C}_1^{ij} (\bar{q}_R^i \gamma_\mu q_R^j)^2 + C_2^{ij} (\bar{q}_R^i q_L^j)^2 + \tilde{C}_2^{ij} (\bar{q}_L^i q_R^j)^2 \\ & + C_4^{ij} (\bar{q}_R^i q_L^j) (\bar{q}_L^i q_R^j) + C_5^{ij} (\bar{q}_L^i \gamma_\mu q_L^j) (\bar{q}_R^i \gamma^\mu q_R^j) + \text{h.c.} \end{aligned} \quad (\text{V.24})$$

The Wilson coefficients generated by exchange of the new scalar s and the pseudoscalar flavon a are [119, 120]

$$\begin{aligned} C_2^{ij} &= -(g_{ji}^*)^2 \left(\frac{1}{m_s^2} - \frac{1}{m_a^2} \right) \\ \tilde{C}_2^{ij} &= -g_{ij}^2 \left(\frac{1}{m_s^2} - \frac{1}{m_a^2} \right) \\ C_4^{ij} &= -\frac{g_{ij}g_{ji}}{2} \left(\frac{1}{m_s^2} + \frac{1}{m_a^2} \right). \end{aligned} \quad (\text{V.25})$$

While the fields s and a enter the coefficient C_4 in the same way, they differ in C_2 and \tilde{C}_2 by a relative minus sign. However, given that their masses are generated by independent scales, a cancelation of these two contributions would be accidental. For the different meson systems there can be sizable enhancements from renormalization group (RG) running and matrix elements. We implement RG running according to Refs. [121, 122] with the matrix elements given in Ref. [123] and match the scalar and pseudoscalar flavon contributions at $\mu = m_s$ and $\mu = m_a$, respectively. Projections for future experimental and lattice improvements are provided in Ref. [124].

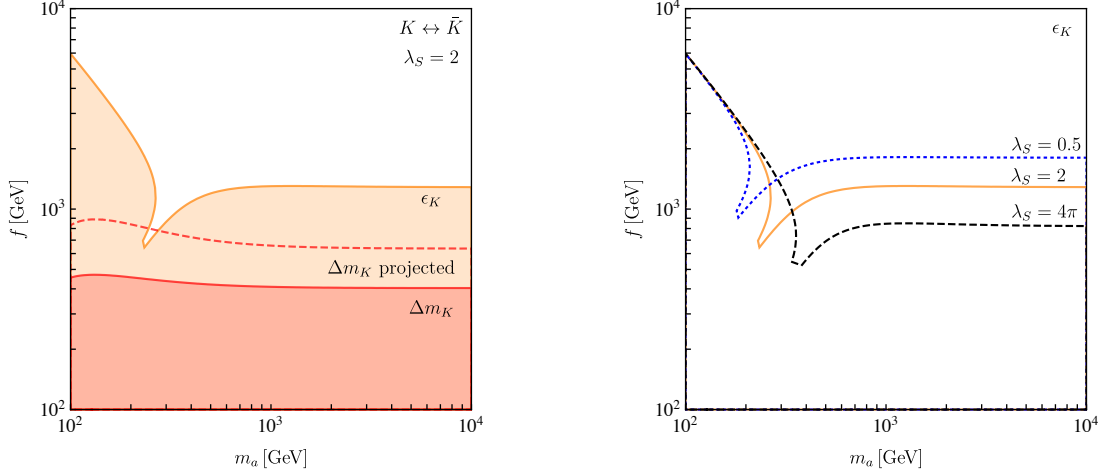


Figure V.3: Left: regions in the $m_a - f$ plane excluded by flavon contributions to ϵ_K (orange) and Δm_K (red) for our benchmark point and $\lambda_S = 2$. The dashed red contour corresponds to the excluded region based on projected improvements in Δm_K . Right: constraint from ϵ_K for $\lambda_S = 0.5$ (dotted blue), $\lambda_S = 2$ (orange) and $\lambda_S = 4\pi$ (dashed black). Taken from Ref. [106].

The UFIT collaboration [121] provides limits for $K - \bar{K}$ mixing

$$\begin{aligned}
 C_{\epsilon_K} &= \frac{\text{Im}\langle K^0 | \mathcal{H}^{\Delta F=2} | \bar{K}^0 \rangle}{\text{Im}\langle K^0 | \mathcal{H}_{\text{SM}}^{\Delta F=2} | \bar{K}^0 \rangle} = 1.05^{+0.36}_{-0.28} \\
 C_{\Delta m_K} &= \frac{\text{Re}\langle K^0 | \mathcal{H}^{\Delta F=2} | \bar{K}^0 \rangle}{\text{Re}\langle K^0 | \mathcal{H}_{\text{SM}}^{\Delta F=2} | \bar{K}^0 \rangle} = 0.93^{+1.14}_{-0.42},
 \end{aligned} \tag{V.26}$$

where $\mathcal{H}_{\text{SM}}^{\Delta F=2}$ denotes the Standard Model contribution and $\mathcal{H}^{\Delta F=2}$ includes additionally the new contributions. The obtained exclusion limits for the flavon model are shown in the left panel of Fig. V.3. The dip in the bound set by C_{ϵ_K} originates from accidental cancellation in C_2^{sd} and \tilde{C}_2^{sd} . The bound from $C_{\Delta m_K}$ exhibits a similar feature below $m_a = 100$ GeV. The dashed contour illustrates projected improvements in Δm_K under the optimistic assumptions of Ref. [124]. The dependence of the bound obtained from C_{ϵ_K} on the quartic coupling λ_S is depicted in the right panel of Fig.V.3.

In the B sector, one can parametrize the mixing of $B_d \leftrightarrow \bar{B}_d$ and $B_s \leftrightarrow \bar{B}_s$ by

$$C_{B_q} e^{2i\varphi_{B_q}} = \frac{\langle B_q | \mathcal{H}^{\Delta F=2} | \bar{B}_q \rangle}{\langle B_q | \mathcal{H}_{\text{SM}}^{\Delta F=2} | \bar{B}_q \rangle}, \tag{V.27}$$

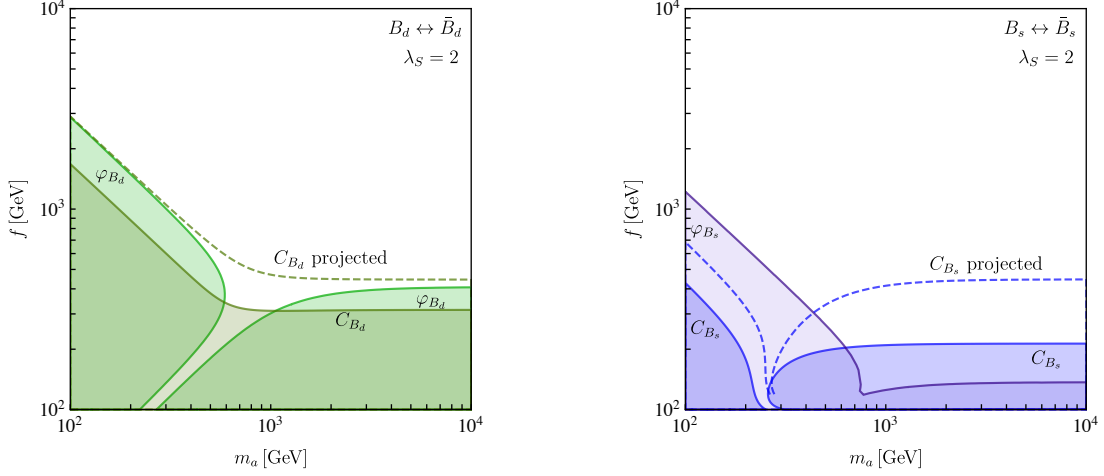


Figure V.4: Left: regions in the $m_a - f$ plane excluded by flavon contributions to C_{B_d} (light green) and φ_{B_d} (green) for our benchmark point and $\lambda_S = 2$. Right: constraints from flavon contributions to C_{B_s} (blue) and φ_{B_s} (light purple). The dashed contours correspond to the excluded regions based on projected improvements in C_{B_d} and C_{B_s} . Taken from Ref. [106].

with the 95% CL limits [121]

$$\begin{aligned}
 C_{B_d} &= 1.07^{+0.36}_{-0.31} & \varphi_{B_d} &= -2.0^{+6.4}_{-6.0} \\
 C_{B_s} &= 1.052^{+0.178}_{-0.152} & \varphi_{B_s} &= 0.72^{+3.98}_{-2.28}.
 \end{aligned}
 \tag{V.28}$$

Figure V.4 illustrates the corresponding limits. Again, the optimistic projections for C_{B_q} follow Ref. [124].

Finally, we provide limits from $D-\bar{D}$ mixing in Fig. V.5. Here, we only demand that the new contributions do not exceed the 2σ constraint [125]

$$|M_{12}^D| = |\langle D | \mathcal{H}^{\Delta F=2} | \bar{D} \rangle| < 7.7 \text{ ps}^{-1}
 \tag{V.29}$$

because of the large hadronic uncertainties in this process. While the relatively large couplings $g_{tc,ct}$ could lead to sizable one-loop box-contributions, the relative suppression $\sim \epsilon^2 m_t^2 / (4\pi^2 f^2)$ renders them irrelevant for the considered parameter space.

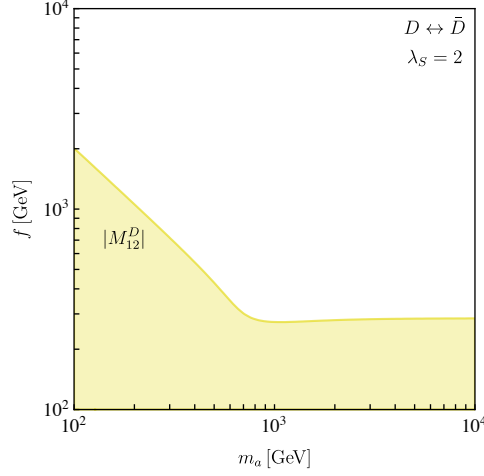


Figure V.5: Regions in the $m_a - f$ plane excluded by flavon contributions to $|M_{12}^D|$ (shaded yellow) for our benchmark point and $\lambda_S = 2$. Taken from Ref. [106].

Leptonic meson decays

Besides mixing, neutral mesons constrain the parameters of the flavon through their decays into charged leptons. Such decays can be described by the effective Hamiltonian

$$\begin{aligned} \mathcal{H}_{\text{eff}} = & -\frac{G_F^2 m_W^2}{\pi^2} \left(C_S^{ij} (\bar{q}_i P_L q_j) \bar{\ell} \ell + \tilde{C}_S^{ij} (\bar{q}_i P_R q_j) \bar{\ell} \ell \right. \\ & \left. + C_P^{ij} (\bar{q}_i P_L q_j) \bar{\ell} \gamma_5 \ell + \tilde{C}_P^{ij} (\bar{q}_i P_R q_j) \bar{\ell} \gamma_5 \ell \right) + \text{h.c.} . \end{aligned} \quad (\text{V.30})$$

The branching ratio for a neutral meson M follows as

$$\begin{aligned} \text{BR}(M \rightarrow \ell^+ \ell^-) = & \frac{G_F^4 m_W^4}{8\pi^5} \beta m_M f_M^2 m_\ell^2 \tau_M \\ & \times \left[\left| \frac{m_M^2 (C_P^{ij} - \tilde{C}_P^{ij})}{2m_\ell (m_i + m_j)} - C_A^{\text{SM}} \right|^2 + \left| \frac{m_M^2 (C_S^{ij} - \tilde{C}_S^{ij})}{2m_\ell (m_i + m_j)} \right|^2 \beta^2 \right] , \end{aligned} \quad (\text{V.31})$$

where $\beta = \sqrt{1 - 4m_\ell^2/m_M^2}$. Again the only relevant contributions are given at tree level. The corresponding Wilson coefficients read

$$\begin{aligned} C_S^{ij} &= \frac{\pi^2}{2G_F^2 m_W^2} \frac{2g_{\ell\ell} g_{ji}}{m_s^2} & \tilde{C}_S^{ij} &= \frac{\pi^2}{2G_F^2 m_W^2} \frac{2g_{\ell\ell} g_{ij}}{m_s^2} \\ C_P^{ij} &= \frac{\pi^2}{2G_F^2 m_W^2} \frac{2g_{\ell\ell} g_{ji}}{m_a^2} & \tilde{C}_P^{ij} &= \frac{\pi^2}{2G_F^2 m_W^2} \frac{2g_{\ell\ell} g_{ij}}{m_a^2}. \end{aligned} \quad (\text{V.32})$$

In the Standard Model, the only non-zero contribution C_A^{SM} originates from the axial coupling structure at one-loop level. For B_s it is to very good approximation given by

$$C_A^{\text{SM}} = -V_{tb}^* V_{ts} Y \left(\frac{m_t^2}{m_W^2} \right), \quad (\text{V.33})$$

with

$$Y(x) = \eta_{\text{QCD}} \frac{x}{8} \left[\frac{4-x}{1-x} + \frac{3x}{(1-x)^2} \log x \right], \quad (\text{V.34})$$

where $\eta_{\text{QCD}} = 1.0113$ parametrizes higher-order corrections [126]. To account for the sizable width difference in the B_S system, the obtained theoretical prediction has to be upscaled by a factor $(1 - y_s)^{-1}$, where $y_s = 0.088 \pm 0.014$ [127]. The most stringent experimental limit is provided by CMS and LHCb [128]

$$\text{BR}(B_s \rightarrow \mu^+ \mu^-) = 2.8_{-0.6}^{+0.7} \cdot 10^{-9}. \quad (\text{V.35})$$

The resulting limits in the f - m plane are presented in the left panel of Fig. V.6. For the B_d system the correction due to the width difference is negligible and the Standard Model value can be calculated using Eq. (V.33) with the appropriate index replacements. The recent limit on $B_d \rightarrow \mu^+ \mu^-$ is set by a combination of the results from CMS and LHCb [128–130]

$$\text{BR}(B_d \rightarrow \mu^+ \mu^-) = (3.9 \pm 1.6) \cdot 10^{-10}. \quad (\text{V.36})$$

We require the flavon model to be consistent with this value within 2σ , namely $\text{BR}(B_d \rightarrow \mu^+ \mu^-) = [1.4, 7.4] \cdot 10^{-10}$. The corresponding region is illustrated in the right panel of Fig. V.6. The measured value deviates from the Standard Model prediction $\text{BR}(B_d \rightarrow \mu^+ \mu^-)^{\text{SM}} = (1.06 \pm 0.09) \times 10^{10}$ on the 2σ level. Unfortunately, a explanation of the

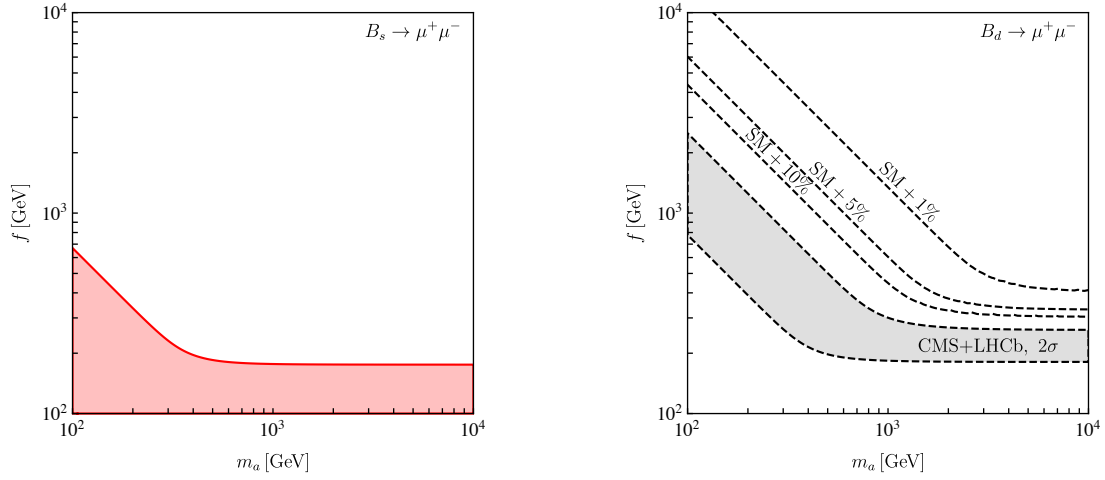


Figure V.6: Left: regions in the $m_a - f$ plane excluded by flavon contributions to the decay $B_s \rightarrow \mu^+ \mu^-$. Right: parameter space where the branching ratio for $B_d \rightarrow \mu^+ \mu^-$ stays within the 2σ confidence interval (shaded gray), as well as contours of 1%, 5% and 10% enhancement with respect to the SM prediction. Taken from Ref. [106].

measured value is not in accordance with the constraints from neutral meson mixing. In addition, we include contours in the right panel of Fig. V.6 corresponding to 1, 5 and 10 % deviation from the Standard Model. Beside these constraints from bottom mesons, we can also determine limits from $D \rightarrow \mu^+ \mu^-$ decays which are considerably weaker. The decay $K_L \rightarrow \mu^+ \mu^-$ excludes similar regions of the parameter space as $B_s \rightarrow \mu^+ \mu^-$.

C. Future lepton flavor measurements

Today, the leading constraints on flavor physics on the proposed flavon model originate from quark flavor physics. However, upcoming lepton flavor experiments will provide stringent limits as well. In this section, we compare recent and projected limits based on our benchmark point.

Decay $\mu \rightarrow e\gamma$

Radiative flavor-violating lepton decays $\ell \rightarrow \ell'\gamma$ are mediated by dipole operators

$$\mathcal{L}_{\text{eff}} = m_{\ell'} C_T^L \bar{\ell} \sigma^{\rho\lambda} P_L \ell' F_{\rho\lambda} + m_{\ell'} C_T^R \bar{\ell} \sigma^{\rho\lambda} P_R \ell' F_{\rho\lambda}. \quad (\text{V.37})$$

This effective Lagrange density leads to branching ratios

$$\text{BR}(\ell' \rightarrow \ell\gamma) = \frac{m_{\ell'}^5}{4\pi\Gamma_{\ell'}} (|C_T^L|^2 + |C_T^R|^2). \quad (\text{V.38})$$

The relevant one-loop diagram for the flavon contributions in the left panels of Fig. V.7 give rise to the Wilson coefficients

$$C_T^L = (C_T^R)^* = \frac{g}{32\pi^2} \sum_{k=e,\mu,\tau} \left\{ \frac{1}{6} \left(g_{\ell k}^* g_{\ell' k} + \frac{m_{\ell}}{m_{\ell'}} g_{k\ell}^* g_{k\ell'} \right) \left(\frac{1}{m_s^2} - \frac{1}{m_a^2} \right) - g_{\ell k} g_{k\ell'} \frac{m_k}{m_{\ell'}} \left[\frac{1}{m_s^2} \left(\frac{3}{2} + \log \frac{m_{\ell'}^2}{m_s^2} \right) - \frac{1}{m_a^2} \left(\frac{3}{2} + \log \frac{m_{\ell'}^2}{m_a^2} \right) \right] \right\}. \quad (\text{V.39})$$

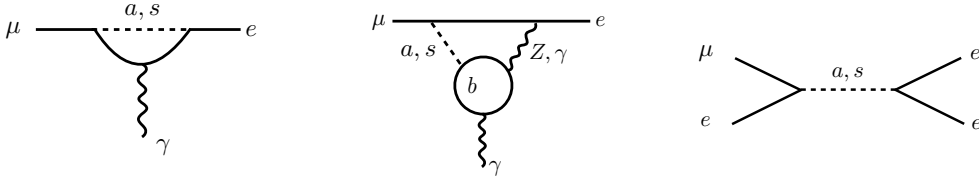


Figure V.7: Feynman diagrams showing flavon contributions to $\mu \rightarrow e\gamma$ at one-loop level and two-loop level, as well as flavon contributions to $\mu \rightarrow 3e$. Taken from Ref. [106].

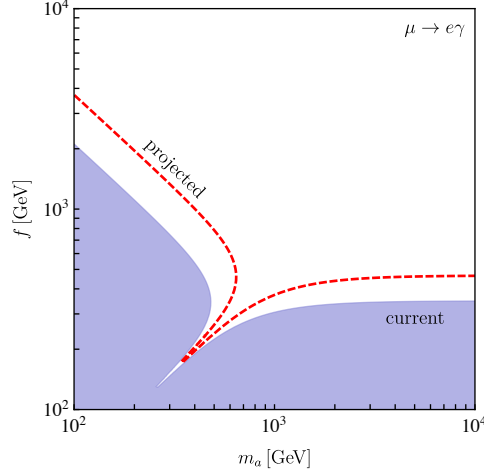


Figure V.8: Regions in the $m_a - f$ plane excluded by flavon contributions to $\mu \rightarrow e\gamma$. The corresponding bounds from $\tau \rightarrow \mu\gamma$ and $\tau \rightarrow e\gamma$ are not visible for the plotted parameter range. Taken from Ref. [106].

Especially, the second term proportional to $m_k/m_{\ell'}$ leads to sizable contributions for a τ -lepton running in the loop. Current bounds are provided by MEG [131] and Belle [132]

$$\text{BR}(\mu \rightarrow e\gamma) < 5.7 \cdot 10^{-13} \quad \text{and} \quad \text{BR}(\tau \rightarrow \mu\gamma) < 4.5 \cdot 10^{-8} . \quad (\text{V.40})$$

The implications of the limits on $\mu \rightarrow e\gamma$ as well as the projected sensitivity of the MEG-II experiment [133],

$$\text{BR}(\mu \rightarrow e\gamma) = 6 \cdot 10^{-14} , \quad (\text{V.41})$$

are illustrated in Fig. V.8.

Conversion $\mu \rightarrow e$

Further constraints arise from $N\mu \rightarrow Ne$ conversion in nuclei. Such interactions can be described on parton level by an effective Lagrange density which contains additional terms to the dipole operators of Eq.(V.37)

$$\begin{aligned} \mathcal{L}_{\text{eff}} = & m_\mu C_T^L \bar{e} \sigma^{\rho\nu} \mu F_{\rho\nu} + C_{qq}^{VL} \bar{e} \gamma^\nu P_L \mu \bar{q} \gamma_\nu q \\ & + m_\mu m_q C_{qq}^{SL} \bar{e} P_R \mu \bar{q} q + m_\mu \alpha_s C_{gg}^L \bar{e} P_R \mu G_{\rho\nu} G^{\rho\nu} + (R \leftrightarrow L) , \end{aligned} \quad (\text{V.42})$$

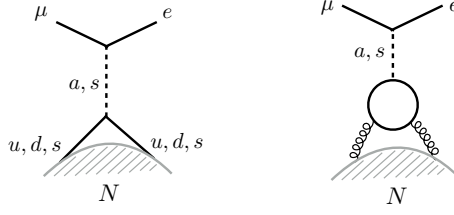


Figure V.9: Diagrams showing flavon contributions to $\mu \rightarrow e$ conversion in nuclei at tree level and one-loop level. Taken from Ref. [106].

Due to the relevant diagrams depicted in Fig. V.9, the flavon model generates the Wilson coefficients

$$\begin{aligned} C_{qq}^{SL} &= \left(\frac{1}{m_s^2} + \frac{1}{m_a^2} \right) g_{\mu e}^* \text{Re}(g_{qq}), \\ C_{qq}^{SR} &= \left(\frac{1}{m_s^2} - \frac{1}{m_a^2} \right) g_{e\mu} \text{Re}(g_{qq}), \end{aligned} \quad (\text{V.43})$$

in addition to C_T^L and C_T^R . Contributions to $C_{gg}^{L,R}$ can be absorbed in $\tilde{C}_{P,N}^{SL}$. Like for flavor-violating Higgs couplings [134], contributions from vector operators are smaller than all scalar coefficients and can be neglected. While in such a model Barr-Zee-type two-loop diagrams generate the dominant contributions, in our flavon model they are irrelevant due to the absence of a flavor-diagonal coupling to a top quark. On nucleon level the relevant Wilson coefficients are

$$\tilde{C}_p^{VL} = \sum_{q=u,d} C_{qq}^{VL} f_{V_q}^p \quad \text{and} \quad \tilde{C}_p^{SL} = \sum_{q=u,d,s} C_{qq}^{SL} f_q^p - \sum_{Q=c,b,t} C_{QQ}^{SL} f_{\text{heavy}}^p, \quad (\text{V.44})$$

in which $f_{V_q}^p, f_q^p$, and $f_{\text{heavy}}^p = 2/27(1 - f_u^p - f_d^p - f_s^p)$ account for the quark content of the proton [135]. While the vector coefficients count the valence quarks in the proton, i.e. $f_{V_u}^p = 2f_{V_d}^p = 2$, the scalar couplings measure the contribution of quark condensates to the mass of the nucleon $\langle p | m_q \bar{q}q | p \rangle = f_q^p m_p$. Analogous expressions are valid for the neutron. We use the numerical values provided in Refs.[136, 137], based on the lattice

average from Ref. [138]:

$$\begin{aligned}
 f_u^p &= 0.0191 & f_u^n &= 0.0171, \\
 f_d^p &= 0.0363 & f_d^n &= 0.0404, \\
 f_s^p &= f_s^n & &= 0.043.
 \end{aligned}
 \tag{V.45}$$

Finally, the expression for the conversion rate reads

$$\Gamma_{N\mu \rightarrow Ne} = \frac{m_\mu^5}{4} \left| C_T^L D + 4 \left[m_\mu m_p \tilde{C}_p^{SL} + \tilde{C}_p^{VL} V^p + (p \rightarrow n) \right] \right|^2,
 \tag{V.46}$$

with p and n denoting the proton and neutron, respectively. The coefficients $D, S^{p,n}$ and $V^{p,n}$ are dimensionless functions of the overlap integrals of the initial-state muon and the final-state electron wave-functions with the target nucleus. We use the numerical values provided in Ref. [139]:

Target	D	S^p	S^n	V^p	V^n	$\Gamma_{\text{capt}}[10^{-6}\text{s}]$
Au	0.189	0.0614	0.0918	0.0974	0.146	13.06
Al	0.0362	0.0155	0.0167	0.0161	0.0173	0.705
Si	0.0419	0.0179	0.0179	0.0187	0.0187	0.871

with Γ_{capt} denoting the muon capture rate.

Currently, the leading constraints are set by the SINDRUM II experiment [140] for a gold target

$$\text{BR}(\mu \rightarrow e)^{\text{Au}} < 7 \cdot 10^{-13}.
 \tag{V.47}$$

The future DeeMe [141] and COMET [142] experiments as well as Mu2e [143] aim to improve this bound using a silicon or an aluminum target. Their projections are

$$\text{BR}(\mu \rightarrow e)^{\text{Si}} < 2 \cdot 10^{-14} \quad \text{and} \quad \text{BR}(\mu \rightarrow e)^{\text{Al}} < 6 \cdot 10^{-17}.
 \tag{V.48}$$

The current bounds in Fig. V.10 cannot compete with the available quark flavor constraint. However, the situation will change once future lepton flavor experiments become operational.

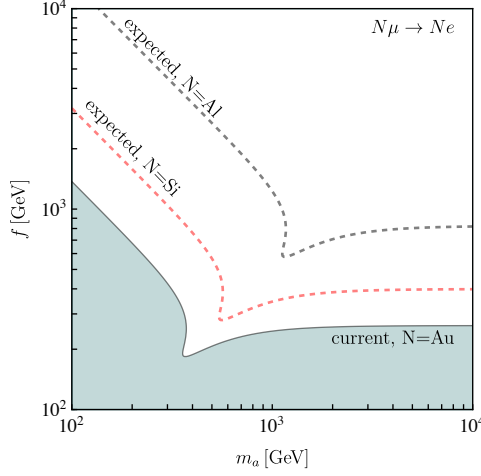


Figure V.10: Regions in the $m_a - f$ plane excluded by flavon contributions to the conversion $N\mu \rightarrow Ne$. Taken from Ref. [106].

Decays $\mu \rightarrow 3e$ and $\tau \rightarrow 3\mu$

Very closely related to the decays $\ell' \rightarrow \ell\gamma$ are decays $\ell' \rightarrow 3\ell$. The corresponding decay width can be approximated by

$$\Gamma(\ell' \rightarrow 3\ell) = \frac{\alpha m_\ell^5}{12\pi^2} \left| \log \frac{m_{\ell'}^2}{m_\ell^2} - \frac{11}{4} \right| (|C_T^L|^2 + |C_T^R|^2). \quad (\text{V.49})$$

In principle, there are additional contributions from tree-level diagrams like the one shown in the right panel of Fig. V.7. However, those are chirally suppressed while the one-loop contributions are logarithmically enhanced such that the latter dipole contributions dominate the tree-level ones by four orders of magnitude in the case of $\mu \rightarrow 3e$. For $\tau \rightarrow 3\mu$ the tree-level contributions become important. Contributions from Z -penguin diagrams are suppressed with respect to the photon contributions and are neglected. Currently, the most constraining bounds on these decays are [144, 145]

$$\begin{aligned} \text{BR}(\tau \rightarrow 3\mu) &< 2.1 \cdot 10^{-8}, \\ \text{BR}(\tau \rightarrow 3e) &< 2.7 \cdot 10^{-8}, \\ \text{BR}(\mu \rightarrow 3e) &< 1.0 \cdot 10^{-12}. \end{aligned} \quad (\text{V.50})$$

The limits from τ -decays do not constrain our model in the parameter space region of interest. Upcoming results from Mu3e will improve the current bounds on $\mu \rightarrow 3e$ by three

orders in magnitude in phase I and a further order in phase II [146]. The corresponding constraints on the parameter space are shown in Fig. V.11.

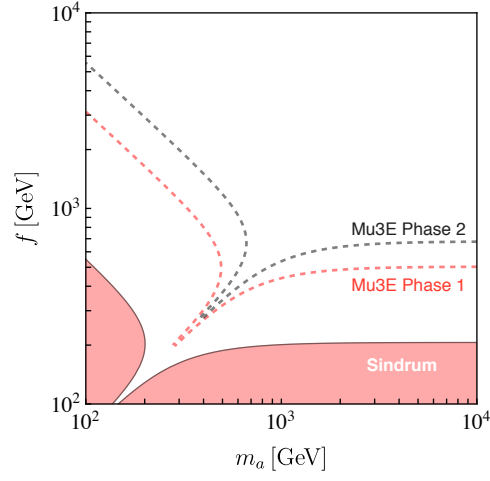


Figure V.11: Regions in the m_a - f plane excluded by flavon contributions $\mu \rightarrow 3e$. Taken from Ref. [106].

D. Future hadron collider measurements

Before discussing the reach of a future 100 TeV hadron collider, we briefly consider limits from direct LHC searches. For light flavons the main search channels are anomalous top-quark decays described by Eq. (V.23). The current measurement of the total top width was obtained at the Tevatron: $1.10 \text{ GeV} < \Gamma_{\text{tot}} < 4.05 \text{ GeV}$ [19, 147]. The large error bar makes this global observable not helpful for flavon searches. Instead, we can search for specific anomalous decays in analogy to the current limit of $\text{BR}(t \rightarrow Hq) \lesssim 0.5\%$ [19]. The current and expected reach for such decays at the LHC and a 100 TeV hadron collider is

$$\begin{aligned} \text{BR}_{8 \text{ TeV}}(t \rightarrow Hc) &< 5.6 \cdot 10^{-3}, \\ \text{BR}_{14 \text{ TeV}, 3 \text{ ab}^{-1}}(t \rightarrow Hc) &< 4.5 \cdot 10^{-5}, \\ \text{BR}_{100 \text{ TeV}, 30 \text{ ab}^{-1}}(t \rightarrow Hc) &< 2.2 \cdot 10^{-6}, \end{aligned} \tag{V.51}$$

based on the channel $H \rightarrow b\bar{b}$. Our estimate for the 100 TeV collider is obtained by scaling the number of expected top quarks by the leading-order ratio of $\sigma(pp \rightarrow t\bar{t})$ at 14 TeV and 100 TeV calculated with MADGRAPH [102]. Assuming a Gaussian scaling, the limit can be estimated by

$$(\sigma\text{BR})_{\text{limit}}^{\text{new}} = \sqrt{\frac{\mathcal{L}_{\text{old}}}{\mathcal{L}_{\text{new}}}} \sqrt{\frac{\sigma_{\text{BG}}^{\text{new}}}{\sigma_{\text{BG}}^{\text{old}}}} (\sigma\text{BR})_{\text{limit}}^{\text{old}} \tag{V.52}$$

For the top-quark counting experiment this implies an improvement by a factor $6.4\sqrt{\mathcal{L}_{100 \text{ TeV}}/\mathcal{L}_{14 \text{ TeV}}}$. The limits on $t \rightarrow Hc$ can be translated into limits on $\text{BR}(t \rightarrow ac \rightarrow b\bar{b}c)$, using $\text{BR}(a \rightarrow b\bar{b}) > 80\%$ from Fig. V.2. Figure V.12 provides calculated branching ratios and corresponding limits as function of the flavon mass and the excluded parameter space. A future 100 TeV hadron collider with 30 ab^{-1} data should be able to constrain the relevant couplings to

$$\sqrt{|g_{tc}|^2 + |g_{ct}|^2} \lesssim \frac{1 \cdot 10^{-3}}{1 - \frac{m_a}{m_t}}. \tag{V.53}$$

For flavon masses above the top-quark mass, we expect constraints from direct flavon

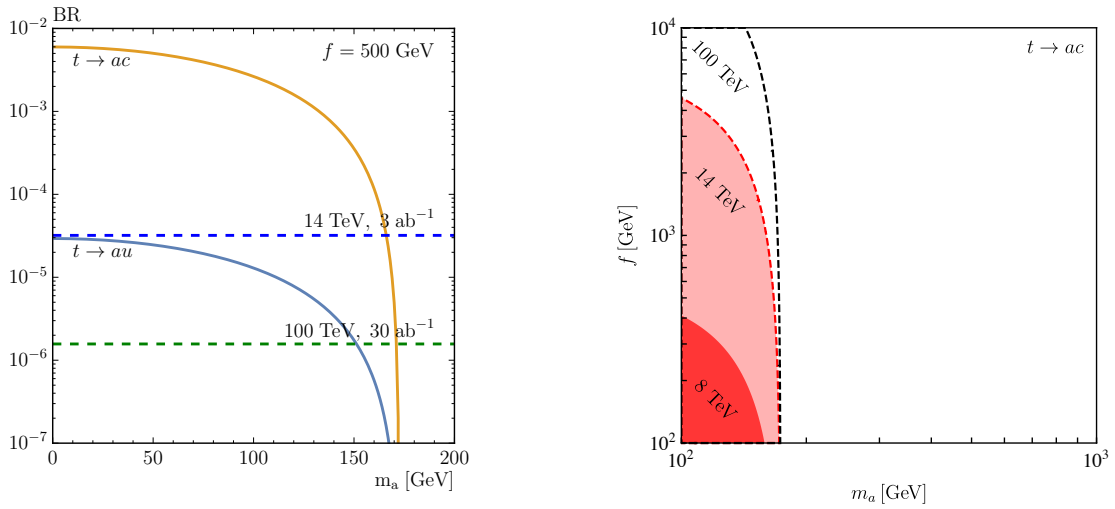


Figure V.12: Left: top branching ratios into a flavon and a jet as a function of the flavon mass, assuming a fixed VEV of $f = 500$ GeV. Right: regions in the $m_a - f$ plane excluded by these days at the LHC and at a 100 TeV collider. Taken from Ref. [106].

decays. Single flavon production is dominated by

$$gg, b\bar{b} \rightarrow a, \quad (\text{V.54})$$

where we assume that the collinear bottoms in the final state do not give us an experimental handle to distinguish the signal from backgrounds.

In absence of a flavor-diagonal coupling to top quarks the gluon-fusion production is subleading. In extended flavon models such couplings can be present, turning gluon fusion sizable even at LHC energies [113].

A second class of production mechanisms is the associated production

$$bg \rightarrow ab \quad \text{or} \quad ug, cg \rightarrow at, \quad (\text{V.55})$$

where we assume the additional b -quark to be hard and central and thus can be tagged. The first of these channels is driven by the flavor-diagonal coupling g_{bb} . The latter two indicate the existence of flavor off-diagonal couplings. Figure V.13 illustrates various production cross sections for the 14 TeV LHC and a 100 TeV proton-proton collider. For the 100 TeV collider, we expect millions of flavons with $m_a > 500$ GeV within 30 ab^{-1} of data. This enables us to study traditional resonance decays as well as specific top-associated

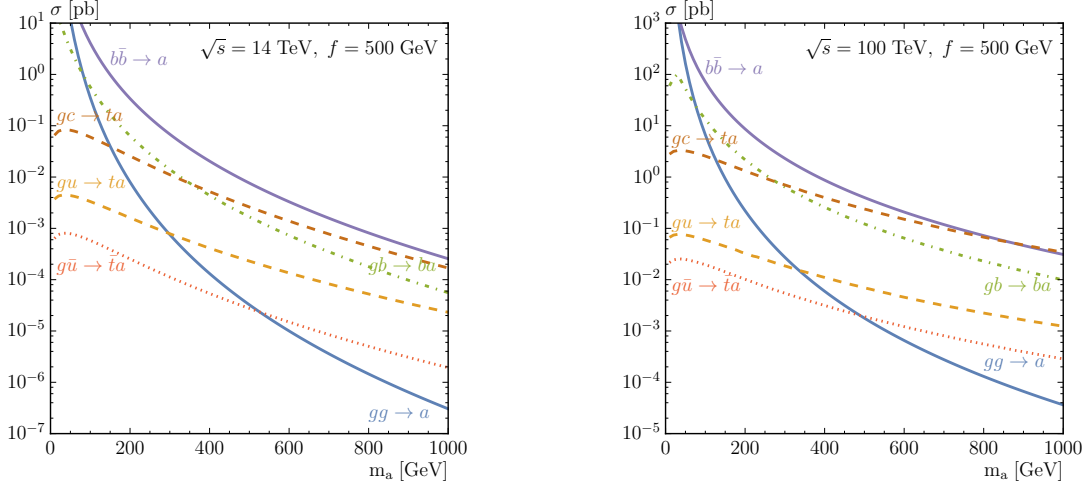


Figure V.13: Flavon production cross sections in the different channels for the 14 TeV LHC and a 100 TeV hadron collider using the MSTW2008 PDF set [148]. Couplings are evaluated at $\mu = m_a$ or $\mu = m_a + m_t$ with CRUNDEC [149]. Taken from Ref. [106].

production, where the flavons decay to $t\bar{q}$ and $\bar{t}q$ with $q = u, c$. In both cases the most important question is how the large backgrounds can be controlled.

Resonance searches

A direct way to search for the flavon as new dynamical degree of freedom are resonance searches like

$$pp \rightarrow a \rightarrow b\bar{b}/\tau^+\tau^- . \quad (\text{V.56})$$

As long as there are no flavor diagonal couplings to the top quark or a coupling to the W boson, the diphoton channel can be discarded. To estimate the discovery potential of a future proton-proton collider, we scale the current 8 TeV limits to 100 TeV assuming Eq. (V.52) with an approximate increase of the relevant background cross sections by a factor of 10 which seems a reasonable estimate except for top-quark pair production [150]. The used LHC limits at 8 TeV and the scaled limits for a 100 TeV collider are given together with the event rates for flavon masses of 500 GeV and 1 TeV in Tab. V.1. According to these numbers only the channel $pp \rightarrow a \rightarrow \tau\tau$ might become sensitive.

All these resonance searches are generic for new (pseudo)scalar particle. However, the

m_a [GeV]	ATLAS 8 TeV		CMS 8 TeV		100 TeV, 30 ab ⁻¹		benchmark	
	500	1000	500	1000	500	1000	500	1000
jet-jet [pb]		0.2				$2 \cdot 10^{-2}$	$2.4 \cdot 10^{-2}$	$1.6 \cdot 10^{-3}$
$\tau^+\tau^-$ [pb]	$4 \cdot 10^{-2}$	$5 \cdot 10^{-3}$	$4 \cdot 10^{-2}$	$9 \cdot 10^{-3}$	$3 \cdot 10^{-3}$	$4 \cdot 10^{-4}$	$4.1 \cdot 10^{-3}$	$3.0 \cdot 10^{-4}$
$\mu^+\mu^-$ [pb]	$5 \cdot 10^{-3}$	$1 \cdot 10^{-3}$	$2 \cdot 10^{-3}$	$8 \cdot 10^{-4}$	$2 \cdot 10^{-4}$	$6 \cdot 10^{-5}$	$4.0 \cdot 10^{-5}$	$2.9 \cdot 10^{-6}$
$\gamma\gamma$ [pb]	$6 \cdot 10^{-3}$	$1 \cdot 10^{-3}$	$2 \cdot 10^{-3}$		$2 \cdot 10^{-4}$	$8 \cdot 10^{-5}$	$2.3 \cdot 10^{-9}$	$6.1 \cdot 10^{-11}$

Table V.1: Current [152–156, 156–159] and expected limits for $\sigma \times \text{BR}$ in pb, assuming an increase in the background rate by a factor 10. For the flavon signal we assume $f = 500$ GeV.

flavor off-diagonal couplings introduce additional single top-quark signatures

$$pp \rightarrow a \rightarrow t\bar{c}/t\bar{u}. \quad (\text{V.57})$$

While the s -channel benefits from the large branching ratios for heavy flavons, the t -channel suffers from two flavon couplings. The corresponding SM background is single top-quark production with a next-to-leading order cross section of 73.5 pb at 100 TeV, requiring $|\eta_t| < 2.5$ [151]. A flavon mass of 500 GeV or 1 TeV results for $f = 500$ GeV in $\sigma \times \text{BR} = 0.37$ pb or $2.9 \cdot 10^{-2}$ pb, respectively. Thus this channel will not be sensitive even before considering the issue of charm tagging and the background from $t\bar{t}$ production.

Associated production

In addition to resonance searches, the large flavor changing couplings g_{tc}, g_{ct} allow for associated production of a flavon with a top quark. Focusing on the dominant branching ratios, this leads to the processes

$$pp \rightarrow ta \rightarrow t b\bar{b}/t \tau^+\tau^-. \quad (\text{V.58})$$

The special case of same-sign top-quark production from the decay $a \rightarrow tc$ is studied in the next section. The decay channel into bottom quarks has to face large combinatorial backgrounds and is overwhelmed by the $t\bar{t}$ background. Here, we focus on the decay to hadronic τ -leptons in combination with a hadronic top decay allowing for an approximate reconstruction of the final state. The heavy flavon decays to a boosted pair of τ -leptons which are significantly harder than the three top decay jets as can be inferred from the left panel of Fig. V.14. To extract such events, we require at least five jets and veto isolated

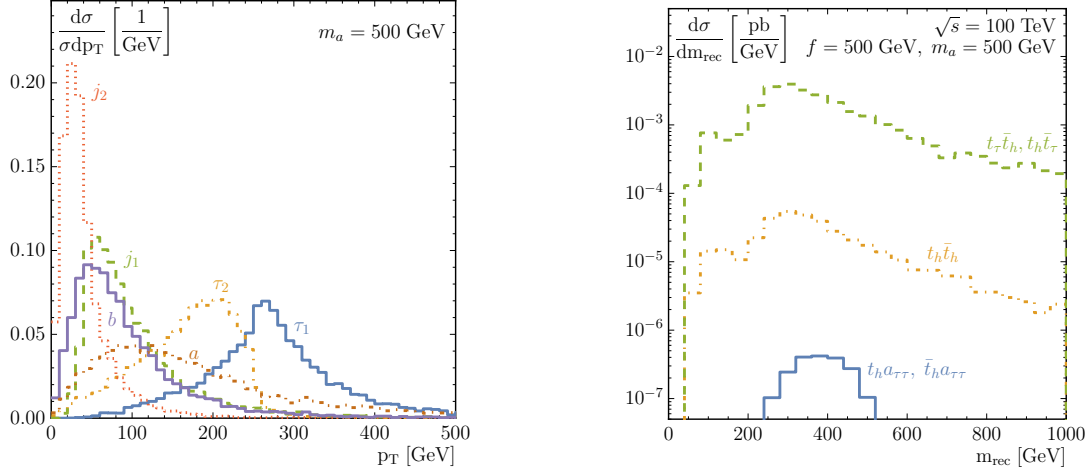


Figure V.14: Left: parton-level p_T distributions. Right: reconstructed mass distribution. Both figures are simulated for $m_a = 500$ GeV. The subscripts in the right panel indicate decays to τ s or hadrons. Taken from Ref. [106].

leptons

$$n_j \geq 5, \quad n_\ell = 0, \quad p_{T,j_1} > 150 \text{ GeV}, \quad m_{j_3 j_4 j_5} \in [140, 190] \text{ GeV}. \quad (\text{V.59})$$

For τ -tagging, we assume an optimistic efficiency of $\epsilon_\tau = 0.3$ and a misidentification rate of $\epsilon_j = 10^{-3}$ [160]. To reconstruct the flavon, we rely on the collinear approximation in terms of the momentum fractions $x_{1,2}$ of the decaying τ -leptons

$$m_{\tau\tau}^2 = \frac{2(p_{j_1} p_{j_2})}{x_1 x_2} \quad \text{with} \quad \frac{\vec{p}_{T,j_1}}{x_1} + \frac{\vec{p}_{T,j_2}}{x_2} = \vec{p}_{T,j_1} + \vec{p}_{T,j_2} + \vec{p}_T. \quad (\text{V.60})$$

This works since the τ -leptons are boosted and the $\tau\tau$ system recoils against the top quark and thus the two neutrinos are not back-to-back. We use FEYNRULES [161] to implement the flavon signal and generate a fully hadronic $t\bar{t}$ sample as well as a sample with one hadronic top quark and the other top quark decaying to a τ lepton with MADGRAPH5+PYTHIA8 +DELPHES3 [28, 51, 102], employing $R = 0.4$ anti- k_T jets from FASTJET3 [52]. For the jets we require $p_T > 20$ GeV and $|\eta| < 2.5$. The left panel of Fig. V.14 depicts the reconstructed flavon mass distribution for $m_a = 500$ GeV and $f = 500$ GeV. It is shifted towards lower masses caused by losses in the reconstruction. The comparison of the expected signal with the background eliminates any motivation to study this signature further.

Same-sign top-quark pairs

Arising from the large flavor-changing couplings g_{tc} and g_{ct} , the most interesting signature is same-sign top-quark production with one additional jet

$$pp \rightarrow t_\ell a \rightarrow t_\ell t_\ell \bar{c}, \quad (\text{V.61})$$

from a gc initial state, where we introduced the subscript ℓ to denote leptonic decays. The signature of such a process are two same-sign leptons, two b -jets, one additional jet and missing transverse momentum \cancel{p}_T . The corresponding SM background $pp \rightarrow bbW^+W^+j$ with a LO signal cross section of $5.7 \cdot 10^{-7}$ pb is negligible. However, $t_\ell \bar{t} Z j$ and $t_\ell \bar{t} W^+ j$ production can fake the signal if at least one top quark and the weak bosons decay leptonically. For event generation, we rely again on MADGRAPH5+PYTHIA8+DELPHES3. Before analysis cuts, the signal rate for a flavon mass $m_a = 500$ GeV is $5.4 \cdot 10^{-3}$ pb \times $(500 \text{ GeV}/f)^2$. It is dominated by the leading backgrounds with $\sigma_{t_\ell \bar{t} W^+ j} = 0.33$ pb and $\sigma_{t_\ell \bar{t} Z j} = 0.48$ pb.

The analysis starts with 2 isolated leptons fulfilling

$$R_{\text{iso}} = 0.2 \quad I_{\text{iso}} = 0.1 \quad p_{T,\ell} > 10 \text{ GeV} \quad |\eta_\ell| < 2.5. \quad (\text{V.62})$$

If there are more than 2 such leptons, we pick the hardest two. The $t_\ell \bar{t} Z j$ background can be reduced by a veto on events with third different-sign lepton and $|m_{\ell^+ \ell^-} - m_Z| < 15$ GeV. The hadronic activity is clustered into $R = 0.4$ anti- k_T jets with $p_T > 40$ GeV and $|\eta_j| < 2.5$ using FASTJET3. The hardest jet with $p_T > 100$ GeV constitutes the c -candidate. Among the other jets, we require two b -tags assuming a 50% b -tagging efficiency based on a parton-level b -quark within $\Delta R > 0.3$. The two neutrinos should give rise to $\cancel{p}_T > 50$ GeV. The missing transverse momentum has to be distributed to the two branches of the event, i.e. the top-quark and the flavon decay. A powerful observable to address such topologies is m_{T2} [162]. Before we can use it, we have to construct the two branches of the event. First, we assign the b -jets to the leptons by minimizing $\Delta R_{\ell_1 b_i} + \Delta R_{\ell_2 b_j}$. The c -jet is added to top candidate with smaller $\Delta y_{(t_b),j}$. We find that typically most signal events fulfill $m_t < m_{T2} < m_a$. This allows us to search for an excess in the m_{T2} distribution. The backgrounds provide smooth side-bands at high values of m_{T2} . The left panel of Fig. V.15 illustrates the distributions for a flavon mass of $m_a = 500$ GeV.

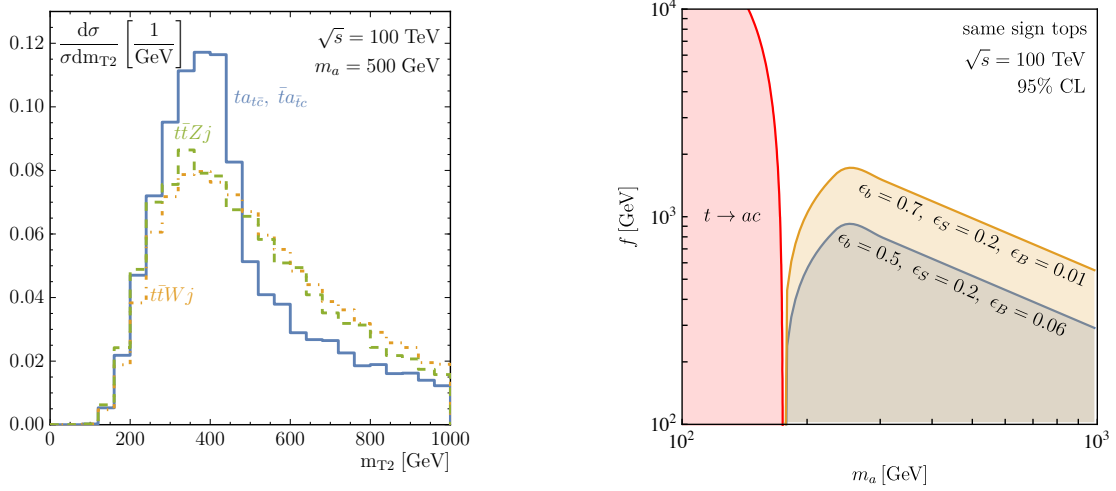


Figure V.15: Left: normalized m_{T2} distribution for a $m_a = 500$ GeV flavon and backgrounds. Right: exclusion limits from $\sigma(gc \rightarrow ta) \times \text{BR}(a \rightarrow t\bar{c})[\text{pb}]$ at $\sqrt{s} = 100$ TeV. The red area is excluded by $t \rightarrow ac$ decays. Taken from Ref. [106].

A last distinction between the signal and the backgrounds is the charge of the b -jets. For the flavon signal not only the two leptons should have the same sign, also the charges of the b -quarks [163] should be identical. Recent ATLAS studies [164] indicate that a $b\bar{b}$ distinction is possible with $\epsilon_S = 0.2$ and $\epsilon_B = 0.06$. For the future 100 TeV collider we assume two scenarios: as conservative estimate, we rely on these ATLAS efficiencies; for a more optimistic case, we assume an improved mistagging rate of $\epsilon_B = 0.01$ and an overall b -tagging efficiency of 70 %. The obtained exclusion limits at 95 % confidence level with the additional requirement $S/B > 0.1$ are illustrated in the right panel of Fig. V.15.

Flavon-pair production

In principle, the study of flavon pair production could be interesting as well. The dominant production channel $b\bar{b} \rightarrow aa$ with $g_{aabb} = 2m_b/f^2$ yields a signal cross section of $1.4 \cdot 10^{-3}$ pb at $\sqrt{s} = 100$ TeV and $m_a = f = 500$ GeV. The dominant decay channel to four b -quarks is overwhelmed by combinatorics and QCD backgrounds. The same-sign $tctc$ channel provides a more distinctive signature, however, it is dominated by $t\bar{t}W^+jj$ with a cross section of 4.6 pb for two jets with $p_{T,j} > 100$ GeV. Additionally, this channel would not allow for the reconstruction of a mass peak. Consequently, also flavon-pair production can be discarded as possible discovery channel.

E. Conclusions

In the past sections, we introduced a Froggatt-Nielsen-type flavon model to motivate the observed hierarchy of fermion masses. In the past, the experimental consequences of flavor models have successfully been described by an effective field theory. In the not-too-far future, flavor physics will be subject of both indirect and direct searches as it is already the case for weak gauge bosons, the top quark and the Higgs boson.

Studying current and future constraints, we illustrated that a large region of the flavon parameter space is accessible for alternative experimental approaches. Currently, the most constraining limits are based on the quark flavor sector. The expected improvements will strengthen current bounds by one order of magnitude. In the lepton flavor sector, we expect significant progress in the coming years. In addition to the indirect searches, a future 100 TeV proton collider will allow for systematic direct searches. Besides generic searches for new (pseudo)scalar resonances, same-sign top-quark searches with an additional jet provide a distinctive signature based on the large flavor-changing couplings to top quarks. To extend the reach of this channel, improvements in the distinction of bottom and antibottom quarks are extremely useful. The expected limits for indirect and direct searches in Fig. V.16 nicely fit together. The limits from quark and lepton flavor physics exhibit a dip feature due to destructive interference of the corresponding virtual scalar and

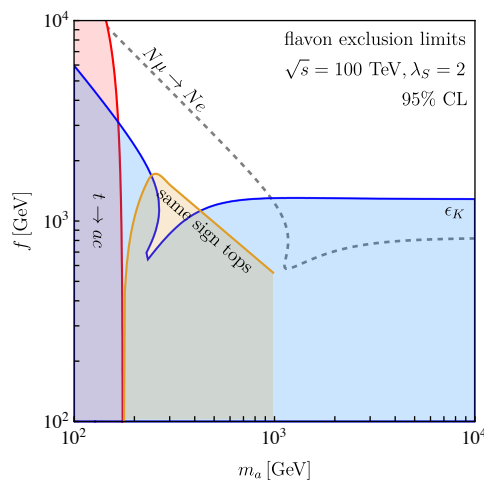


Figure V.16: Regions in the $m_a - f$ plane which can be probed by quark flavor physics (ϵ_K), by lepton flavor physics ($\mu \rightarrow e$ conversion), and by a 100 TeV hadron collider. For the latter we show the reach of anomalous top-quark decays and same-sign top-quark production.

pseudoscalar contributions. For small flavon masses, anomalous top-quark decays provide strong bounds. The weak parts of the indirect searches around $m_a \sim f$ can be cured by same-sign top-quark searches. In combination the shown limits provide independent coverage of the flavon parameter space in the lepton and quark sector. The latter ideally allows for a direct discovery of the flavon-specific couplings at a future 100 TeV proton-proton collider.

VI. SUMMARY

Top quarks are important in many different areas of particle physics. In this thesis, we focused on their coupling to the Higgs boson, the top Yukawa coupling y_t , and top quarks occurring in signatures of physics beyond the Standard Model. A measurement of y_t probes the mechanism of electroweak symmetry breaking and in absence of new physics plays a crucial role for the stability of the electroweak vacuum.

Essentially, this thesis consists of three parts, each containing its own more detailed conclusion section. In chapter III, we considered a classic resonance search for a heavy Z' boson decaying into hadronic top quarks which manifest themselves as fat jets. Starting from the old HEPTOPTAGGER in combination with a simple cut on the invariant mass of the reconstructed top-quark pair, we extended the analysis to a multivariate framework. This allowed for several steps of improvement. First, we included kinematical information of the reconstructed top quarks. The impact of final-state radiation could be reduced by considering information from the fat jets as well. The reconstruction of the Z' boson was limited by the efficiency to identify the two top quarks, *i.e.* the choice of a top-tagging working point. A multivariate setup allowed more flexibility by loosening tagging cuts but including the corresponding observables in the analysis. Further, we introduced a procedure to decrease the size of the used fat jets algorithmically (optimalR). Besides reducing the contamination from other hadronic activity, the difference between the found and expected size of the fat jet yields a new handle to distinguish top decay jets from background. Additionally, N -subjettiness provided information on the soft structures inside the fat jets. Finally, QJETS allowed us to consider alternative fat jet clustering histories which can be useful especially at high signal efficiencies. In combination, the background rejection at fixed signal efficiency could be improved by a factor 30 compared to the initial cut-and-count analysis. We illustrated that this makes the outlined analysis competitive with the leading proposals for such a resonance reconstruction. Finally, the improvements concerning standard top tagging have been incorporated in the HEPTOPTAGGER code yielding the new HEPTOPTAGGER2.

A measurement of the top Yukawa coupling in the process $t\bar{t}H$ was the focus of chapter IV. While its extraction at the LHC is limited by statistics to $\sim 10\%$, we illustrated

that at a future 100 TeV proton collider percent-level precision should be possible. We argued that theoretical uncertainties cancel in the ratio of $t\bar{t}H$ and $t\bar{t}Z$ production rates to this level already today. Using the HEPTOPTAGGER2 and applying its core improvements to the BDRS Higgs tagger, we translated the original LHC analysis of semileptonic $t\bar{t}H$ with $H \rightarrow b\bar{b}$ to the 100 TeV collider. The analysis gives rise to two peaks in the reconstructed m_{bb} distribution corresponding to the Higgs and the Z boson. Smooth side bands provide a handle to subtract the background, which is dominated by continuum $t\bar{t}b\bar{b}$ production. Provided sufficient knowledge of the branching ratio $H \rightarrow b\bar{b}$, we found that a determination of y_T at percent-level precision should be reachable.

Although a precision measurement of the top Yukawa coupling directly probes our understanding of electroweak symmetry breaking, the observed large hierarchy of fermion masses remains unexplained. In chapter V, we proposed a Froggatt-Nielsen-type model that not only offers an explanation of the mass hierarchy, but in addition yields a pseudoscalar degree of freedom, the flavon, that can be searched for at colliders. We studied current and projected bounds on the available parameter space from indirect searches in the quark and lepton flavor sector. While currently the most restricting bounds are set by kaon oscillations, upcoming lepton flavor experiments are expected to significantly cut into the available parameter space. Additionally, direct searches for the flavon can restrict the model. A feature of the proposed model is the large flavor-changing coupling to top and charm quarks. For light flavons, strong bounds therefore arise from anomalous top decays. For heavier masses most generic resonance searches will not reach the required sensitivity to discover the flavon, even with 30 ab^{-1} at a future 100 TeV proton-proton collider. However, associated production with a top quark in combination with the decay into a top and a charm quark gives rise to same-sign lepton signatures which allow to probe the parameter space for a first time at a future 100 TeV proton-proton collider.

Summing up, we employed top quarks in various contexts: from the search for new heavy resonances, precision tests of the Standard Model and finally as signatures of a model that might explain the hierarchy of fermion masses. Of course, these topics are only a small fraction of particle physics involving top quarks. Nevertheless, we are confident that the developed techniques and models indicate some new directions in top physics.

Acknowledgments

Here, at the end of this thesis and close to the end of my PhD studies there are many people I would like to thank. First of all, I am grateful to Tilman Plehn for accepting me as PhD student and all his advise and support during the past years. Jan Martin Pawlowski I thank for his commitment to referee this thesis. Without naming all of them explicitly, I enjoyed working with all my collaborators. Special acknowledgements go to Gregor Kasieczka for his contributions to the HEPTOPTAGGER. Furthermore, it has been a great pleasure working with and supervising Peter Reimitz, whom I wish all the best for his further path in physics. In addition, I want to mention the Heidelberg ATLAS group of André Schöning for various discussions, using the HEPTOPTAGGER within ATLAS and hospitality during their annual retreats. A very big thank you goes to the entire Heidelberg LHC pheno group for uncountable many physics discussions and a nice social embedding. Working with you has always been great fun! If this thesis should have resulted in a readable piece of text, this has been made possible by the careful reading of Anke Biekötter, Johann Brehmer, Patrick Foldenauer and Nikolai Zerf. Further, I acknowledge support from the International Max Planck Research School for Precision Tests of Fundamental Symmetries which has not only funded my studies but also allowed me to attend many conferences in Europe and the US. Most computations used to obtain the presented results have been made possible by bwHPC, especially the former bwGrid node in Heidelberg and the BWUniCluster in Karlsruhe. Finally, I want to thank my family and friends for their support. A last and special thank you goes to my wife Sabrina and my son Benjamin for all their patience especially during last weeks.

Appendix A: HEPTopTagger2 performance

Some of the improvements that were introduced in chapter III in the context of a $Z' \rightarrow t\bar{t}$ resonance search are directly connected to top tagging. Thus, they have been implemented in the HEPTOPTAGGER algorithm resulting in the new HEPTOPTAGGER2. In this appendix, we benchmark the HEPTOPTAGGER2 showing tagging efficiencies and mistagging rates obtained from continuum top pair production and QCD background events. All results have been published in Ref. [40], which also includes a description of the complete HEPTOPTAGGER2 code.

Our analyses are based on fully hadronic $t\bar{t}$ signal and QCD dijet background samples generated with PYTHIA8 [51]. For the general top tagger analysis in this appendix, we include underlying event in the event generation and mimic the limited detector resolution by clustering the hadronic activity into $(\eta \times \phi)$ cells of size (0.1×0.1) , similar to the QJETS resolution in Sec. III B 3. Instead of the hard acceptance cuts in Eq.(III.1), we now allow for softer fat jets. Two separate multivariate BDT analyses focus on $t\bar{t}$ samples with

$$p_{T,\text{fat}} > 200 \text{ GeV}, \quad |y_{\text{fat}}| < 2.5, \quad p_{T,t} > 200, 600 \text{ GeV}, \quad (\text{A.1})$$

where the top-quark momenta are evaluated on the Monte Carlo truth level. We select events with fat C/A jets of radius $R_{\text{fat}} = 1.8$ constructed with FASTJET [52].

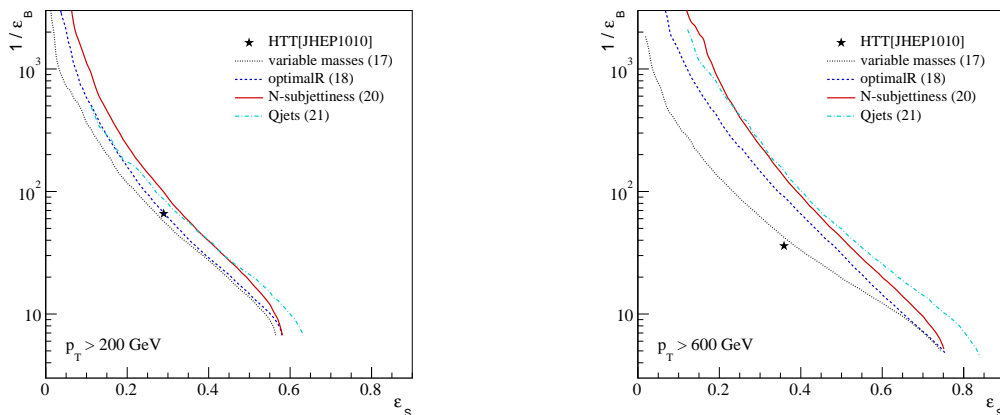


Figure A.1: Performance of the HEPTOPTAGGER2 for $t\bar{t}$ production in the Standard Model. We show the incremental improvements from the extended multivariate analyses for top quarks with $p_{T,t} > 200 \text{ GeV}$ and $p_{T,t} > 600 \text{ GeV}$. Taken from Ref. [40].

Background efficiencies ϵ_B are defined relative to the number of those fat jets. For the signal efficiencies we require that the fat jets can be matched to a parton-level top quark within $\Delta R < 0.8$. Using the original version of the HEPTOPTAGGER [37], we find for the $p_T > 600$ GeV samples a signal efficiency of $\epsilon_S = 35.6\%$ and a mistagging rate $\epsilon_B = 2.7\%$. The first change in the algorithm addresses the signal efficiency and background sculpting and has already been introduced in Ref. [38]. In the original algorithm the triplet of subjects closest to the true top-quark mass was selected and only later the mass-plane cuts were applied. Therefore, the tagger failed if this triplet did not pass the mass-plane constraints and no alternative triplet was analyzed. To eliminate this limitation, we now first apply the mass-plane constraints and then pick the triple closest to the top-quark mass, as described in Sec. II E.

As in the main text of Sec. III, we study further improvements of the tagger based on ROC curves. To allow for such improvements, we loosen the cuts of the tagger to $m_{\text{rec}} < 1$ TeV and $f_W = 0.3$. The initial set of BDT parameters in analogy to Eq.(III.4) is

$$\{ m_{\text{rec}}, f_{\text{rec}} \} \quad (\text{variable masses}). \quad (\text{A.2})$$

The optimalR mode accounts for the large cone size of $R = 1.8$, which is not always appropriate. Thus, the optimalR mode optimizes the radius of each fat jet. Starting from the initial cone size, we stepwise reduce the size of the fat jet until the criterion of Eq. (III.5) indicates that we miss parts of the top-quark decay. The output of the tagger is set to the result obtained at R_{opt} . In addition, we calculate the expected value $R_{\text{opt}}^{\text{calc}}$ for the critical radius based on the transverse momentum of the filtered fat jet as outlined in Sec. III B 1 using

$$R_{\text{opt}}^{\text{calc}} = \frac{327 \text{ GeV}}{p_{T,\text{filt}}}. \quad (\text{A.3})$$

For a fat jet originating from a top decay this prediction should agree with the measured value, while for a background fat jet the two are only strongly correlated when the entire subject kinematics is a perfect match to a top decay. For the optimalR mode we set up a

BDT analysis with the observables

$$\{ m_{\text{rec}}, f_{\text{rec}}, R_{\text{opt}} - R_{\text{opt}}^{(\text{calc})} \} \quad (\text{optimalR}). \quad (\text{A.4})$$

All tagging observables are evaluated at R_{opt} . The corresponding ROC curve in Fig. A.1 illustrates the improvement from the optimized size of the fat jet. Obviously, it is more impressive for larger boost, while for $p_{T,t} > 200$ GeV the optimalR mode hardly leads to a reduction of the fat jet size.

The N -subjettiness variables are best applied independently for fat jets which would pass and those which would not pass the initial tagging criterion. The optimalR working point that we use for this intermediate classification is

$$m_{\text{rec}} \in [150, 200] \text{ GeV} \quad f_{\text{rec}} < 0.175 \quad R_{\text{opt}} - R_{\text{opt}}^{(\text{calc})} < 0.3, \quad (\text{A.5})$$

and corresponds to the signal efficiency $\epsilon_S = 0.22(0.27)$ in Fig. A.1. Fat jets passing Eq.(A.5) are assumed to include a complete set of top decay products and are filtered with $R_{\text{filt}}^{(1)} = 0.2$ and $N_{\text{filter}}^{(1)} = 5$; fat jets failing this criterion are instead filtered with $R_{\text{filt}}^{(0)} = 0.3$ and $N_{\text{filter}}^{(0)} = 3$. The unfiltered N -subjettiness variables τ_i defined in Eq.(III.7) and their filtered counter parts $\tau_i^{(0)}, \tau_i^{(1)}$ are included for $i \leq 3$. The reference axes are chosen as k_T -axes. We then set up two independent BDTs with

$$\begin{aligned} & \{ m_{\text{rec}}, f_{\text{rec}}, R_{\text{opt}} - R_{\text{opt}}^{(\text{calc})}, m_{\text{fat}}^{(1)}, \tau_3^{(1)}, \tau_3^{(1)}/\tau_2^{(1)}, \tau_2^{(1)}/\tau_1^{(1)}, \\ & \quad \tau_2, \tau_3/\tau_2, \tau_2/\tau_1 \} \quad (N\text{-subjettiness, pass}) \\ & \{ m_{\text{rec}}, f_{\text{rec}}, R_{\text{opt}} - R_{\text{opt}}^{(\text{calc})}, m_{\text{fat}}^{(0)}, \tau_3^{(0)}, \tau_3^{(0)}/\tau_2^{(0)}, \tau_2^{(0)}/\tau_1^{(0)}, \\ & \quad \tau_1, \tau_3/\tau_2, \tau_2/\tau_1 \} \quad (N\text{-subjettiness, fail}), \end{aligned} \quad (\text{A.6})$$

and later combine them into one ROC curve. This precise condition is represented by the more generic Eq.(III.8). Figure A.1 summarizes the corresponding ROC curves for the successively improved tagger.

Finally, we can replace the deterministic C/A clustering history of the fat jet by a set of QJETS histories as explained in Sec. III B 3 with large global weights $\Omega^{(\alpha)}$ defined in

Eq.(III.10). As before, we set the rigidity for the clustering weights to $\alpha = 0.1$. These histories help in cases where the deterministic clustering history is misled during the selection of splittings in the usual jet algorithm. When defining jets as analysis objects for a hard process this does not pose a problem, but for subjet analyses it can have an effect.

Our analysis is based on 100 QJETS histories per fat jet. In Tab. A.1 we provide signal and background efficiencies. As reference value we use the default HEPTOPTAGGER2 with a fixed mass windows. Based on the 100 QJETS histories we define the fraction ϵ_{Qjets} of histories which leads to a top tag with the default tagging setup. We see that for moderately boosted top quarks the deterministic signal tagging efficiency can be reproduced by requiring 30% of the QJETS histories to deliver a positive tag. The corresponding mistag probability is slightly reduced compared to the deterministic tagger. For harder tops the corresponding value is around $\epsilon_{\text{Qjets}} > 20\%$, with no improvement in the background rejection.

As discussed in Sec. IIIB3 QJETS offers two strategies to improve the top tagger. To maximize the improvement in tagging performance and to limit the CPU time we base the multivariate analysis on the tagged history with the largest global weight. As additional parameters we include the value of ϵ_{Qjets} as well as the mean and variance of the m_{rec} distribution with the $\epsilon_{\text{Qjets}} \times 100$ QJETS entries, symbolically denoted as $\{m_{\text{rec}}^{\text{Qjets}}\}$. For the

	$t\bar{t}$	QCD		$t\bar{t}$	QCD
default HTT	0.337	0.0212	default HTT	0.465	0.0489
$\epsilon_{\text{Qjets}} > 0.1$	0.435	0.0318	$\epsilon_{\text{Qjets}} > 0.1$	0.524	0.0661
$\epsilon_{\text{Qjets}} > 0.2$	0.384	0.0231	$\epsilon_{\text{Qjets}} > 0.2$	0.447	0.0461
$\epsilon_{\text{Qjets}} > 0.3$	0.341	0.0174	$\epsilon_{\text{Qjets}} > 0.3$	0.388	0.0342
$\epsilon_{\text{Qjets}} > 0.4$	0.298	0.0123	$\epsilon_{\text{Qjets}} > 0.4$	0.336	0.0245
$\epsilon_{\text{Qjets}} > 0.5$	0.250	0.0089	$\epsilon_{\text{Qjets}} > 0.5$	0.281	0.0168
$\epsilon_{\text{Qjets}} > 0.6$	0.212	0.0064	$\epsilon_{\text{Qjets}} > 0.6$	0.236	0.0118
$\epsilon_{\text{Qjets}} > 0.7$	0.163	0.0036	$\epsilon_{\text{Qjets}} > 0.7$	0.181	0.0062
$\epsilon_{\text{Qjets}} > 0.8$	0.118	0.0021	$\epsilon_{\text{Qjets}} > 0.8$	0.133	0.0032
$\epsilon_{\text{Qjets}} > 0.9$	0.064	0.0007	$\epsilon_{\text{Qjets}} > 0.9$	0.069	0.0009

Table A.1: Tagging efficiencies for $p_T > 200$ GeV (left) and $p_T > 600$ GeV (right). ϵ_{Qjets} is defined as the number of QJETS tags per number of QJETS runs. For this table we tested 10.000 fat jets with 100 QJETS iterations.

BDT analysis we employ

$$\{ m_{\text{rec}}, f_{\text{rec}}, R_{\text{opt}} - R_{\text{opt}}^{(\text{calc})}, m_{\text{fat}}, \tau_N, \tau_N^{(\text{filt})}, \epsilon_{\text{Qjets}}, \{m_{\text{rec}}^{\text{Qjets}}\} \} \quad (\text{QJETS}). \quad (\text{A.7})$$

As usual, all tagger outputs are evaluated at R_{opt} and the clustering history with the largest global weight. The additional improvement is shown in Fig. A.1.

Because QJETS offers a variety of improvements to the tagger, we study different setups based on the stage with multivariate mass windows in Fig. A.2. We start by replacing the deterministic C/A output with the most likely QJETS history and including ϵ_{Qjets} in the multivariate analysis. This leads to a moderate improvement of the tagger at large transverse momenta and at large signal efficiencies. Adding the statistical information from the $\epsilon_{\text{Qjets}} \times 100$ entries in the m_{rec} information leads to a sizable improvement over a wide range of signal efficiencies. This is the mode we use for the Z' analysis as well as in Fig. A.1.

Next, we add the second-best QJETS history to the tagger, such that the multivariate tagger (including ϵ_{Qjets}) is free to construct a criterion based on one or two tags in the two best QJETS histories. For most of the ROC curves this comparably simple approach is as successful as the full statistical information. Finally, adding the statistical information on the m_{rec} distribution leads to an additional mild improvement.

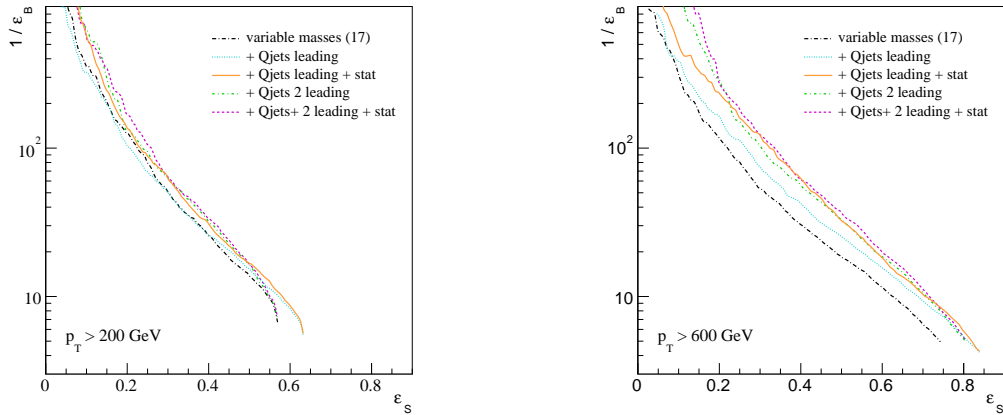


Figure A.2: Performance of the HEPTOPTAGGER2 for $t\bar{t}$ production in the Standard Model. For $p_{T,t} > 200$ GeV and $p_{T,t} > 600$ GeV. We focus on different QJETS setups, based on a more basic multivariate tagger without optimalR and N -subjettiness. Taken from Ref. [40].

Appendix B: More details on the flavon model

In chapter V, we studied the phenomenology of a Froggatt-Nielsen-type flavon model. This appendix provides more details on the model, derives some equations used in the analysis and gives the benchmark point that was used for our simulations.

Masses and couplings

In addition to the well-known Higgs part, the potential gains terms from the new complex scalar S

$$V(\Phi, S) = -\mu_S^2(S^*S) + \lambda_S(S^*S)^2 + \lambda_{\Phi S}(\Phi^\dagger\Phi)(S^*S) - b(S^2 + S^{*2}) + V(\Phi). \quad (\text{B.1})$$

We assume $\lambda_{\Phi S} = 0$ and thus have no mixing between the new scalar and the Higgs boson. The term $\propto b$ brakes the global $U(1)$ symmetry and allows us to give mass to the pseudoscalar flavon. The introduced phase dependence can be absorbed by a phase rotation of S . This allows us to locate the vacuum expectation value (VEV) f on the real axis and thus expand S around its VEV

$$S = \frac{f + s + ia}{\sqrt{2}}, \quad (\text{B.2})$$

where we label the scalar part s and the pseudoscalar flavon a . Note that the Higgs sector decouples due to $\lambda_{\Phi S} = 0$. Minimizing the potential yields

$$f^2 = \frac{\mu_S^2 + 2b}{\lambda_S}. \quad (\text{B.3})$$

The masses of the real-valued scalar s and the flavon a follow from the mass matrix $M^2 = \frac{d^2V}{d\{s,a\}}$ at the minimum as

$$m_s^2 = -\mu_S^2 + 3\lambda_S f^2 - 2b = 2\lambda_S f^2 \quad m_a^2 = 4b. \quad (\text{B.4})$$

The modified Yukawa terms in the Lagrangian generate the fermion mass terms and the couplings of the pseudoscalar flavon a . Here, we show the derivation for down-type quarks, where we neglect the Hermitian conjugate part for brevity. The masses for other fermions

follow analogously.

$$\begin{aligned}
\mathcal{L}_{\text{Yuk}} &\supset -y_{ij}^d \bar{Q}_{L_i} \left(\frac{S}{\Lambda} \right)^{n_{ij}^d} \Phi d_{R_j} \rightarrow -y_{ij}^d \bar{d}_{L_i} \left(\frac{f}{\sqrt{2}\Lambda} \right)^{n_{ij}^d} \frac{v}{\sqrt{2}} d_{R_j} \\
&= -y_{ij}^d \frac{v}{\sqrt{2}} \bar{d}_{L_i} \epsilon^{n_{ij}^d} d_{R_j} = -\bar{d}_{L_i} Y_{ij}^d \frac{v}{\sqrt{2}} d_{R_j} \\
&= -\bar{d}_{L_i} \widetilde{M}_{ij}^d d_{R_j} = -\bar{d}_{L_i} U_{ir}^d M_{rs}^d W_{sj}^{d\dagger} d_{R_j} \\
&= -\bar{d}_{L_i}^M m_i d_{R_i}^M .
\end{aligned} \tag{B.5}$$

In the second-to-last step, we diagonalized the mass matrix \widetilde{M} by two unitary matrices U^d and W^d . In addition to the masses, the modified Yukawa term dictates the couplings between the flavon and the fermions. The leading-order ϵ -dependence of the relevant quantities can be derived as [107]:

$$\begin{aligned}
m_{u_j} &\sim \frac{v}{\sqrt{2}} \epsilon^{a_j - a_{u_j}} , & m_{d_j} &\sim \frac{v}{\sqrt{2}} \epsilon^{a_j - a_{d_j}} , \\
U_{ij}^{u,d} &\sim \epsilon^{|a_i - a_j|} , & W_{ij}^u &\sim \epsilon^{|a_{u_i} - a_{u_j}|} , & W_{ij}^d &\sim \epsilon^{|a_{d_i} - a_{d_j}|} .
\end{aligned} \tag{B.6}$$

The quark mixing matrix follows in the usual way as

$$(V_{\text{CKM}})_{ij} = U_{ik}^{u\dagger} U_{kj}^d \sim \epsilon^{|a_i - a_j|} . \tag{B.7}$$

Corresponding relations hold in the lepton sector.

In addition to the fermion masses, the Yukawa terms in the Lagrangian determine the interactions between the flavon a and the fermions. The flavon couplings to fermions $g_{af_{L_i} f_{R_j}} = g_{aij}$ can be written as

$$\begin{aligned}
g_{aij}^d &= -\frac{i}{f} \left[\mathcal{Q}_{ij}^d m_i - \mathcal{D}_{ij} m_j - a_H m_i \delta_{ij} \right] , & g_{aij}^u &= -\frac{i}{f} \left[\mathcal{Q}_{ij}^u m_i - \mathcal{U}_{ij} m_j + a_H m_i \delta_{ij} \right] , \\
g_{aij}^\ell &= -\frac{i}{f} \left[\mathcal{L}_{ij}^\ell m_i - \mathcal{E}_{ij} m_j - a_H m_i \delta_{ij} \right] , & g_{aij}^\nu &= -\frac{i}{f} \left[\mathcal{L}_{ij}^\nu m_i - \mathcal{N}_{ij} m_j + a_H m_i \delta_{ij} \right] .
\end{aligned} \tag{B.8}$$

with

$$\begin{aligned}
\mathcal{Q}_{ij}^d &= a_{Q_k} U_{ki}^{d*} U_{kj}^d & \mathcal{D}_{ij} &= a_{Q_k} W_{ki}^{d*} W_{kj}^d & \mathcal{Q}_{ij}^u &= a_{Q_k} U_{ki}^{u*} U_{kj}^u & \mathcal{U}_{ij} &= a_{Q_k} W_{ki}^{u*} W_{kj}^u \\
\mathcal{L}_{ij}^\ell &= a_{L_k} U_{ki}^{\ell*} U_{kj}^\ell & \mathcal{E}_{ij} &= a_{L_k} W_{ki}^{\ell*} W_{kj}^\ell & \mathcal{L}_{ij}^\nu &= a_{L_k} U_{ki}^{\nu*} U_{kj}^\nu & \mathcal{N}_{ij} &= a_{L_k} W_{ki}^{\nu*} W_{kj}^\nu
\end{aligned} \tag{B.9}$$

A step-by-step derivation for the coupling to down-type quarks proceeds as:

$$\begin{aligned}
 \mathcal{L}_{\text{Yuk}} &\supset -y_{ij}^d \bar{Q}_{L_i} \left(\frac{S}{\Lambda} \right)^{n_{ij}^d} \Phi d_{R_j} \rightarrow -y_{ij}^d n_{ij}^d \bar{d}_{L_i} \left(\frac{f}{\sqrt{2}\Lambda} \right)^{n_{ij}^d-1} \left(\frac{s+ia}{\sqrt{2}\Lambda} \right) \frac{v}{\sqrt{2}} d_{R_j} \\
 &\supset -y_{ij}^d \frac{n_{ij}^d v}{\sqrt{2}} \bar{d}_{L_i} \epsilon^{n_{ij}^d-1} \left(\frac{ia}{\sqrt{2}\Lambda} \right) d_{R_j} = -y_{ij}^d \frac{in_{ij}^d v}{\sqrt{2}} \bar{d}_{L_i} \epsilon^{n_{ij}^d} \left(\frac{a}{f} \right) d_{R_j} \\
 &= -\frac{iv}{\sqrt{2}f} \bar{d}_{L_i} Y_{ij}^d n_{ij}^d d_{R_j} a = -\frac{iv}{\sqrt{2}f} \bar{d}_{L_i} Y_{ij}^d [a_{Q_i} - a_{d_j} - a_{a_H}] d_{R_j} a \\
 &= -\frac{iv}{\sqrt{2}f} \bar{d}_{L_i} U_{il}^d M_{lm} W_{mj}^{d\dagger} [a_{Q_i} - a_{d_j} - a_{a_H}] d_{R_j} a \\
 &= -\frac{iv}{\sqrt{2}f} \bar{d}_{L_r}^M U_{ri}^{d\dagger} U_{il}^d M_{lm} W_{mj}^{d\dagger} [a_{Q_i} - a_{d_j} - a_{a_H}] W_{js}^d d_{R_s}^M a \\
 &= -\frac{iv}{\sqrt{2}f} \bar{d}_{L_r}^M \left[a_{Q_i} U_{ri}^{d\dagger} U_{il}^d M_{lm} W_{mj}^{d\dagger} W_{js}^d - U_{ri}^{d\dagger} U_{il}^d M_{lm} W_{mj}^{d\dagger} W_{js}^d a_{d_j} \right. \\
 &\quad \left. - U_{ri}^{d\dagger} U_{il}^d M_{lm} W_{mj}^{d\dagger} W_{js}^d a_{a_H} \right] d_{R_s}^M a \\
 &= -\frac{iv}{\sqrt{2}f} \bar{d}_{L_r}^M \left[a_{Q_i} U_{ri}^{d\dagger} U_{il}^d M_{lm} \delta_{ms} - \delta_{rl} M_{lm} W_{mj}^{d\dagger} W_{js}^d a_{d_j} - a_H \delta_{rl} M_{lm} \delta_{ms} \right] d_{R_s}^M a \\
 &= -\frac{iv}{\sqrt{2}f} \bar{d}_{L_r}^M \left[\underbrace{a_{Q_i} U_{ri}^{d\dagger} U_{il}^d M_{ls}}_{=: \mathcal{Q}_{rs}} - M_{rm} \underbrace{W_{mj}^{d\dagger} W_{js}^d a_{d_j}}_{=: \mathcal{D}_{rs}} - a_H \delta_{rl} M_{lm} \delta_{ms} \right] d_{R_s}^M a \\
 &= -\frac{i}{f} \bar{d}_{L_r}^M [\mathcal{Q}_{rs} m_{ss} - m_{rr} \mathcal{D}_{rs} - a_H m_{ss} \delta_{rs}] d_{R_s}^M a \\
 &= -i g_{afL_i fR_j}^d \bar{d}_{L_i}^M d_{R_j}^M a .
 \end{aligned} \tag{B.10}$$

Finally, we quote formulae for the a pseudoscalar a decaying to gluons [165] and photons [165, 166]:

$$\Gamma(a \rightarrow gg) = \frac{1}{\sqrt{2}f^2} \frac{\alpha_s^2 m_a^3}{16\sqrt{2}\pi^3} \left| \sum_q \frac{g_{aqq} f}{m_{qq}} A_a \left(\frac{m_a^2}{4m_f^2} \right) \right|^2 \tag{B.11}$$

$$\Gamma(a \rightarrow \gamma\gamma) = \frac{1}{\sqrt{2}f^2} \frac{\alpha_{\text{em}}^2 m_a^3}{32\sqrt{2}\pi^3} \left| \sum_f \frac{g_{aff} f}{m_{ff}} N_{C,f} Q_f^2 A_a \left(\frac{m_a^2}{4m_f^2} \right) \right|^2 , \tag{B.12}$$

where

$$A_a(\tau) = \frac{f(\tau)}{\tau} \quad f(\tau) = \begin{cases} \arcsin^2 \sqrt{\tau} & \tau \leq 1 \\ -\frac{1}{4} \left(\log \left(\frac{1+\sqrt{1-\frac{1}{\tau}}}{1-\sqrt{1-\frac{1}{\tau}}} \right) - i\pi \right)^2 & \tau > 1 \end{cases} . \tag{B.13}$$

Benchmark point for the flavon model

In this section, we provide the point in parameter space that was used for the simulation. It is directly taken from Ref. [106].

To find sample parameter points, we generate random fundamental Yukawa couplings with $y_{ij}^{u,d} = |y_{ij}^{u,d}| e^{i\phi_{ij}^{u,d}}$ and $|y_{ij}^{u,d}| \in [0.5, 1.5]$ and $\phi_{ij}^{u,d} \in [0, 2\pi]$. The effective Yukawa couplings defined in Eq.(V.9) have to reproduce the quark and lepton masses, and mixing angles at the flavor breaking scale, which we take to be 1 TeV. For the numerical values we use Refs. [167, 168]. To this end we perform a χ^2 fit, with symmetrized 2σ errors and require $\chi^2 < 1/\text{d.o.f.}$. To illustrate the results in Sec. V, we define a benchmark point with the masses

$$\begin{aligned}
m_{u_i} &= (0.00138, 0.563, 150.1) \text{ GeV} \\
m_{d_i} &= (0.00342, 0.054, 2.29) \text{ GeV} \\
m_{\ell_i} &= (0.000513, 0.106, 1.81) \text{ GeV} \\
m_{\nu_i} &= (0.00161, 0.523, 3.79) \cdot 10^{-11} \text{ GeV},
\end{aligned} \tag{B.14}$$

and the mixing matrices

$$|V_{\text{CKM}}| = \begin{pmatrix} 0.974 & 0.226 & 0.0035 \\ 0.226 & 0.974 & 0.0388 \\ 0.011 & 0.037 & 0.999 \end{pmatrix}, \quad |V_{\text{PMNS}}| = \begin{pmatrix} 0.813 & 0.565 & 0.142 \\ 0.483 & 0.519 & 0.705 \\ 0.324 & 0.642 & 0.695 \end{pmatrix}. \tag{B.15}$$

The corresponding Yukawa couplings in the quark sector are

$$\begin{aligned}
y_u &= \begin{pmatrix} 0.34 + 0.82i & -0.23 + 0.69i & 0.41 - 0.43i \\ -0.84 + 0.26i & -0.64 + 0.32i & 1.35 - 0.24i \\ 0.98 - 0.90i & -0.84 - 1.20i & 0.75 + 0.65i \end{pmatrix} \\
y_d &= \begin{pmatrix} 0.53 + 0.72i & 0.50 - 0.34i & 0.65 - 0.10i \\ 1.12 - 0.14i & 0.93 - 0.54i & -0.31 - 0.65i \\ -0.16 + 0.6i & -0.73 + 0.34i & 0.84 + 0.61i \end{pmatrix},
\end{aligned} \tag{B.16}$$

while the lepton sector is described by

$$\begin{aligned}
 y_\nu &= \begin{pmatrix} -0.73 - 0.49i & 0.91 - 0.68i & 0.50 - 0.21i \\ 0.77 + 0.36i & 0.59 + 0.84i & 0.23 - 1.19i \\ -0.29 + 1.14i & -0.02 - 0.59i & 1.15 + 0.91i \end{pmatrix} \\
 y_\ell &= \begin{pmatrix} 0.16 + 1.29i & -0.95 - 0.97i & 0.25 + 0.92i \\ 0.008 - 0.99i & 1.11 + 0.40i & 0.47 + 0.48i \\ 0.30 - 1.30i & 0.22 + 0.77i & -0.59 - 0.018i \end{pmatrix}.
 \end{aligned}$$

We note that this benchmark point is not optimized to illustrate specific features linked to quark flavor, lepton flavor, and collider reaches. The quark flavor and collider sector on the one hand, and the lepton sector on the other, are only loosely related. All couplings are deliberately chosen in the weakly interacting regime, to avoid conclusions too closely tied to assumptions about underlying ultraviolet completions.

References

The References are sorted in citation order.

- [1] S. L. Glashow, "Partial Symmetries of Weak Interactions," Nucl. Phys. **22**, 579 (1961).
- [2] S. Weinberg, "A Model of Leptons," Phys. Rev. Lett. **19**, 1264 (1967).
- [3] A. Salam, "Weak and electromagnetic interactions," in Elementary particle theory: relativistic groups and analyticity, N. Svartholm, ed., p.367. Almqvist & Wiskell, 1968. Proceedings of the eighth Nobel symposium.
- [4] P. W. Higgs, "Broken symmetries, massless particles and gauge fields," Phys. Lett. **12**, 132 (1964).
- [5] P. W. Higgs, "Broken symmetries and the masses of gauge bosons," Phys. Rev. Lett. **13**, 508 (1964).
- [6] F. Englert and R. Brout, "Broken symmetry and the mass of gauge vector mesons," Phys. Rev. Lett. **13**, 321 (1964).
- [7] ATLAS Collaboration, "Observation of a new particle in the search for the Standard Model Higgs boson with the ATLAS detector at the LHC," Phys. Lett. B **716**, 1 (2012).
- [8] CMS Collaboration, "Observation of a new boson at a mass of 125 GeV with the CMS experiment at the LHC," Phys. Lett. B **716**, 30 (2012).
- [9] G. Bertone, D. Hooper and J. Silk, "Particle dark matter: Evidence, candidates and constraints," Phys. Rept. **405**, 279 (2005).
- [10] S. Weinberg, "Implications of Dynamical Symmetry Breaking," Phys. Rev. D **13**, 974 (1976); E. Gildener, "Gauge Symmetry Hierarchies," Phys. Rev. D **14**, 1667 (1976); S. Weinberg, "Implications of Dynamical Symmetry Breaking: An Addendum," Phys. Rev. D **19**, 1277 (1979); L. Susskind, "Dynamics of Spontaneous Symmetry Breaking in the Weinberg-Salam Theory," Phys. Rev. D **20**, 2619 (1979).
- [11] R. N. Mohapatra *et al.*, "Theory of neutrinos: A White paper," Rept. Prog. Phys. **70**, 1757 (2007).
- [12] M. Klute, R. Lafaye, T. Plehn, M. Rauch and D. Zerwas, "Measuring Higgs Couplings at a Linear Collider," Europhys. Lett. **101**, 51001 (2013).
- [13] R. Brock *et al.*, "Planning the Future of U.S. Particle Physics (Snowmass 2013): Chapter 3: Energy Frontier," arXiv:1401.6081 [hep-ex].
- [14] C. P. Burgess and G. D. Moore, "The standard model: A primer," Cambridge Univ. Press, 2007.
- [15] M. E. Peskin and D. V. Schroeder, "An Introduction to Quantum Field Theory," Westview Press, 2007.
- [16] M. Srednicki, "Quantum Field Theory," Cambridge Univ. Press, 2010.

-
- [17] R. K. Ellis, W. J. Stirling, B. R. Webber, QCD and collider physics, Camb. Monogr. Part. Phys. Nucl. Phys. Cosmol. 8 (1996) 1435.
- [18] T. Plehn, “Lectures on LHC Physics,” Lect. Notes Phys. **844**, 1 (2012).
- [19] Particle Data Group Collaboration, “Review of Particle Physics,” Chin. Phys. C **38**, 090001 (2014).
- [20] A. Buckley *et al.*, “General-purpose event generators for LHC physics,” Phys. Rept. **504**, 145 (2011).
- [21] see *e.g.* G. Degrandi, S. Di Vita, J. Elias-Miro, J. R. Espinosa, G. F. Giudice, G. Isidori and A. Strumia, “Higgs mass and vacuum stability in the Standard Model at NNLO,” JHEP **1208**, 098 (2012); S. Alekhin, A. Djouadi and S. Moch, “The top quark and Higgs boson masses and the stability of the electroweak vacuum,” Phys. Lett. B **716**, 214 (2012); L. A. Anchordoqui, I. Antoniadis, H. Goldberg, X. Huang, D. Lüster, T. R. Taylor and B. Vlack, “Vacuum Stability of Standard Model⁺⁺,” JHEP **1302**, 074 (2013); D. Buttazzo, G. Degrandi, P. P. Giardino, G. F. Giudice, F. Sala, A. Salvio and A. Strumia, “Investigating the near-criticality of the Higgs boson,” JHEP **1312**, 089 (2013); F. Bezrukov and M. Shaposhnikov, “Why should we care about the top quark Yukawa coupling?,” J. Exp. Theor. Phys. **120**, 335 (2015); A. Eichhorn, H. Gies, J. Jaeckel, T. Plehn, M. M. Scherer and R. Sondenheimer, “The Higgs Mass and the Scale of New Physics,” JHEP **1504**, 022 (2015); F. Loebbert and J. Plefka, “Quantum Gravitational Contributions to the Standard Model Effective Potential and Vacuum Stability,” Mod. Phys. Lett. A **30**, no. 34, 1550189 (2015).
- [22] P. Langacker, “The Physics of Heavy Z' Gauge Bosons,” Rev. Mod. Phys. **81**, 1199 (2009).
- [23] ZEUS and H1 Collaborations, “PDF Fits at HERA,” PoS EPS -HEP2011, 320 (2011).
- [24] <http://sherpa.hepforge.org/event.png>.
- [25] T. Kinoshita, “Mass singularities of Feynman amplitudes,” J. Math. Phys. **3**, 650 (1962).
T. D. Lee and M. Nauenberg, “Degenerate Systems and Mass Singularities,” Phys. Rev. **133**, B1549 (1964).
R. Akhoury and V. I. Zakharov, “A Quick look at renormalons,” Nucl. Phys. Proc. Suppl. **54A**, 217 (1997).
- [26] B. Andersson, G. Gustafson, G. Ingelman and T. Sjostrand, “Parton Fragmentation and String Dynamics,” Phys. Rept. **97**, 31 (1983); B. Andersson, “The Lund model,” Camb. Monogr. Part. Phys. Nucl. Phys. Cosmol. **7**, 1 (1997).
- [27] B. R. Webber, “A QCD Model for Jet Fragmentation Including Soft Gluon Interference,” Nucl. Phys. B **238**, 492 (1984); J. C. Winter, F. Krauss and G. Soff, “A Modified cluster hadronization model,” Eur. Phys. J. C **36**, 381 (2004).
- [28] M. Selvaggi, “DELPHES 3: A modular framework for fast-simulation of generic collider experiments,” J. Phys. Conf. Ser. **523** (2014) 012033.

- [29] S. Catani, Y. L. Dokshitzer, M. Olsson, G. Turnock and B. R. Webber, “New clustering algorithm for multi - jet cross-sections in $e^+ e^-$ Phys. Lett. B **269**, 432 (1991); S. Catani, Y. L. Dokshitzer, M. H. Seymour and B. R. Webber, “Longitudinally Invariant K(T) Clustering Algorithms For Hadron Hadron Nucl. Phys. B **406**, 187 (1993); S. D. Ellis and D. E. Soper, “Successive combination jet algorithm for hadron collisions,” Phys. Rev. D **48**, 3160 (1993).
- [30] Y. L. Dokshitzer, G. D. Leder, S. Moretti and B. R. Webber, “Better Jet Clustering Algorithms,” JHEP **9708**, 001 (1997); M. Wobisch and T. Wengler, “Hadronization corrections to jet cross sections in deep-inelastic scattering,” arXiv:hep-ph/9907280.
- [31] M. Cacciari, G. P. Salam and G. Soyez, “The Anti-k(t) jet clustering algorithm,” JHEP **0804**, 063 (2008).
- [32] M. Dasgupta, L. Magnea and G. P. Salam, “Non-perturbative QCD effects in jets at hadron colliders,” JHEP **0802**, 055 (2008).
- [33] J. M. Butterworth, A. R. Davison, M. Rubin and G. P. Salam, “Jet substructure as a new Higgs search channel at the LHC,” Phys. Rev. Lett. **100**, 242001 (2008).
- [34] S. D. Ellis, C. K. Vermilion and J. R. Walsh, “Techniques for improved heavy particle searches with jet substructure,” Phys. Rev. D **80**, 051501 (2009); S. D. Ellis, C. K. Vermilion and J. R. Walsh, “Recombination Algorithms and Jet Substructure: Pruning as a Tool for Heavy Particle Searches,” Phys. Rev. D **81**, 094023 (2010); C. K. Vermilion, “Jet Substructure at the Large Hadron Collider: Harder, Better, Faster, Stronger,” arXiv:1101.1335 [hep-ph].
- [35] D. Krohn, J. Thaler and L. T. Wang, “Jet Trimming,” JHEP **1002**, 084 (2010).
- [36] T. Plehn, G. P. Salam and M. Spannowsky, “Fat Jets for a Light Higgs,” Phys. Rev. Lett. **104**, 111801 (2010).
- [37] T. Plehn, M. Spannowsky, M. Takeuchi, and D. Zerwas, “Stop Reconstruction with Tagged Tops,” JHEP **1010**, 078 (2010).
- [38] T. Plehn, M. Spannowsky and M. Takeuchi, “How to Improve Top Tagging,” Phys. Rev. D **85**, 034029 (2012).
- [39] C. Anders, C. Bernaciak, G. Kasieczka, T. Plehn and T. Schell, “Benchmarking an even better top tagger algorithm,” Phys. Rev. D **89**, no. 7, 074047 (2014).
- [40] G. Kasieczka, T. Plehn, T. Schell, T. Strebler and G. P. Salam, “Resonance Searches with an Updated Top Tagger,” JHEP **1506**, 203 (2015).
- [41] CMS Collaboration, TWiki zu CMS-PAS-JME-13-007, https://twiki.cern.ch/twiki/pub/CMSPublic/PhysicsResultsJME13007/HEP_one_slide_description.pdf.
- [42] ATLAS Collaboration, “Identification of high transverse momentum top quarks in pp collisions at $\sqrt{s} = 8$ TeV with the ATLAS detector,” JHEP **1606**, 093 (2016).
- [43] ATLAS Collaboration, “Search for resonances decaying into top-quark pairs using fully hadronic decays in pp collisions with ATLAS at $\sqrt{s} = 7$ TeV,” JHEP **1301**, 116 (2013); AT-

-
- LAS Collaboration, “Performance of boosted top quark identification in 2012 ATLAS data” ATLAS-CONF-2013-084; ATLAS Collaboration, “Search for Resonances Decaying into Top Quark Pairs Using Fully Hadronic Decays in pp Collisions with ATLAS at $\sqrt{s} = 7$ TeV,” ATLAS-CONF-2012-102; G. Piacquadio, “Identification of b-jets and investigation of the discovery potential of a Higgs boson in the $WH \rightarrow l\nu b\bar{b}$ channel with the ATLAS experiment,” CERN-THESIS-2010-027; G. Kasieczka, “Search for Resonances Decaying into Top Quark Pairs Using Fully Hadronic Decays in pp Collisions with ATLAS at $\sqrt{s} = 7$ TeV” PhD thesis, <http://www.ub.uni-heidelberg.de/archiv/14941>.
- [44] CMS Collaboration, “Search for $t\bar{t}H$ production in the $H \rightarrow b\bar{b}$ decay channel with $\sqrt{s} = 13$ TeV pp collisions at the CMS experiment,” CMS-PAS-HIG-16-004. CMS Collaboration, “Top Tagging with New Approaches,” CMS-PAS-JME-15-002. CMS Collaboration, “Search for resonant $t\bar{t}$ production in proton-proton collisions at $\sqrt{s} = 8$ TeV,” Phys. Rev. D **93**, no. 1, 012001 (2016).
- [45] A. Höcker *et al.*, J. Stelzer, F. Tegenfeldt, H. Voss, K. Voss, A. Christov, S. Henrot-Versille and M. Jachowski “TMVA - Toolkit for Multivariate Data Analysis,” PoS ACAT, 040 (2007) [physics/0703039 [PHYSICS]]; P. Speckmayer, A. Höcker, J. Stelzer and H. Voss, “The toolkit for multivariate data analysis, TMVA 4,” J. Phys. Conf. Ser. **219**, 032057 (2010).
- [46] R. Brun and F. Rademakers, “ROOT: An object oriented data analysis framework,” Nucl. Instrum. Meth. A **389**, 81 (1997).
- [47] Y. Freund and R. E. Schapire, “A decision-theoretic generalization of on-line learning and an application to Boosting,” J. of Computer and System Science 55, 119 (1997).
- [48] see *e.g.* K. Agashe, A. Belyaev, T. Krupovnickas, G. Perez and J. Virzi, “LHC Signals from Warped Extra Dimensions,” Phys. Rev. D **77**, 015003 (2008); V. Barger, T. Han and D. G. E. Walker, “Top Quark Pairs at High Invariant Mass: A Model-Independent Discriminator Phys. Rev. Lett. **100**, 031801 (2008); B. Lillie, L. Randall and L. -T. Wang, “The Bulk RS KK-gluon at the LHC,” JHEP **0709**, 074 (2007); U. Baur and L. H. Orr, “High p_T Top Quarks at the Large Hadron Collider,” Phys. Rev. D **76**, 094012 (2007); U. Baur and L. H. Orr, “Searching for $t\bar{t}$ Resonances at the Large Hadron Collider,” Phys. Rev. D **77**, 114001 (2008); P. Fileviez Perez, R. Gavin, T. McElmurry and F. Petriello, “Grand Unification and Light Color-Octet Scalars at the LHC,” Phys. Rev. D **78**, 115017 (2008).
- [49] L. G. Almeida, S. J. Lee, G. Perez, I. Sung and J. Virzi, “Top Jets at the LHC,” Phys. Rev. D **79**, 074012 (2009); L. G. Almeida, S. J. Lee, G. Perez, G. F. Sterman, I. Sung and J. Virzi, “Substructure of high- p_T Jets at the LHC,” Phys. Rev. D **79**, 074017 (2009); L. G. Almeida, S. J. Lee, G. Perez, G. Sterman, I. Sung, “Template Overlap Method for Massive Jets,” Phys. Rev. **D82**, 054034 (2010); M. Backovic and J. Juknevich, “TemplateTagger v1.0.0: A Template Matching Tool for Jet Substructure,” Comput. Phys. Commun. **185**, 1322 (2014).

-
- [50] D. E. Soper and M. Spannowsky, “Finding physics signals with event deconstruction,” *Phys. Rev. D* **89**, no. 9, 094005 (2014).
- [51] T. Sjöstrand, S. Ask, J. R. Christiansen, R. Corke, N. Desai, P. Ilten, S. Mrenna and S. Prestel *et al.*, “An Introduction to PYTHIA 8.2,” *Comput. Phys. Commun.* **191** (2015) 159.
- [52] M. Cacciari and G. P. Salam, “Dispelling the N^3 myth for the k_t jet-finder,” *Phys. Lett. B* **641**, 57 (2006); M. Cacciari, G. P. Salam and G. Soyez, “FastJet User Manual,” *Eur. Phys. J. C* **72**, 1896 (2012);
- [53] J. Thaler and K. Van Tilburg, “Identifying Boosted Objects with N-subjettiness,” *JHEP* **1103**, 015 (2011); J. Thaler and K. Van Tilburg, “Maximizing Boosted Top Identification by Minimizing N-subjettiness,” *JHEP* **1202**, 093 (2012); I. W. Stewart, F. J. Tackmann and W. J. Waalewijn, “N-Jettiness: An Inclusive Event Shape to Veto Jets,” *Phys. Rev. Lett.* **105**, 092002 (2010).
- [54] D. E. Kaplan, K. Rehermann, M. D. Schwartz and B. Tweedie, “Top Tagging: A Method for Identifying Boosted Hadronically Decaying Top Phys. Rev. Lett. **101**, 142001 (2008).
- [55] Y. T. Chien, “Telescoping Jets: Multiple Event Interpretations with Multiple R’s,” *Phys. Rev. D* **90**, 054008 (2014).
- [56] D. Krohn, J. Thaler and L. T. Wang, “Jets with Variable R,” *JHEP* **0906**, 059 (2009).
- [57] T. Lapsien, R. Kogler and J. Haller, “A new tagger for hadronically decaying heavy particles at the LHC,” *Eur. Phys. J. C* **76**, no. 11, 600 (2016).
- [58] for an extension beyond the usual fat jet approach see M. Stoll, “Vetoed jet clustering: The mass-jump algorithm,” *JHEP* **1504** (2015) 111.
- [59] T. Plehn and T. Schell, “Multivariate comparison of the HOTVR and the HEPTopTagger” (working title), in preparation.
- [60] T. Strebler, Master thesis, ETH Zürich (2014).
- [61] for a possible improvement over N -subjettiness see A. J. Larkoski, I. Moult and D. Neill, “Power Counting to Better Jet Observables,” *JHEP* **1412**, 009 (2014); A. J. Larkoski, I. Moult and D. Neill, “Building a Better Boosted Top Tagger,” *Phys. Rev. D* **91**, no. 3, 034035 (2015).
- [62] S. D. Ellis, A. Hornig, T. S. Roy, D. Krohn and M. D. Schwartz, “Qjets: A Non-Deterministic Approach to Tree-Based Jet Substructure,” *Phys. Rev. Lett.* **108**, 182003 (2012); S. D. Ellis, A. Hornig, D. Krohn and T. S. Roy, “On Statistical Aspects of Qjets,” *JHEP* **1501**, 022 (2015).
- [63] see *e.g.* C. Englert, T. Plehn, P. Schichtel and S. Schumann, “Jets plus Missing Energy with an Autofocus,” *Phys. Rev. D* **83**, 095009 (2011); S. Ask, J. H. Collins, J. R. Forshaw, K. Joshi and A. D. Pilkington, “Identifying the colour of TeV-scale resonances,” *JHEP* **1201**, 018 (2012); E. Gerwick, T. Plehn, S. Schumann and P. Schichtel, “Scaling Patterns for QCD Jets,” *JHEP* **1210**, 162 (2012); E. Gerwick, S. Schumann, B. Gripaios and B. Webber, “QCD

-
- Jet Rates with the Inclusive Generalized kt Algorithms,” *JHEP* **1304**, 089 (2013); Z. Bern, L. J. Dixon, F. Febres Cordero, S. Höche, H. Ita, D. A. Kosower, D. Maitre and K. J. Ozeren, “Next-to-Leading Order $W + 5$ -Jet Production at the LHC,” *Phys. Rev. D* **88**, no. 1, 014025 (2013).
- [64] D. E. Soper and M. Spannowsky, “Finding top quarks with shower deconstruction,” *Phys. Rev. D* **87**, 054012 (2013);
- [65] for some early examples see e.g. K. Kondo, “Dynamical Likelihood Method for Reconstruction of Events With Missing Momentum. 1: Method and Toy Models,” *J. Phys. Soc. Jap.* **57**, 4126 (1988); D. Atwood and A. Soni, “Analysis for magnetic moment and electric dipole moment form-factors of the top quark via $e^+e^- \rightarrow t\bar{t}$,” *Phys. Rev. D* **45**, 2405 (1992); D0 Collaboration, “Helicity of the W boson in lepton + jets $t\bar{t}$ events,” *Phys. Lett. B* **617**, 1 (2005); CDF Collaboration, “Measurement of the top quark mass with the dynamical likelihood method using *Phys. Rev. D* **73**, 092002 (2006); D0 Collaboration, *Nature* **429**, 638 (2004).
- [66] M. L. Mangano, T. Plehn, P. Reimitz, T. Schell and H. S. Shao, “Measuring the Top Yukawa Coupling at 100 TeV,” *J. Phys. G* **43**, no. 3, 035001 (2016).
- [67] For a comprehensive analysis of Run I data see e.g. T. Corbett, O. J. P. Eboli, D. Goncalves, J. Gonzalez-Fraile, T. Plehn and M. Rauch, “The Higgs Legacy of the LHC Run I,” *JHEP* **1508**, 156 (2015).
- [68] CMS Collaboration, “Search for the associated production of the Higgs boson with a top-quark pair,” *JHEP* **1409**, 087 (2014) [Erratum-ibid. **1410**, 106 (2014)]; ATLAS Collaboration, “Search for $H \rightarrow \gamma\gamma$ produced in association with top quarks and constraints on the Yukawa coupling between the top quark and the Higgs boson using data taken at 7 TeV and 8 TeV with the ATLAS detector,” *Phys. Lett. B* **740**, 222 (2015); CMS Collaboration, “Search for a Standard Model Higgs Boson Produced in Association with a Top-Quark Pair and Decaying to Bottom Quarks Using a Matrix Element Method,” *Eur. Phys. J. C* **75**, no. 6, 251 (2015).
- [69] V. Drollinger, T. Müller and D. Denegri, “Searching for Higgs bosons in association with top quark pairs in the $H_0 \rightarrow b\bar{b}$ decay mode,” hep-ph/0111312; J. Cammin and M. Schumacher, “The ATLAS discovery potential for the channel $t\bar{t}H, H \rightarrow b\bar{b}$,” ATL-PHYS-2003-024; P. Artoisenet, P. de Aquino, F. Maltoni and O. Mattelaer, “Unravelling $t\bar{t}h$ via the matrix element method,” *Phys. Rev. Lett.* **111**, 091802 (2013); D. Curtin, J. Galloway and J. G. Wacker, “Measuring the $t\bar{t}h$ coupling from SSDL+2b measurements,” *Phys. Rev. D* **88**, 093006 (2013); P. Agrawal, S. Bandyopadhyay and S. P. Das, “Multilepton Signatures of the Higgs Boson through its Production in Association with a Top-quark Pair,” *Phys. Rev. D* **88**, 093008 (2013); M. R. Buckley, T. Plehn, T. Schell and M. Takeuchi, “Buckets of Higgs and Tops,” *JHEP* **1402**, 130 (2014).
- [70] LHC/LC Study Group Collaboration, “Physics interplay of the LHC and the ILC,” *Phys.*

- Rept. **426**, 47 (2006);
- [71] ILC Collaboration, “ILC Reference Design Report: ILC Global Design Effort and World Wide Study,” arXiv:0712.1950 [physics.acc-ph].
- [72] Future Circular Collider Study Group, “Future Circular Collider Study, Hadron Collider Parameters,” Tech. Rep. FCC-ACC-SPC-0001, M. Benedikt, “FCC study overview and status”, talk at the FCC week 2015, Washington D.C., 23-29 March 2015, <http://indico.cern.ch/event/340703/session/108/contribution/186>; I. Hinchliffe, A. Kotwal, M. L. Mangano, C. Quigg and L. T. Wang, “Luminosity goals for a 100-TeV pp collider,” Int. J. Mod. Phys. A **30**, no. 23 (2015).
- [73] CEPC-SPPC Study Group, “CEPC-SPPC Preliminary Conceptual Design Report. 1. Physics and Detector,” IHEP-CEPC-DR-2015-01, IHEP-TH-2015-01, IHEP-EP-2015-01.
- [74]
- [75] B. S. Acharya, K. Bozek, C. Pongkitivanichkul and K. Sakurai, “Prospects for observing charginos and neutralinos at a 100 TeV proton-proton collider,” JHEP **1502**, 181 (2015); S. Gori, S. Jung, L. T. Wang and J. D. Wells, “Prospects for Electroweakino Discovery at a 100 TeV Hadron Collider,” JHEP **1412**, 108 (2014); J. Bramante, P. J. Fox, A. Martin, B. Ostdiek, T. Plehn, T. Schell and M. Takeuchi, “Relic neutralino surface at a 100 TeV collider,” Phys. Rev. D **91**, 054015 (2015); A. Berlin, T. Lin, M. Low and L. T. Wang, “Neutralinos in Vector Boson Fusion at High Energy Colliders,” Phys. Rev. D **91**, no. 11, 115002 (2015); S. A. R. Ellis and B. Zheng, “Reaching for squarks and gauginos at a 100 TeV p-p collider,” Phys. Rev. D **92**, no. 7, 075034 (2015).
- [76]
- [77] D. Curtin, P. Meade and C. T. Yu, “Testing Electroweak Baryogenesis with Future Colliders,” JHEP **1411**, 127 (2014).
- [78] U. Baur, T. Plehn and D. L. Rainwater, “Probing the Higgs selfcoupling at hadron colliders using rare decays,” Phys. Rev. D **69**, 053004 (2004); A. J. Barr, M. J. Dolan, C. Englert, D. E. Ferreira de Lima and M. Spannowsky, “Higgs Self-Coupling Measurements at a 100 TeV Hadron Collider,” JHEP **1502**, 016 (2015); A. V. Kotwal, S. Chekanov and M. Low, “Double Higgs Boson Production in the 4τ Channel from Resonances in Longitudinal Vector Boson Scattering at a 100 TeV Collider,” Phys. Rev. D **91**, no. 11, 114018 (2015). W. Yao, “Studies of measuring Higgs self-coupling with $HH \rightarrow b\bar{b}\gamma\gamma$ at the future hadron colliders,” arXiv:1308.6302 [hep-ph]; H. J. He, J. Ren and W. Yao, “Probing new physics of cubic Higgs boson interaction via Higgs pair production at hadron colliders,” Phys. Rev. D **93** (2016) no.1, 015003; A. Azatov, R. Contino, G. Panico and M. Son, “Effective field theory analysis of double Higgs boson production via gluon fusion,” Phys. Rev. D **92**, no. 3, 035001 (2015).
- [79] R. Lafaye, T. Plehn, M. Rauch, D. Zerwas and M. Dürrssen, “Measuring the Higgs Sector,”

-
- JHEP **0908**, 009 (2009); K. Cranmer, S. Kreiss, D. Lopez-Val and T. Plehn, “Decoupling Theoretical Uncertainties from Measurements of the Higgs Boson,” Phys. Rev. D **91**, no. 5, 054032 (2015).
- [80] J. R. Christiansen and T. Sjöstrand, “Weak Gauge Boson Radiation in Parton Showers,” JHEP **1404**, 115 (2014); F. Krauss, P. Petrov, M. Schoenherr and M. Spannowsky, “Measuring collinear W emissions inside jets,” Phys. Rev. D **89**, no. 11, 114006 (2014); T. Cohen, R. T. D’Agnolo, M. Hance, H. K. Lou and J. G. Wacker, “Boosting Stop Searches with a 100 TeV Proton Collider,” JHEP **1411**, 021 (2014); A. J. Larkoski and J. Thaler, “Aspects of jets at 100 TeV,” Phys. Rev. D **90**, no. 3, 034010 (2014); T. Han, J. Sayre and S. Westhoff, “Top-Quark Initiated Processes at High-Energy Hadron Colliders,” JHEP **1504**, 145 (2015); J. A. Aguilar-Saavedra, B. Fuks and M. L. Mangano, “Pinning down top dipole moments with ultra-boosted tops,” Phys. Rev. D **91**, 094021 (2015); A. J. Larkoski, F. Maltoni and M. Selvaggi, “Tracking down hyper-boosted top quarks,” JHEP **1506**, 032 (2015);
- [81] K. Fujii *et al.*, “Physics Case for the International Linear Collider,” arXiv:1506.05992 [hep-ex].
- [82] TLEP Design Study Working Group Collaboration, “First Look at the Physics Case of TLEP,” JHEP **1401**, 164 (2014).
- [83] L. Linssen, A. Miyamoto, M. Stanitzki and H. Weerts, “Physics and Detectors at CLIC: CLIC Conceptual Design Report,” arXiv:1202.5940 [physics.ins-det].
- [84] LHC Higgs Cross Section Working Group Collaboration, “Handbook of LHC Higgs Cross Sections: 1. Inclusive Observables,” arXiv:1101.0593 [hep-ph].
- [85] C. Anastasiou, C. Duhr, F. Dulat, F. Herzog and B. Mistlberger, “Higgs Boson Gluon-Fusion Production in QCD at Three Loops,” Phys. Rev. Lett. **114**, 212001 (2015).
- [86] J. Rojo *et al.*, “The PDF4LHC report on PDFs and LHC data: Results from Run I and preparation for Run II,” J. Phys. G **42**, 103103 (2015).
- [87] M. Czakon, P. Fiedler and A. Mitov, “Total Top-Quark Pair-Production Cross Section at Hadron Colliders Through $O(\frac{4}{9})$,” Phys. Rev. Lett. **110**, 252004 (2013).
- [88] W. Beenakker, S. Dittmaier, M. Krämer, B. Plümper, M. Spira and P. M. Zerwas, “NLO QCD corrections to t anti-t H production in hadron collisions,” Nucl. Phys. B **653**, 151 (2003); S. Dawson, C. Jackson, L. H. Orr, L. Reina and D. Wackerth, “Associated Higgs production with top quarks at the large hadron collider: NLO QCD corrections,” Phys. Rev. D **68**, 034022 (2003).
- [89] A. Denner and R. Feger, “NLO QCD corrections to off-shell top-antitop production with leptonic decays in association with a Higgs boson at the LHC,” JHEP **1511** (2015) 209.
- [90] A. Lazopoulos, T. McElmurry, K. Melnikov and F. Petriello, “Next-to-leading order QCD corrections to $t\bar{t}Z$ production at the Phys. Lett. B **666**, 62 (2008).
- [91] S. Frixione, V. Hirschi, D. Pagani, H. S. Shao and M. Zaro, “Weak corrections to Higgs

- hadroproduction in association with a top-quark pair,” JHEP **1409**, 065 (2014).
- [92] S. Frixione, V. Hirschi, D. Pagani, H.-S. Shao and M. Zaro, “Electroweak and QCD corrections to top-pair hadroproduction in association with heavy bosons,” JHEP **1506**, 184 (2015).
- [93] J. Alwall *et al.*, “The automated computation of tree-level and next-to-leading order differential cross sections, and their matching to parton shower simulations,” JHEP **1407**, 079 (2014).
- [94] A. D. Martin, W. J. Stirling, R. S. Thorne and G. Watt, “Parton distributions for the LHC,” Eur. Phys. J. C **63**, 189 (2009).
- [95] M. R. Whalley, D. Bourilkov and R. C. Group, “The Les Houches accord PDFs (LHAPDF) and LHAGLUE,” hep-ph/0508110.
- [96] H. L. Lai, M. Guzzi, J. Huston, Z. Li, P. M. Nadolsky, J. Pumplin and C.-P. Yuan, “New parton distributions for collider physics,” Phys. Rev. D **82**, 074024 (2010).
- [97] R. D. Ball *et al.*, “Parton distributions with LHC data,” Nucl. Phys. B **867**, 244 (2013).
- [98] ATLAS and CMS Collaborations, “Combined Measurement of the Higgs Boson Mass in pp Collisions at $\sqrt{s} = 7$ and 8 TeV with the ATLAS and CMS Experiments,” Phys. Rev. Lett. **114**, 191803 (2015).
- [99] F. Maltoni, D. Pagani and I. Tsinikos, “Associated production of a top-quark pair with vector bosons at NLO in QCD: impact on $t\bar{t}H$ searches at the LHC,” JHEP **1602**, 113 (2016).
- [100] A. Bredenstein, A. Denner, S. Dittmaier and S. Pozzorini, “NLO QCD corrections to $pp \rightarrow t\bar{t}b\bar{b} + X$ at the LHC,” Phys. Rev. Lett. **103**, 012002 (2009); A. Bredenstein, A. Denner, S. Dittmaier and S. Pozzorini, “NLO QCD Corrections to Top Anti-Top Bottom Anti-Bottom Production at the LHC: 2. full hadronic results,” JHEP **1003**, 021 (2010); G. Bevilacqua, M. Czakon, C. G. Papadopoulos, R. Pittau and M. Worek, “Assault on the NLO Wishlist: $pp \rightarrow t\bar{t}b\bar{b}$,” JHEP **0909**, 109 (2009).
- [101] G. Bevilacqua, M. Czakon, C. G. Papadopoulos and M. Worek, “Dominant QCD Backgrounds in Higgs Boson Analyses at the LHC: A Study of $pp \rightarrow t\bar{t} + 2$ jets at Next-To-Leading Order,” Phys. Rev. Lett. **104**, 162002 (2010).
- [102] J. Alwall *et al.*, “The automated computation of tree-level and next-to-leading order differential cross sections, and their matching to parton shower simulations,” JHEP **1407**, 079 (2014).
- [103] NNPDF Collaboration, “Parton distributions with QED corrections,” Nucl. Phys. B **877**, 290 (2013).
- [104] J. Anderson, A. Avetisyan, R. Brock, S. Chekanov, T. Cohen, N. Dhingra, J. Dolen and J. Hirschauer *et al.*, “Snowmass Energy Frontier Simulations,” arXiv:1309.1057 [hep-ex]. Detector card adapted for DELPHES3.3.
- [105] M. Oreglia, “A Study of the Reactions $\psi' \rightarrow \gamma\gamma\psi$,” SLAC-236 (80,REC.APR. 81),

-
- J. Gaiser, “Charmonium Spectroscopy From Radiative Decays of the J/ψ and ψ' ,” SLAC-255 (82,REC.JUN.83) T. Skwarnicki, “A study of the radiative CASCADE transitions between the Upsilon-Prime and Upsilon resonances,” DESY-F31-86-02.
- [106] M. Bauer, T. Schell and T. Plehn, “Hunting the Flavon,” *Phys. Rev. D* **94**, no. 5, 056003 (2016).
- [107] C. D. Froggatt and H. B. Nielsen, “Hierarchy of Quark Masses, Cabibbo Angles and CP Violation,” *Nucl. Phys. B* **147**, 277 (1979).
- [108] M. Leurer, Y. Nir and N. Seiberg, “Mass matrix models,” *Nucl. Phys. B* **398**, 319 (1993); M. Leurer, Y. Nir and N. Seiberg, “Mass matrix models: The Sequel,” *Nucl. Phys. B* **420**, 468 (1994).
- [109] H. Georgi and S. L. Glashow, “Attempts to calculate the electron mass,” *Phys. Rev. D* **7**, 2457 (1973).
- [110] D. B. Kaplan, “Flavor at SSC energies: A New mechanism for dynamically generated fermion masses,” *Nucl. Phys. B* **365**, 259 (1991).
- [111] T. Gherghetta and A. Pomarol, “Bulk fields and supersymmetry in a slice of AdS,” *Nucl. Phys. B* **586**, 141 (2000); Y. Grossman and M. Neubert, “Neutrino masses and mixings in nonfactorizable geometry,” *Phys. Lett. B* **474**, 361 (2000); M. Blanke, A. J. Buras, B. Duling, S. Gori and A. Weiler, “ $\Delta F=2$ Observables and Fine-Tuning in a Warped Extra Dimension with Custodial Protection,” *JHEP* **0903**, 001 (2009); S. Casagrande, F. Goertz, U. Haisch, M. Neubert and T. Pfoh, “Flavor Physics in the Randall-Sundrum Model: I. Theoretical Setup and Electroweak Precision Tests,” *JHEP* **0810**, 094 (2008); M. Bauer, S. Casagrande, U. Haisch and M. Neubert, “Flavor Physics in the Randall-Sundrum Model: II. Tree-Level Weak-Interaction Processes,” *JHEP* **1009**, 017 (2010).
- [112] S. F. King and C. Luhn, “Neutrino Mass and Mixing with Discrete Symmetry,” *Rept. Prog. Phys.* **76**, 056201 (2013).
- [113] K. Tsumura and L. Velasco-Sevilla, “Phenomenology of flavon fields at the LHC,” *Phys. Rev. D* **81**, 036012 (2010).
- [114] M. Bauer, M. Carena and K. Gemmler, “Flavor from the Electroweak Scale,” *JHEP* **1511**, 016 (2015); M. Bauer, M. Carena and K. Gemmler, “Creating the Fermion Mass Hierarchies with Multiple Higgs Bosons,” arXiv:1512.03458 [hep-ph].
- [115] L. Calibbi, A. Crivellin and B. Zaldivar, “Flavor portal to dark matter,” *Phys. Rev. D* **92**, no. 1, 016004 (2015).
- [116] I. Dorsner and S. M. Barr, “Flavor exchange effects in models with Abelian flavor symmetry,” *Phys. Rev. D* **65**, 095004 (2002).
- [117] A. Ball *et.al.*, Future Circular Collider Study, Hadron Collider Parameters,” Tech. Rep. FCC-ACC-SPC-0001; N. Arkani-Hamed, T. Han, M. Mangano and L. T. Wang, “Physics oppor-

- tunities of a 100 TeV protonproton collider,” Phys. Rept. **652**, 1 (2016).
- [118] E. L. Berger, S. B. Giddings, H. Wang and H. Zhang, “Higgs-flavon mixing and LHC phenomenology in a simplified model of broken flavor symmetry,” Phys. Rev. D **90**, no. 7, 076004 (2014).
- [119] A. J. Buras, F. De Fazio, J. Girrbach, R. Kneijens and M. Nagai, “The Anatomy of Neutral Scalars with FCNCs in the Flavour Precision Era,” JHEP **1306**, 111 (2013).
- [120] A. Crivellin, A. Kokulu and C. Greub, “Flavor-phenomenology of two-Higgs-doublet models with generic Yukawa structure,” Phys. Rev. D **87**, no. 9, 094031 (2013).
- [121] UTfit Collaboration, “Model-independent constraints on $\Delta F = 2$ operators and the scale of new physics,” JHEP **0803**, 049 (2008), <http://www.utfit.org/UTfit/>.
- [122] M. Gorbahn, S. Jager, U. Nierste and S. Trine, “The supersymmetric Higgs sector and $B - \bar{B}$ mixing for large $\tan \beta$,” Phys. Rev. D **84**, 034030 (2011).
- [123] ETM Collaboration, “ $\Delta S = 2$ and $\Delta C = 2$ bag parameters in the standard model and beyond from $N_f = 2 + 1 + 1$ twisted-mass lattice QCD,” Phys. Rev. D **92**, no. 3, 034516 (2015); Fermilab Lattice and MILC Collaborations, “ $B_{(s)}^0$ -mixing matrix elements from lattice QCD for the Standard Model and beyond,” Phys. Rev. D **93**, no. 11, 113016 (2016).
- [124] J. Charles, S. Descotes-Genon, Z. Ligeti, S. Monteil, M. Papucci and K. Trabelsi, “Future sensitivity to new physics in B_d, B_s , and K mixings,” Phys. Rev. D **89**, no. 3, 033016 (2014).
- [125] UTfit Collaboration, “The UTfit collaboration average of D meson mixing data: Winter 2014,” JHEP **1403**, 123 (2014).
- [126] A. J. Buras, J. Girrbach, D. Guadagnoli and G. Isidori, “On the Standard Model prediction for $\text{BR}(B_{s,d} \rightarrow \mu^+ \mu^-)$,” Eur. Phys. J. C **72**, 2172 (2012).
- [127] R. Fleischer, “Theory News on $B_{s(d)} \rightarrow \mu^+ \mu^-$ Decays,” arXiv:1212.4967 [hep-ph].
- [128] CMS and LHCb Collaborations, “Observation of the rare $B_s^0 \rightarrow \mu^+ \mu^-$ decay from the combined analysis of CMS and LHCb data,” Nature **522**, 68 (2015).
- [129] CMS Collaboration, “Measurement of the $B(s) \rightarrow \mu^+ \mu^-$ branching fraction and search for B_0 to $\mu^+ \mu^-$ with the CMS Experiment,” Phys. Rev. Lett. **111**, 101804 (2013).
- [130] LHCb Collaboration, “Measurement of the $B_s^0 \rightarrow \mu^+ \mu^-$ branching fraction and search for $B^0 \rightarrow \mu^+ \mu^-$ decays at the LHCb experiment,” Phys. Rev. Lett. **111**, 101805 (2013).
- [131] MEG Collaboration, “New constraint on the existence of the $\mu^+ \rightarrow e^+ \gamma$ decay,” Phys. Rev. Lett. **110**, 201801 (2013).
- [132] Belle Collaboration, “New search for $\tau \rightarrow \mu \gamma$ and $\tau \rightarrow e \gamma$ decays at Belle,” Phys. Lett. B **666**, 16 (2008).
- [133] A. M. Baldini *et al.*, “MEG Upgrade Proposal,” arXiv:1301.7225 [physics.ins-det].
- [134] R. Harnik, J. Kopp and J. Zupan, “Flavor Violating Higgs Decays,” JHEP **1303**, 026 (2013).
- [135] M. A. Shifman, A. I. Vainshtein and V. I. Zakharov, “Remarks on Higgs Boson Interactions

-
- with Nucleons,” Phys. Lett. B **78**, 443 (1978); for a pedagogical discussion of the infamous factor $2/27$ see also http://www.thphys.uni-heidelberg.de/~plehn/pics/dark_matter.pdf.
- [136] A. Crivellin, M. Hoferichter and M. Procura, “Accurate evaluation of hadronic uncertainties in spin-independent WIMP-nucleon scattering: Disentangling two- and three-flavor effects,” Phys. Rev. D **89**, 054021 (2014).
- [137] A. Crivellin, M. Hoferichter and M. Procura, “Improved predictions for $\mu \rightarrow e$ conversion in nuclei and Higgs-induced lepton flavor violation,” Phys. Rev. D **89**, 093024 (2014).
- [138] P. Junnarkar and A. Walker-Loud, “Scalar strange content of the nucleon from lattice QCD,” Phys. Rev. D **87**, 114510 (2013).
- [139] R. Kitano, M. Koike and Y. Okada, “Detailed calculation of lepton flavor violating muon electron conversion rate for various nuclei,” Phys. Rev. D **66**, 096002 (2002) [Phys. Rev. D **76**, 059902 (2007)]; T. Suzuki, D. F. Measday and J. P. Roalsvig, “Total Nuclear Capture Rates for Negative Muons,” Phys. Rev. C **35**, 2212 (1987).
- [140] SINDRUM II Collaboration, “A Search for muon to electron conversion in muonic gold,” Eur. Phys. J. C **47**, 337 (2006).
- [141] DeeMe Collaboration, “DeeMe experiment - An experimental search for a mu-e conversion reaction at J-PARC MLF,” Nucl. Phys. Proc. Suppl. **248-250**, 52 (2014).
- [142] COMET Collaboration, “A search for muon-to-electron conversion at J-PARC: The COMET experiment,” PTEP **2013**, 022C01 (2013).
- [143] Mu2e Collaboration, “Mu2e Conceptual Design Report,” arXiv:1211.7019 [physics.ins-det].
- [144] K. Hayasaka *et al.*, “Search for Lepton Flavor Violating Tau Decays into Three Leptons with 719 Million Produced Tau+Tau- Pairs,” Phys. Lett. B **687**, 139 (2010).
- [145] SINDRUM Collaboration, “Search for the Decay $\mu^+ \rightarrow e^+e^+e^-$,” Nucl. Phys. B **299**, 1 (1988).
- [146] Mu3e Collaboration, “The Mu3e Experiment - Introduction and Current Status,” PoS NUFACT **2014**, 088 (2015).
- [147] [CDF Collaboration], “Direct Measurement of the Total Decay Width of the Top Quark,” Phys. Rev. Lett. **111**, no. 20, 202001 (2013).
- [148] A. D. Martin, W. J. Stirling, R. S. Thorne and G. Watt, “Parton distributions for the LHC,” Eur. Phys. J. C **63**, 189 (2009).
- [149] B. Schmidt and M. Steinhauser, “CRunDec: a C++ package for running and decoupling of the strong coupling and quark masses,” Comput. Phys. Commun. **183**, 1845 (2012).
- [150] J. M. Campbell *et al.*, “Working Group Report: Quantum Chromodynamics,” arXiv:1310.5189 [hep-ph].
- [151] F. Caola, talk at “QCD, EW and Tools at 100 TeV”, CERN, Oct. 7th 2015,

- <https://indico.cern.ch/event/437912/session/2/contribution/11/attachments/1166613/1682282/singletop100TeV.pdf>.
- [152] ATLAS Collaboration, “Search for high-mass diphoton resonances in pp collisions at $\sqrt{s} = 8$ TeV with the ATLAS detector,” *Phys. Rev. D* **92**, no. 3, 032004 (2015).
- [153] ATLAS Collaboration, “Search for high-mass dilepton resonances in pp collisions at $\sqrt{s} = 8$ TeV with the ATLAS detector,” *Phys. Rev. D* **90**, no. 5, 052005 (2014).
- [154] ATLAS Collaboration, “A search for high-mass resonances decaying to $\tau^+\tau^-$ in pp collisions at $\sqrt{s} = 8$ TeV with the ATLAS detector,” *JHEP* **1507**, 157 (2015).
- [155] ATLAS Collaboration, “Search for new phenomena in the dijet mass distribution using $p-p$ collision data at $\sqrt{s} = 8$ TeV with the ATLAS detector,” *Phys. Rev. D* **91**, no. 5, 052007 (2015).
- [156] CMS Collaboration, “Search for resonances and quantum black holes using dijet mass spectra in proton-proton collisions at $\sqrt{s} = 8$ TeV,” *Phys. Rev. D* **91**, no. 5, 052009 (2015).
- [157] CMS Collaboration, “Search for diphoton resonances in the mass range from 150 to 850 GeV in pp collisions at $\sqrt{s} = 8$ TeV,” *Phys. Lett. B* **750**, 494 (2015).
- [158] CMS Collaboration, “Search for physics beyond the standard model in dilepton mass spectra in proton-proton collisions at $\sqrt{s} = 8$ TeV,” *JHEP* **1504**, 025 (2015).
- [159] CMS Collaboration, “Search for additional neutral Higgs bosons decaying to a pair of tau leptons in pp collisions at $\sqrt{s} = 7$ and 8 TeV,” CMS-PAS-HIG-14-029.
- [160] ATLAS Collaboration, “Identification of the Hadronic Decays of Tau Leptons in 2012 Data with the ATLAS Detector,” ATLAS-CONF-2013-064.
- [161] A. Alloul, N. D. Christensen, C. Degrande, C. Duhr and B. Fuks, “FeynRules 2.0 - A complete toolbox for tree-level phenomenology,” *Comput. Phys. Commun.* **185**, 2250 (2014); N. D. Christensen and C. Duhr, “FeynRules - Feynman rules made easy,” *Comput. Phys. Commun.* **180**, 1614 (2009).
- [162] C. G. Lester and D. J. Summers, “Measuring masses of semiinvisibly decaying particles pair produced at hadron colliders,” *Phys. Lett. B* **463**, 99 (1999); A. Barr, C. Lester and P. Stephens, “m(T2): The Truth behind the glamour,” *J. Phys. G* **29**, 2343 (2003).
- [163] A. Alves, O. Eboli and T. Plehn, “It’s a gluino,” *Phys. Rev. D* **74**, 095010 (2006).
- [164] ATLAS Collaboration, ATLAS-PHYS-PUB-2015-040.
- [165] M. Spira, A. Djouadi, D. Graudenz and P. M. Zerwas, “Higgs boson production at the LHC,” *Nucl. Phys. B* **453**, 17 (1995) [hep-ph/9504378].
- [166] A. Djouadi, M. Spira and P. M. Zerwas, “Two photon decay widths of Higgs particles,” *Phys. Lett. B* **311**, 255 (1993) [hep-ph/9305335].
- [167] Z. z. Xing, H. Zhang and S. Zhou, “Updated Values of Running Quark and Lepton Masses,” *Phys. Rev. D* **77**, 113016 (2008).

-
- [168] M. C. Gonzalez-Garcia, M. Maltoni, J. Salvado and T. Schwetz, “Global fit to three neutrino mixing: critical look at present precision,” *JHEP* **1212**, 123 (2012).